Intermediate-Energy Coulomb Excitation of the Neutron-Rich Radioactive Isotopes ^{26,28}Ne, $^{28-31}$Na, $^{30-34}$Mg, ^{34,35}Al, ^{33}Si and ^{34}P

By

Boris V. Pritychenko

A DISSERTATION

Submitted to
Michigan State University
in partial fulfillment of the requirements
for the Degree of

DOCTOR OF PHILOSOPHY

Department of Physics and Astronomy

2000

ABSTRACT

Intermediate-Energy Coulomb Excitation of the Neutron-Rich Radioactive Isotopes ^{26,28}Ne, $^{28-31}$Na, $^{30-34}$Mg, ^{34,35}Al, ^{33}Si and ^{34}P

By

Boris V. Pritychenko

The subject of this thesis is the study of collectivity and deformation in light neutron-rich radioactive nuclei in the $Z \sim 12$ and $N \sim 20$ region. Recent experimental and theoretical results indicate the existence of strongly deformed nuclei near the $N = 20$ shell closure. In a Coulomb excitation experiment conducted at RIKEN, large values for the reduced transition probability ($B(E2\uparrow)$) and deformation parameter β_2 in ^{32}Mg were reported. These results are in good agreement with shell-model predictions, which take into account an inversion of the normal $\nu(f_{7/2})\nu(d_{3/2})$ shell ordering.

To achieve a more complete understanding of the nuclear properties of light nuclei, intermediate-energy Coulomb excitation experiments were conducted at the National Superconducting Cyclotron Laboratory at Michigan State University. Radioactive nuclear beams of ^{26,28}Ne, $^{28-31}$Na, $^{30-34}$Mg, ^{34,35}Al, ^{33}Si and ^{34}P produced by projectile fragmentation with energies of $E \approx 50$ MeV/nucleon were directed onto a secondary ^{197}Au target, where Coulomb excitation of the projectile and target took place. The de-excitation photons were detected in an array of position-sensitive NaI(Tl) detectors, which were selected for in-beam γ-ray spectroscopy.

The energies and $B(E2; 0^+_{\text{g.s.}} \rightarrow 2^+_1)$ values for the lowest $J^\pi = 2^+$ states in the neutron-rich radioactive nuclei ^{26,28}Ne and ^{30,32}Mg were measured. In addition, a 1.436 MeV state was observed in ^{32}Mg. An upper limit on $B(E2\uparrow)$ was established in ^{34}Mg. The energies of the first excited states, and excitation cross sections were

also measured for: ^{28,30,31}Na, ^{31,33}Mg, ^{34,35}Al, ^{33}Si and ^{34}P. Data on ^{31}Na and ^{33}Mg indicate that excited states are highly collective as predicted by the island of inversion hypothesis. These results imply large collectivities in the $Z \geq 11$ and $N \geq 20$ region.

Due to the mixing ratio-, spin- and parity assignment uncertainties in the odd nuclei, only the maximum possible values for $B(E1\uparrow)$, $B(E2\uparrow)$, $B(M1\uparrow)$ and $B(M2\uparrow)$ were extracted. Comparison of these values with recommended upper limits for γ-strengths in light nuclei allowed us to exclude $M2$ and often $M1$ excitations as possible explanations. The extracted upper limits on transition intrinsic electric quadrupole moments in ^{28,29,30,31}Na were compared to reported ground state moment measurements.

To those

who believe

ACKNOWLEDGMENTS

The research described herein was performed at the National Superconducting Cyclotron Laboratory (NSCL) and it involved the collaborative efforts of many at the NSCL. It is a difficult task to express my gratitude to all those esteemed people, and I apologize to those I may neglected to mention.

I must first thank my advisor, Professor Thomas Glasmacher. I would like to thank him for his guidance in the many stages my research, for teaching me a good deal accelerator nuclear physics; for his enthusiasm and most of all, for his patience.

I also would like to express my gratitude to Heiko Scheit and Richard Ibbotson for teaching me about nuclear data analysis. I would also like to thank them for their assistance and encouragement during my research. I was very fortunate to find such an enlightened comrade as Heiko. I believe he made me a better person.

I am indebted to Prof. Vladimir G. Zelevinsky for actively serving on my guidance committee. He and Alexander Sakharuk provided me with theoretical calculations for my thesis project and a good deal valuable information about nuclear theory. I must thank him for his constant help and support during my stay at the NSCL.

I was very fortunate to have an excellent collaboration with Florida State University; Professors Kirby Kemper and Paul Cottle taught me a great deal about physics.

I will remember John Yurkon for assisting me with many difficult aspects of experimental nuclear physics, and also helping me with my work at the NSCL.

In addition, I will also remember Takashi Nakamura for his valuable insights into Coulomb excitation and for exposing me to Japanese culture.

I am also thankful to the cyclotron operations group for running the accelerator during my thesis experiments, and to the computer department for their help and patience during my data analysis.

Special thanks go to Barry Davids and Joann Prisciandaro for proof reading my thesis. I was also lucky to have Luke Chen and Richard Shomin as office mates. They provided help and a good environment for productive research.

I would also like to acknowledge the generous moral support of Lulu Rinkleib throughout this project.

Finally, I would like to express my gratitude to Professors James Linnemann, S. D. Mahanti and Michael Thoennessen for their help, expertise and for serving on my guidance committee. The financial support of the NSF is also gratefully acknowledged.

Extended Curriculum Vitae

I was born and raised in the Former Soviet Union. In 1979 I attended Tomsk State University and after one year in Western Siberia transfered to the Department of Physics and Technology at the Khar'kov State University. I was granted a Diploma in 1985 for experimental nuclear physics and received the rank of lieutenant in the reserve of the Red Armed Forces. From the summer of 1984 until December 1991 I worked at the Baksan Neutrino Observatory, Institute for Nuclear Research, Academy of Sciences of the USSR (Northern Caucasus, Russia).

Looking back, I must admit that I was very lucky to be there and work for Prof. Alexander A. Pomansky [1], despite the low pay and poor living conditions. To say that Pomansky became a professor under the leadership of Bruno M. Pontecorvo and convinced the leadership of the Tyrnyauz district not to support communist hard-liners on August 20, 1991, this would not be sufficient to describe him. He was the son of a known Russian painter and was well versed in art and history. Life in the Caucasus mountains was rough, we basically had two choices: to succeed in physics or to find another place of employment. The first option was the more interesting, and from 1988 until I moved to Berkeley in 1991, I worked on the dark matter problem. Somehow Pomansky was able to predict that I would not return to Russia but never tried to stop me. I learned a great deal from him, unfortunately, he died in April, 1993 from the heart failure. My first Ph.D. project was never completed.

A few weeks later, I spoke with V.M. Novikov and V.P. Spiridonov. They suggested that I become a graduate student in the States and forget about my "ego". I would like to thank "BOBA" and Slava for their help during this difficult moment in my life. I still remember that day in June of 1993. I was standing on the corner of Telegraph Avenue and Derby in Berkeley, when I made my final decision to stay in

this country. I would like to express my gratitude to the Center for Particle Astrophysics and to Prof. Bernard Sadoulet, for allowing me to stay despite the obvious problems with my former employers. I also would like to express my gratitude to Prof. F. T. Avignone (University of South Carolina) and R. E. Lanou (Brown University) for their help and support. During my stay in Berkeley I was able to get a different look at myself and learned a lot. Without doubt, it was the most remarkable period in my life and I have never been the same.

In September of 1994 I became a graduate student at Michigan State with the serious intention of obtaining a Ph.D., in spite of unfavorable circumstances. I soon came to realize the difference between my expectations and reality in East Lansing, which resulted in two unhappy years satisfying the Michigan State University degree requirements. In the Fall of 1996 I passed my comprehensive exams and started to work for Prof. T. Glasmacher at the National Superconducting Cyclotron Laboratory. I really appreciate the fact that Thomas invited me to work with the Gamma group, it was during this time I was able to recover from some of my problems and confide in such friends as Heiko Scheit.

I would also like to express my gratitude to this wonderful country, which accepted me with all my strengths and weaknesses. I have finally come to terms with myself, and can freely admit that I do not feel the need to prove myself anymore. I'm tired of many remarkable things which happened to me and would like to have just a normal life.

CONTENTS

LIST OF TABLES

LIST OF FIGURES

Chapter 1

Introduction

1.1 Physics of Atomic Nuclei

The experimental study of atomic nuclei is currently motivated by:

- The unique nature of nuclei as the main constituents of matter.
- The necessity of establishing the limits of nuclear stability, radioactivity and searching for the neutron and proton driplines [2].
- The search for nuclei with unique physical properties (large spatial neutron or proton halos [3, 4] and large deformations in neutron-rich isotopes [5]).
- The extension of experimental knowledge of fundamental nuclear processes [6].
- Astrophysical applications (solar neutrino problem, origin of the elements [6, 7]).
- Industrial and medical applications of nuclear physics [8].

The interplay of nuclear stability and radioactivity shaped the world as we know it. The study of these phenomena allows us to gain a better understanding of our universe useful in many different applications: astrophysics, radioactive dating, geology, industry, power production and nuclear medicine.

The study of the fundamental properties of nuclei such as neutron or proton halos and deformations in neutron-rich isotopes is part of the search for an understanding

of the fundamental properties of nuclear matter. Currently, the center of interest in nuclear structure has shifted to nuclei far from the line of stability. In halo nuclei, most of the nucleons occupy standard single-particle states, forming what is usually called the "core" of the nucleus. This core is relatively inert in nuclear reactions at low energies. Only a few neutrons (one or two) occupy outer orbitals and create a "halo" stretched in space far away from the core. The most studied halo nuclei are ^{11}Be and ^{11}Li [4]. The halo phenomenon has also been identified in ^{14}Be, ^{17}B and ^{19}C [9].

First evidence for the existence of an "island of deformed nuclei" near the $N = 20$ shell closure was obtained in 1975 by Thibault *et al.* [10] from mass measurements of sodium isotopes. They found that ^{31}Na and ^{32}Na are more tightly bound than expected from the spherically symmetrical $\pi(sd)$-shell model. (Figure 1.1 shows the region of light neutron-rich nuclei with $N \sim 20$.) In the same year this phenomenon was explained by Campi *et al.* [11] via the introduction of neutron $f_{7/2}$ intruder orbits for $Z < 14$ nuclei (i.e., an "inversion" of the standard shell ordering) in the framework of Hartree-Fock calculations. Theoretical research in this field [5, 12] created a basis for understanding the unusual properties of ^{32}Mg, which was studied at CERN [13, 14, 15] and RIKEN [16]. Using the technique of intermediate-energy Coulomb excitation, Motobayashi *et al.* [16] reported the reduced transition probability of the first excited 2^+ state in ^{32}Mg, $B(E2; 0^+_{g.s.} \rightarrow 2^+_1) = 454(78)$ e^{2}fm^4, with a corresponding deformation parameter of $\beta_2 \approx 0.52$. A similar result was recently obtained at the National Superconducting Cyclotron Laboratory (NSCL) [17]. Recent calculations by Caurier *et al.* [18] predict that intruder configurations dominate the ground states of ^{30}Ne, ^{31}Na, and ^{32}Mg, and that they are nearly degenerate with the closed shell states in ^{31}Ne, ^{32}Na and ^{33}Mg. However, the exact boundaries of the island of inversion are still not known experimentally [5, 19]. The technique of intermediate-

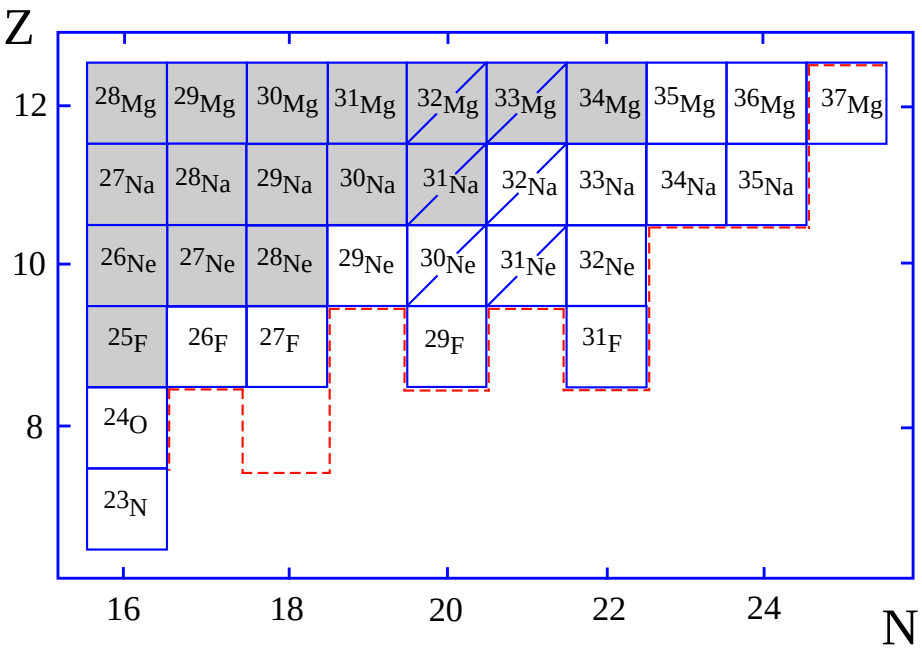

Figure 1.1: Neutron dripline and the island of inversion. Isotopes produced at the NSCL for this thesis with an experimental yield more than 1 particle/sec are shown in gray, the slashed boxes represent the island of inversion and the dashed line represents the calculated neutron dripline [2].

energy Coulomb excitation is well-suited for this kind of research because it allows the deduction of reduced transition probabilities (collectivity) from experimental excitation cross sections in a model-independent way [20, 21]. A detailed discussion of intermediate-energy Coulomb excitation is presented in chapter 2.

The unusual properties observed in the island of inversion region motivate the study of these nuclei. For this thesis, experiments were conducted at the NSCL, in which the isotopes ^{26,28}Ne, $^{28-31}$Na, $^{30-34}$Mg, ^{34,35}Al, ^{33}Si and ^{34}P were studied via intermediate-energy Coulomb excitation. Interpretation of the experimental data was done on the basis of theoretical nuclear models, which are described in general terms in sections 1.2 and 1.3.

1.2 Single-Particle Approach

In the single-particle approach we often employ the widely used shell model [5, 18, 22] or Hartree-Fock calculations [23, 24, 25, 26, 27]. In its current form [5] the shell model represents a very powerful tool for predicting the structure of nuclei. In the independent-particle approximation model the effect of all nucleons in the nucleus is replaced by an average or mean field. The nuclear Hamiltonian is then a sum of single-particle terms

$$H^0 = \sum_{i=1}^{n} \epsilon(i) n_i \,, \tag{1.1}$$

where the summation is over all single-particle states. The energy of each single-particle state is represented by $\epsilon(i)$ and n_i is the number operator which measures the occupancy (0 or 1) of the single-particle state i. In this model, the nuclear single-particle spectrum is not smooth; it has relatively large energy gaps between groups of single-particle states. When each group of states is completely filled, the Fermi energy of the nucleus is just below one of these large energy gaps. Thus more energy than usual is required to excite the nucleus. Nuclei fulfilling this condition for either protons and neutrons are called closed shell (magic) nuclei. With all the orbits filled, the ground state of the nucleus is tightly bound and spherical in shape. By adding the residual interaction V to the independent-particle model (1.1) and truncating the space of orbitals i, one performs a diagonalization of the total Hamiltonian $H^0 + V$ and obtains many-body states and their energies. This allows one to describe nuclear deformation. In the framework of the shell model large deformation typically requires a large number of basis states.

The Hartree-Fock method is used for determining the average one-body potential and single-particle energies $\epsilon(i)$ from the nucleon-nucleon interaction [26, 27]. This method allows a self-consistent study of nuclear structure starting from a given Skyrme type nucleon-nucleon force V_{ij} and determines the average nucleonic proper-

ties (binding energies, nuclear radii, density distributions, ...) and the excited states in each nucleus. Because of the need to describe average nuclear properties, the nucleon-nucleon force is parameterized with a relatively small number of parameters, to be determined throughout the nuclear mass region.

For many nuclei, a deformed intrinsic shape is more stable. Then it is possible to use deformed average potentials. The desire to obtain a simple picture leads us to the Nilsson model [28, 29, 30, 31]. In the case of axial symmetry the Nilsson single-particle Hamiltonian is given by

$$H = H_0 + H_\delta + a\mathbf{l}\cdot\mathbf{s} + b\mathbf{l^2}\,, \tag{1.2}$$

where H_0 is the spherical part, generally taken to be the Hamiltonian of an isotropic three-dimensional harmonic oscillator. $\mathbf{l}$ and $\mathbf{s}$ are the orbital angular moment and the nucleon spin, respectively. The deformation is produced by H_δ due to a quadrupole field,

$$H_\delta(\mathbf{r_i}) = -\delta_{osc}\frac{1}{3}\mu\omega_0^2 r_i^2\sqrt{\frac{16\pi}{5}}Y_{20}(\theta_i)\,. \tag{1.3}$$

Here δ_{osc} provides a measure of the departure from a spherical shape and $\mathbf{r_i}$ is the coordinate of nucleon i. a and b are phenomenological parameters for each shell, and for large deformations, effects due to $\mathbf{l}\cdot\mathbf{s}$ and $\mathbf{l^2}$ are less important. Nilsson orbitals for light deformed nuclei recently calculated by A. Sakharuk [17] are presented in Figure 1.2. It is easy to see that for N = 20 and $\delta \geq 0.4$, the $f_{7/2}$ nuclear orbitals penetrate into the *sd*-shell (intruder states). Therefore $N = 20$ ceases to be a magic number. This phenomenon explains the existence of the island of inversion.

Experimental observables for the disappearance of the shell gap include:

- Low energy of the first excited state.
- Large degree of collectivity (deformation).
- Relatively large neutron- or proton capture cross sections.

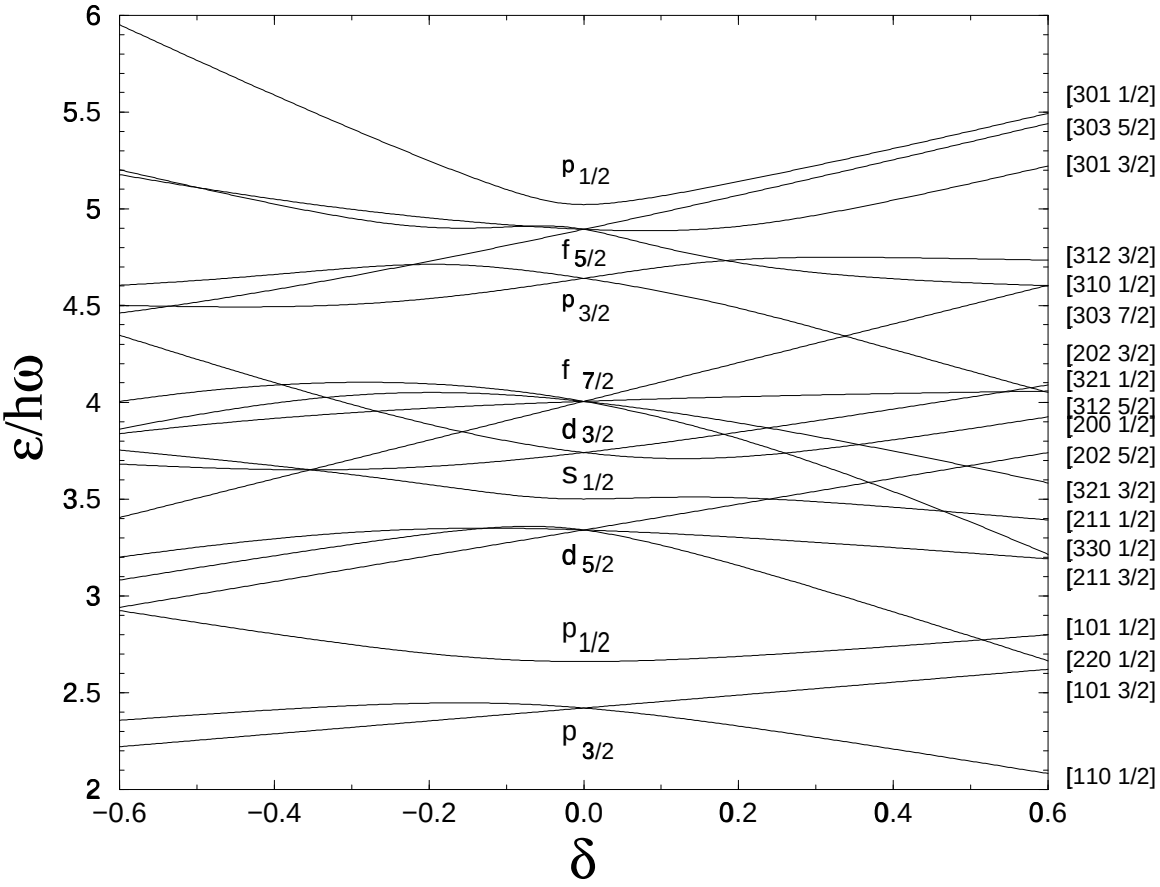

Figure 1.2: Nilsson diagrams for light nuclei. Each nuclear state is described by the following parameters: total number of quanta, number of quanta along the z-axis, projection of orbital momentum on the z-axis and projection of the total momentum on the z-axis. This particular diagram is explained in section 4.3.2.

For an independent-particle approximation in the deformed basis, the residual interaction is ignored and the nuclear Hamiltonian is a sum of the single-particle Hamiltonians over all active nucleons. In this model, all states are separated into three groups: the core states, the valence states and the empty states. Since the single-particle Hamiltonian $H(\mathbf{r_i})$ is, in part, a result of the interaction of the valence nucleons with the core, the actual value of the deformation depends on the equilibrium shape of the core. The Nilsson model provides a reasonable description of a wide variety of nuclei. It was successfully applied to calculating intrinsic quadrupole moments in ^{26,28}Ne and ^{30,32,34}Mg [17]. The comparison of the calculated and experimentally measured moments (see equations 4.1 and 4.2) allows us to deduce that these nuclei likely have a prolate shape.

1.3 Collective Approach

Many observed properties of nuclei can be described in a picture that includes the motion of many nucleons "collectively". It is convenient to describe nuclear properties with a Hamiltonian expressed in terms of macroscopic coordinates of the system.

Rotational Model. From the previous discussion it follows that nuclei away from the filled shells tend to be deformed. In general, the nuclear shape tends to be prolate, i.e., elongated along the z-axis, at the beginning of a major shell, and oblate, i.e., flattened at the poles, toward the end of a major shell. The deformation has the same sign as the quadrupole moment. The appearance of rotational spectra indicates onset of deformation. In quantum mechanics, rotation can be observed only for asymmetric (non-spherical) objects. For an axially symmetric object with angular momentum

$$\mathbf{J} = I\boldsymbol{\omega}\,, \tag{1.4}$$

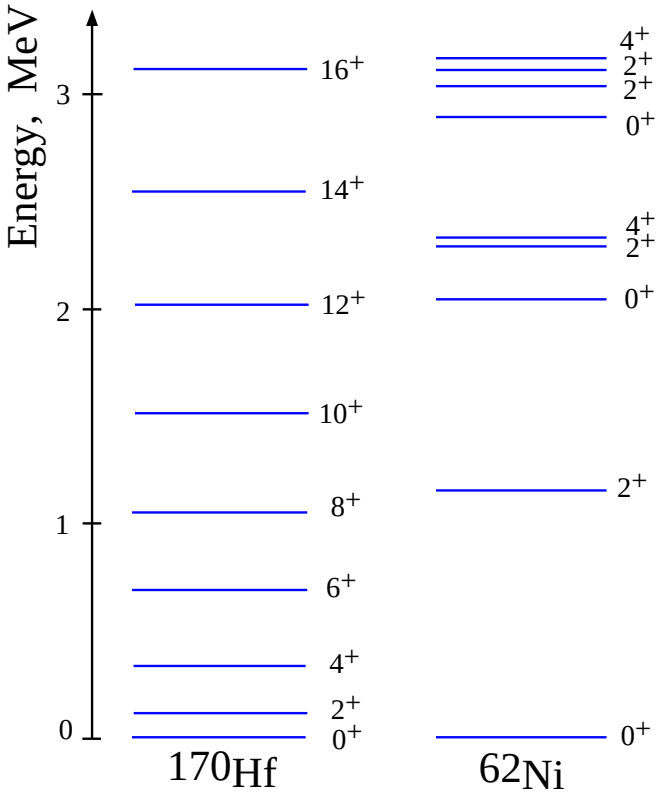

Figure 1.3: Energy spectra for the rotational nucleus ^{170}Hf and the vibrational nucleus ^{62}Ni. Data is taken from [33].

the rotational Hamiltonian is

$$H_{rot} = \frac{\hbar^2}{2I}\mathbf{J}^2\,, \tag{1.5}$$

where I is the moment of inertia for rotation around the axis perpendicular to the symmetry axis and ω is the angular velocity. For a given intrinsic state, the nucleus can rotate with different angular velocities. A group of states, each with different total angular momentum J but sharing the same intrinsic state, forms a rotational band. The ground state band for ^{170}Hf is presented in Figure 1.3. The energy of a rotational band is

$$E_J = \frac{\hbar^2}{2I}J(J+1) + E_K\,, \tag{1.6}$$

where E_K represents contributions from the intrinsic part of the wave function. In the rotational model we also can calculate static moments and transition rates. For

example, the observed quadrupole moment is

$$Q_{JK} = \frac{3K^2 - J(J+1)}{(J+1)(2J+3)} Q_0 \,, \tag{1.7}$$

where K is an eigenvalue of $\mathbf{J}_3$ ($J = K$ for the ground state) and Q_0 is the intrinsic quadrupole moment, which is a function of deformation. The reduced transition probability in the limit of the rigid rotator is taken from [30] as

$$B(E2; J_i \to J_f) = \frac{5}{16\pi} e^2 Q_0^2 \langle J_i K 20 | J_f K \rangle^2 \,, \tag{1.8}$$

where the Clebsch-Gordan coefficient $\langle J_i K 20 | J_f K \rangle$ represents the conservation of the quantum number K in the transition between the rotational states of the same intrinsic structure.

Vibrational Model. A large number of nuclear properties can be explained from the liquid-drop model as the interplay between surface tension, Coulomb repulsion and volume energy of the drop. Coulomb or nuclear excitation can excite nuclei and set them into vibration around the equilibrium. For example, the nucleus can change its size without changing its shape. Such motion involves the oscillation of density and is called a breathing mode [31]. To preserve the nuclear shape, the breathing mode generates 0^+ states. Low-lying 0^+ states in ^{16}O, ^{40}Ca and ^{90}Zr indicate the presence of a breathing mode. A second type of vibration is an oscillation in the shape of the nucleus without changing the density; such collective behavior can be also explained in the liquid-drop model [30, 31]. The shape of the liquid drop can be described in terms of a set of shape parameters $\alpha_{\lambda\mu}$:

$$R(\theta, \phi) = R_0 \{ 1 + \sum_{\lambda\mu} \alpha_{\lambda\mu}(t) Y_{\lambda\mu}(\theta, \phi) \} \,, \tag{1.9}$$

where $R(\theta, \phi)$ is the distance from the center of the nucleus to the surface at angles (θ, ϕ) and R_0 is the radius of the equivalent density sphere. In even-even nuclei,

spin and parity assignments for the ground and first excited states are usually 0^+ and 2^+. Figure 1.3 shows a triplet of levels with J^π equal to 0^+, 2^+ and 4^+ with energy roughly twice the excitation energy which is a good indication of quadrupole vibrations. The Hamiltonian for vibrational excitation around spherical equilibrium shape can be written as [30, 31]

$$H_\lambda = \frac{1}{2} C_\lambda \sum_\mu |\alpha_{\lambda\mu}|^2 + \frac{1}{2} D_\lambda \sum_\mu |\frac{d\alpha_{\lambda\mu}}{dt}|^2 , \tag{1.10}$$

where the quantity C_λ is related to the surface and Coulomb energies of the nuclear fluid and D_λ is a quantity having the equivalent role as the mass in nonrelativistic kinetic energy in mechanics. However, the vibrations can be also described microscopically, and the resulting Hamiltonian still has, in the harmonic approximation, the form (1.10). If different modes of excitation are decoupled from each other, then for small oscillations the amplitude $\alpha_{\lambda\mu}$ undergoes harmonic oscillation with frequency

$$\omega_\lambda = \left(\frac{C_\lambda}{D_\lambda} \right)^{\frac{1}{2}} , \tag{1.11}$$

where $\hbar\omega_\lambda$ is a quantum of vibrational energy for multipole λ. A shape vibration of order λ, with density vibrations, is characterized by large values of the multipole moment (related to the total particle density $\rho(\mathbf{r})$)

$$\mathcal{M}(\lambda\mu) = \int \rho(\mathbf{r}) r^\lambda Y_{\lambda\mu}(\vartheta, \varphi) d\tau \, . \tag{1.12}$$

The electric multipole moment for a spherical charge distribution is exactly the same as for a surface deformation in a system with constant density and a sharply defined radius R (liquid-drop model)

$$\mathcal{M}(E\lambda, \mu) = \frac{3}{4\pi} Z e R^\lambda \alpha_{\lambda\mu} \, . \tag{1.13}$$

Finally, the transition probability for exciting a vibrational quantum is very similar to the rotational model (see equation 1.8) except for the geometrical (Clebsch-Gordan)

coefficient [32]

$$B(E\lambda; n_\lambda = 0 \rightarrow n_\lambda = 1) = \left(\frac{3}{4\pi} Z e R^\lambda\right)^2 {\beta_2}^2 \,. \tag{1.14}$$

For even-even nuclei both models produce an identical result for the deformation parameter

$$|\beta_2| = \frac{4\pi}{3} \frac{\sqrt{B(E2)}}{ZeR^2} \,. \tag{1.15}$$

The collective models were introduced to describe coherent motion of many nucleons and these models successfully predict properties of heavy nuclei. Unfortunately, the experimental measurement of the transition probability between the ground and first excited states by itself does not discriminate static and dynamic (vibrational) deformations.

Chapter 2

Intermediate-Energy Coulomb Excitation

This chapter contains a general description of the semi-classical theory of intermediate-energy Coulomb excitation. Possible physical implications of the theory are discussed and limitations are given.

2.1 General Description

Coulomb excitation is a very powerful tool for the study of low-lying nuclear states [34, 35, 36]. The excitation of target or projectile nuclei occurs by means of the electromagnetic interaction with another nucleus. Since the interaction strength is proportional to the charge Z of the projectile nucleus, Coulomb excitation is especially useful in the collision of heavy ions, with cross sections proportional to Z^2. Coulomb excitation dominates nuclear excitation in scattering when the bombarding energy is below the Coulomb barrier or when the distance of the closest approach between nuclei is larger than the sum of the projectile and target nuclear radii ("touching sphere" distance) [37]. This can be experimentally achieved by selecting only events

with small scattering angles. The Coulomb excitation cross sections provide a model-independent way to measure collectivity and deformation parameters for even-even and odd nuclei [35, 38] with in-beam γ-spectroscopy [21, 39], when the isotope of interest is short-lived and a stable target cannot be produced.

2.2 Excitation Cross Section

The two-body scattering problem can be reduced [40] to the central-body problem (motion of a single body in an external field when its potential energy depends only on its distance r from some fixed point). Consequently the path of a particle lies in one plane and the classical Lagrangian can be written in polar coordinates r, ϕ as follows

$$L = \frac{1}{2}m(\dot{r}^2 + r^2\dot{\phi}^2) - U(r)\,, \tag{2.1}$$

where $\dot{r}$ and $\dot{\phi}$ are the radial and angular velocity of the particle, respectively. In a central field the path of a particle is symmetrical about a line from the center to the nearest point in the orbit (OA in Figure 2.1). Here the deflection angle χ is equal to $|\pi - 2\phi_0|$ and ϕ_0 is given by

$$\phi_0 = \int_{r_{min}}^{\infty} \frac{(M/r^2)dr}{\sqrt{2m(E - U(r)) - M^2/r^2}}\,, \tag{2.2}$$

where is $M = mr^2\dot{\phi}$. For infinite motion it is common to use the initial relative velocity v_∞ of the particle and the impact parameter b instead of the constants energy (E) and angular momentum (M). The impact parameter is the length of the perpendicular from the center O to the direction of v_∞, i.e. the distance at which the particle would pass the center if there were no field or force, and $E = \frac{1}{2}m{v_\infty}^2$ and $M = mbv_\infty$. After

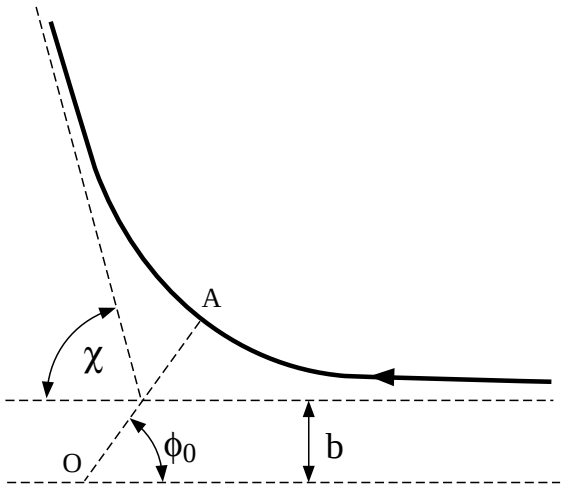

Figure 2.1: Classical picture of the Coulomb-projectile trajectory. The projectile nucleus is deflected by means of electromagnetic interaction with the target nucleus, which is located at the center O.

substitution the equation for ϕ_0 becomes

$$\phi_0 = \int_{r_{min}}^{\infty} \frac{(b/r^2)dr}{\sqrt{[1-(b^2/r^2)-(2U/mv_\infty^2)]}}\,. \tag{2.3}$$

The last integral describes the scattering angle χ as a function of b. Assuming that the scattering angle is a monotonically decreasing function of the impact parameter we can deduce that only those particles whose impact parameters lie between $b(\chi)$ and $b(\chi)+db(\chi)$ are scattered at angles between χ and $\chi+ d\chi$. The effective cross section is $d\sigma = 2\pi b db$. The dependence of $d\sigma$ on the angle of scattering can be introduced as follows

$$d\sigma = 2\pi b(\chi)\left|\frac{db(\chi)}{d\chi}\right| d\chi\,. \tag{2.4}$$

The above described formalism can be applied to a Coulomb field. In this case $U = \alpha/r$ and after integration

$$\phi_0 = \cos^{-1}\frac{\alpha/mv_\infty{}^2 b}{\sqrt{[1+(\alpha/mv_\infty{}^2 b)^2]}}\,, \tag{2.5}$$

where $b^2 = (\alpha/mv_\infty{}^2)^2 \tan^2\phi_0$; after substituting $\phi_0 = \frac{1}{2}(\pi - \chi)$

$$b^2 = \left(\frac{\alpha}{mv_\infty{}^2}\right)^2 \cot^2\left[\frac{1}{2}\chi\right]. \tag{2.6}$$

Differentiation of the last expression with respect to χ and substitution into 2.4 produces the Rutherford equation

$$d\sigma = \pi\left(\frac{\alpha}{mv_\infty{}^2}\right)^2 \frac{\cos\left[\frac{1}{2}\chi\right]}{\sin^3\left[\frac{1}{2}\chi\right]}, \tag{2.7}$$

which is often written in the c.m. system as follows

$$d\sigma = \left(\frac{\alpha}{2mv_\infty{}^2}\right)^2 \frac{d\omega}{\sin^4\left[\frac{1}{2}\chi\right]}, \tag{2.8}$$

where $d\omega = 2\pi \sin\chi d\chi$.

In the semi-classical theory of Coulomb excitation the nuclei are assumed to follow classical trajectories and the excitation probabilities are calculated in time-dependent perturbation theory. At low energies one assumes Rutherford trajectories for the relative motion, while at relativistic energies one assumes straight-line motion. In intermediate-energy collisions, where one wants to account for recoil and retardation simultaneously, one should solve the general classical problem of the motion of two relativistic charged particles. The semi-classical solution can be deduced by using the relativistic Lagrangian

$$L = -m_0c^2\{1 - \frac{1}{c^2}(\dot{r}^2 + r^2\dot{\phi}^2)\}^{\frac{1}{2}} - \frac{Z_pZ_te^2}{r}. \tag{2.9}$$

But, even if radiation is neglected, this problem can only be solved if one particle has infinite mass [41]. This approximation is valid if we take the collision ^{32}Mg + ^{197}Au as our system. An improved solution may be obtained by use of the reduced mass $m_0 = m_pm_t/(m_p + m_t)$, where m_p and m_t are masses of projectile and target nucleus, respectively [36, 41].

For pure Coulomb excitation, where the charge distribution of the two nuclei do not overlap at any time during the collision, the excitation cross section can be expressed in terms of the same electromagnetic multipole matrix elements characterizing the electromagnetic decay of the nuclear states [34]. According to Winther and Alder [35], in most cases it is sufficient to assume that the relative motion takes place on a classical Rutherford trajectory, and the cross section for exciting a definite state $|f\rangle$ from the state $|i\rangle$ is given by

$$\left(\frac{d\sigma}{d\Omega}\right)_{\mathrm{CE}} = \left(\frac{d\sigma}{d\Omega}\right)_{\mathrm{Ruth}} P_{i\to f}\,, \tag{2.10}$$

where $P_{i\to f}$ is the probability of excitation from the initial state $|i\rangle$ to the final state $|f\rangle$. Assuming that the electromagnetic interaction potential $V(\boldsymbol{r}(t))$ is a time-dependent perturbation, $P_{i\to f}$ can be deduced as

$$P_{i\to f} = |a_{i\to f}|^2 \quad \text{with} \tag{2.11}$$

$$a_{i\to f} = \frac{1}{i\,\hbar}\int_{-\infty}^{\infty} e^{i\,\omega_{fi}\,t}\langle f|V(\boldsymbol{r}(t))|i\rangle\,dt\,, \tag{2.12}$$

where $\omega_{fi} = (E_f - E_i)/\,\hbar$. The amplitudes $a_{i\to f}$ can be expressed as a product of two factors

$$a_{i\to f} = i\sum_{\lambda}\chi^{(\lambda)}_{i\to f} f_\lambda(\xi)\,, \tag{2.13}$$

where the excitation strength

$$\chi^{(\pi\lambda)}_{i\to f} \simeq \frac{Z_p e\langle f|\mathcal{M}(\{\begin{smallmatrix}E\\M\end{smallmatrix}\}\lambda\mu)|i\rangle}{\hbar\{\begin{smallmatrix}v_p\\c\end{smallmatrix}\}{b_a}^{\lambda}}\,, \tag{2.14}$$

is a measure of the strength of the interaction,

$$\gamma = \frac{1}{\sqrt{1-\beta^2}} \quad \text{and} \quad \beta = \frac{v_p}{c}\,, \tag{2.15}$$

v_p the projectile velocity in the laboratory system, b_a is the distance of the closest approach in the collision and the function $f_\lambda(\xi)$ ($f_\lambda(\xi) = 1$ for $\xi = 0$ and $f_\lambda(\xi) \sim$

$e^{-\pi\xi}$ for $\xi \gg 1$) measures the degree of adiabaticity of the process in terms of the adiabaticity parameter ξ, which is defined as the ratio of the collision time

$$\tau_{\rm coll} = \frac{b}{\gamma v_p} \tag{2.16}$$

to the time of internal motion in the nucleus

$$\tau_{\rm nucl} = \omega_{\rm fi}^{-1} = \frac{\hbar}{\Delta E}\,. \tag{2.17}$$

Therefore Coulomb excitations are possible when $\xi < 1$. This limits intermediate-energy Coulomb excitation when $v \sim 0.3\,c$, $b \sim 15$ fm and

$$\xi \sim \frac{\Delta \mathrm{E}}{5\ \mathrm{MeV}}\,, \tag{2.18}$$

to the study of low-lying collective states with energies of several MeV. Such limitation can be avoided by using heavy projectiles ($Z_p \gg 1$) for excitation of collective states, where the strength parameter

$$\chi^{(\lambda)} \approx V_\lambda(b_a)\tau_{\rm coll}/\,\hbar\,, \tag{2.19}$$

which is measuring the action of the field, is larger than unity. In this case perturbation theory breaks down and multiple excitations may occur [35, 36].

The Coulomb excitation cross sections are usually calculated by integrating the excitation probability from a minimum impact parameter b_{min} to infinity. Final results can be deduced by introducing an adiabatic cutoff and integrating the absolute square of the excitation strength $|\chi|^2$ from b_{min} to b_{max}, instead of integrating $P_{if} = |\chi f(\xi)|^2$ from b_{min} to infinity:

$$\sigma = 2\pi \int_{b_{\rm min}}^{\infty} P_{if}\, b\, db \approx 2\pi \int_{b_{\rm min}}^{b_{\rm max}} |\chi|^2 b\, db\,, \tag{2.20}$$

where b_{max} is a function of transition energy ΔE

$$b_{max} = \frac{\gamma v}{w_{fi}} = \frac{\gamma\,\hbar\, v}{\Delta E}\,. \tag{2.21}$$

This produces an approximate expression for the excitation cross section as a function of the reduced transition probability $\mathrm{B}(\pi\lambda, 0 \to \lambda)$

$$\sigma_{\pi\lambda} \approx \left(\frac{Z_p e^2}{\hbar c}\right)^2 \frac{\mathrm{B_t}(\pi\lambda, 0 \to \lambda)}{e^2} \pi b_{min}^{2(1-\lambda)} \times \begin{cases} (\lambda-1)^{-1} & \text{for} \quad \lambda \geq 2 \\ 2\ln\left(\frac{b_{max}}{b_{min}}\right) & \text{for} \quad \lambda = 1 \end{cases} , \qquad (2.22)$$

where π is the parity and λ is multipolarity. In general, $\mathrm{B}(\pi\lambda, 0 \to \lambda)$ depends on the multipole operator for electromagnetic transitions ($\mathcal{M}(\pi\lambda\mu)$) as follows [31]:

$$\begin{aligned} \mathrm{B_t}(\pi\lambda, I_i \to I_f) &= \sum_{\mu M_f} |\langle J_f M_f | \mathcal{M}(\pi\lambda\mu) | J_i M_i \rangle|^2 \\ &= \frac{1}{2J_i+1} |\langle J_f \| \mathcal{M}(\pi\lambda) \| J_i \rangle|^2 , \end{aligned}$$

where $\langle J_f \| \mathcal{M}(\pi\lambda) \| J_i \rangle$ is the reduced matrix element.

The exact expression for the excitation cross section, summed over parities and multipolarities, was derived by Winther and Alder [35]

$$\sigma_{i\to f} = \left(\frac{Z_p e^2}{\hbar c}\right)^2 \sum_{\pi\lambda\mu} k^{2(\lambda-1)} \frac{\mathrm{B_t}(\pi\lambda, I_i \longrightarrow I_f)}{e^2} \left| G_{\pi\lambda\mu}\left(\frac{c}{v}\right)\right|^2 g_\mu(\xi(b_{min})) , \qquad (2.23)$$

where

$$\begin{aligned} G_{\mathrm{E}\lambda\mu}\left(\frac{c}{v}\right) &= i^{\lambda+\mu} \frac{\sqrt{16\pi}}{\lambda(2\lambda+1)!!} \left(\frac{(\lambda-\mu)!}{(\lambda+\mu)!}\right)^{\frac{1}{2}} \left(\left(\frac{c}{v}\right)-1\right)^{-\frac{1}{2}} \\ &\times \left(\frac{(\lambda+1)(\lambda+\mu)}{2\lambda+1} P_{\lambda-1}^{\mu}\left(\frac{c}{v}\right) - \frac{\lambda(\lambda-mu+1)}{2\lambda+1} P_{\lambda+1}^{\mu}\left(\frac{c}{v}\right)\right) \end{aligned}$$

for electric excitations ($\pi = \mathrm{E}$) and

$$G_{\mathrm{M}\lambda\mu}\left(\frac{c}{v}\right) = i^{\lambda+\mu+1} \frac{\sqrt{16\pi}}{\lambda(2\lambda+1)!!} \left(\frac{(\lambda-\mu)!}{(\lambda+\mu)!}\right)^{\frac{1}{2}} \left(\left(\frac{c}{v}\right)-1\right)^{-\frac{1}{2}} \mu P_{\lambda}^{\mu}\left(\frac{c}{v}\right) \qquad (2.24)$$

for magnetic excitations ($\pi = \mathrm{M}$), and $P_\lambda^\mu(x)$ are associated Legendre polynomials evaluated for $x > 1$. For $\mu < 0$ the following relations are applicable

$$G_{\mathrm{E}\lambda-\mu} = (-1)^\mu G_{\mathrm{E}\lambda\mu} \quad \text{and} \quad G_{\mathrm{M}\lambda-\mu} = -(-1)^\mu G_{\mathrm{M}\lambda\mu} , \qquad (2.25)$$

where μ is

$$\mu = M_f - M_i . \qquad (2.26)$$

In the present chapter we denoted $k = \frac{E_\gamma}{\hbar\, c}$, Z_p is the proton number of the projectile, $E_\gamma = \Delta E$ is the excitation energy, and $\mathrm{B_t}(\pi\lambda, I_i \longrightarrow I_f)$ is the reduced transition probability of the target nucleus. The MATHEMATICA code `boris_wi79.m` for cross section calculations is based on equation 2.23 and shown in Appendix A.

Finally, it is important to notice that the Coulomb excitation cross section is directly proportional to the reduced transition probability

$$\sigma_{i\to f} \;\propto\; \mathrm{B}(\pi\lambda, I_i \longrightarrow I_f)\ . \tag{2.27}$$

Consequently, for given $\pi\lambda$ and pure transitions the $\mathrm{B}(\pi\lambda)$ value can be extracted in a model-independent way from a cross section measurement. In the present review the relation between the cross section and the reduced transition probability for target excitation was obtained. The cross section for projectile excitation is given by the same formulas with B_t substituted by B_p and Z_p by Z_t [35].

The transition between an initial nuclear state J_i^π and a final state J_f^π is usually dominated by the lowest multipolarity allowed by angular momentum and parity selection rules [30, 31]. The angular momentum (triangle) selection rule for the λ-th multipole electromagnetic transition is

$$|J_f - J_i| \le \lambda \le J_f + J_i \tag{2.28}$$

and the parity selection rules are

$$\pi_i \pi_f = (-1)^\lambda \tag{2.29}$$

for electric and

$$\pi_i \pi_f = (-1)^{\lambda+1} \tag{2.30}$$

for magnetic transitions.

2.3 Angular Distribution

The angular distribution of γ-rays is important for the calculation of detection efficiency. A complete analysis of Coulomb excitation angular distributions is given in [39], here I will present only final results. The angular distribution $W(\theta)$ is given by

$$\begin{aligned} W(\theta) &= \sum_{\substack{k \text{ even},\mu \\ L,L'}} |G_{\lambda\mu}(\frac{c}{v})|^2 g_\mu(\xi)(-)^\mu \begin{pmatrix} \lambda & \lambda & k \\ \mu & -\mu & 0 \end{pmatrix} \\ &\quad \times \begin{Bmatrix} I_f & I_f & k \\ \lambda & \lambda & I_i \end{Bmatrix} F_k(L, L', I_{ff}, I_f)\, \sqrt{2k+1}\; P_k(\cos(\theta))\; \delta_L\, \delta_{L'}\;, \end{aligned} \tag{2.31}$$

where $P_k(\cos(\theta))$ are Legendre polynomials, and the Winther and Alder functions

$$\begin{aligned} g_\mu(\xi(b)) &= 2\pi \left(\frac{\omega}{v\gamma}\right)^2 \int_b^\infty \rho\, d\rho |K_\mu(\xi(\rho))|^2 \\ &= 2\pi \int_\xi^\infty |K_\mu(x)|^2\, x\, dx \\ &= \pi\xi^2 \left[|K_{\mu+1}(\xi)|^2 - |K_\mu(\xi)|^2 - \frac{2\mu}{\xi} K_{\mu+1}(\xi) K_\mu(\xi) \right] , \end{aligned}$$

$K_\mu(\xi)$ is a modified Bessel function and the $\gamma - \gamma$ correlation function $F_k(L, L', I_1, I_2)$ depends on Clebsch-Gordan and Racah coefficients as follows [39, 42]

$$\begin{aligned} F_k(L, L', I_1, I_2) &= (-)^{I_1+I_2-1} \sqrt{(2k+1)(2I_2+1)(2L+1)(2L'+1)} \\ &\quad \times \begin{pmatrix} L & L' & k \\ 1 & -1 & 0 \end{pmatrix} \begin{Bmatrix} L & L' & k \\ I_2 & I_2 & I_1 \end{Bmatrix} . \end{aligned} \tag{2.32}$$

In the Coulomb excitation data analysis we express the angular distributions as

$$W(\theta) = \sum_{k \text{ even}} a_k P_k(\cos(\theta)) , \tag{2.33}$$

and use MATHEMATICA [43] for the calculation of the coefficients a_k as demonstrated in Appendix B.

2.4 Experimental Cross Sections

The cross section is an experimentally observable parameter which is often measured in nuclear physics. The Coulomb excitation cross section σ to a bound state is defined as the ratio of the number of detected de-excitation photons N_γ from this state to the product of efficiency ϵ_{tot}, the number of incoming beam particles N_b and the number of target nuclei per unit area N_t,

$$\sigma = \frac{N_\gamma}{\epsilon_{\rm tot}} \frac{1}{N_b N_t} \,. \tag{2.34}$$

The number of target nuclei per area N_t is calculated as a product of Avogadro's number ($N_A = 6.02{\cdot}10^{23}$ 1/mole) and target areal density ρ (in g/cm^2) divided by the atomic mass A (in g/mole) of the target material,

$$N_t = \frac{N_A \cdot \rho}{A} \quad . \tag{2.35}$$

Incident flux calculations are presented in 3.5.2. The efficiency is more difficult to determine because photons can escape without detection mostly due to imperfect geometry of the detector and the statistical nature of the interaction of γ-rays with matter. A detailed discussion on the interaction of γ-rays with matter is presented in 3.4.

2.5 Doppler Shift

At intermediate energies ($v_p \sim 0.3c$) relativistic effects become noticeable ($\gamma = 1.0483$), photons emitted from the "moving" or projectile frame have different energies in the "stationary" or laboratory frame. The relation between the γ-ray energy in the projectile (E_p) and laboratory (E_{lab}) frames is affected by Doppler shift as follows

$$E_p = \gamma E_{lab}(1 - \beta \cos(\theta_{lab})) \,, \tag{2.36}$$

where θ_{lab} is the angle between the direction of motion of the particle and the direction of the γ ray as measured in the laboratory, β is the beam velocity in units of the speed of light, and γ is the Lorentz factor. For the photons emitted from target excitation Doppler correction is not necessary.

Experimental parameters such as spread in beam velocities $\Delta\beta$ [21, 39] and energy loss in the target contribute to the uncertainty in the measured γ-ray energy (energy resolution) as follows

$$\left(\frac{\Delta E_{lab}^{(\gamma)}}{E_{lab}^{(\gamma)}}\right)^2_{\text{dopp}} = \left(\frac{\cos(\theta_{lab})}{1-\beta\cos(\theta_{lab})} - \beta\gamma^2\right)^2 \Delta\beta^2 + \left(\frac{\beta\sin(\theta_{lab})}{1-\beta\cos(\theta_{lab})}\right)^2 \Delta\theta^2 \,. \quad (2.37)$$

Chapter 3

Experimental Setup and Main Principles of Data Analysis

This chapter contains a general description of the NSCL facility [44] and the NSCL NaI(Tl) array [45]. The schematic layout of the NSCL facility is presented in Figure 3.1. While a complete discussion on the experimental beams will be presented in chapter 4, I will present a short introduction here, which is necessary for a better understanding of the experimental technique [21]. Primary beams were produced with the NSCL superconducting electron cyclotron resonance ion source (SECR) and the K1200 cyclotron. Secondary beams were produced via fragmentation of calcium and argon primary beams in a ^{9}Be primary target, located at the mid-acceptance target

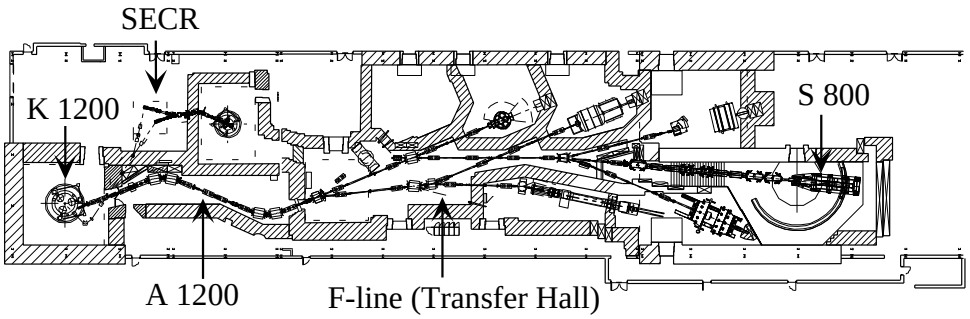

Figure 3.1: Schematic layout of the NSCL facility [46].

position of the A1200 fragment separator [47] and delivered onto a ^{197}Au secondary target, located in the center of the NSCL NaI(Tl) array. The experimental setup, the background reduction procedures, and principles of data analysis will be presented in this chapter. A review of position, energy and efficiency calibrations for the NSCL NaI(Tl) array will be given.

3.1 Exotic Nuclear Beams

There are ∼300 stable and up to 8000 radioactive isotopes in nature. The study of radioactive isotopes is one of the frontiers in modern physics. The nuclear properties of stable isotopes are mostly known. Radioactive isotopes often have short half-lives and because of that it is very difficult or often impossible to manufacture a target made of a radioactive species for studies. Radioactive nuclear beams overcome this problem and the only limiting factor is the time of flight, which should be less than the life time. There are two main methods of radioactive nuclear beam production [48]: isotope separation on-line (ISOL) and nuclear fragmentation. ISOL facilities such as the ISOLDE mass separator at CERN use sophisticated chemistry for the extraction of radioactive nuclei with half-lives up to few msec from the production (primary) target [49] [1] .

3.1.1 Nuclear Fragmentation

Chemical selectivity and microsecond life times of radioactive isotopes are not problems for nuclear fragmentation facilities such as MSU, RIKEN, GANIL, and GSI; because of the quick physical separation of wanted and unwanted isotopes (∼10^{-6} sec). Re-acceleration of the radioactive ions is not necessary since the fragmentation

[1] The shortest-lived isotope studied up to date at ISOLDE (^{14}Be) has a half-life time of only 4.3 msec [50].

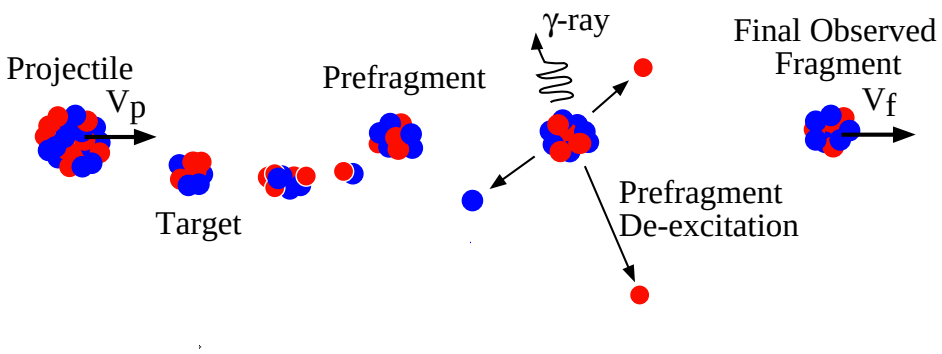

Figure 3.2: Schematic illustration of nuclear fragmentation.

products have essentially the primary beam velocity. Nuclear fragmentation was first described by Serber [51] as a peripheral, highly energetic, two-step heavy-ion reaction in which each step occurs in clearly separated time intervals graphically illustrated in Figure 3.2. The first step consists of the initial collision between the constituents of the target and projectile nuclei and occurs within $\sim 10^{-23}$ sec. This can create highly excited objects (prefragments) which lose their excitation energy through the emission of nucleons (neutrons, protons, small clusters) and γ-rays. The second step (de-excitation) proceeds slowly relative to the first step ($\sim 10^{-17}$ sec) and depends on the excitation energy of the prefragrament. A disadvantage of this beam production technique is poor quality of beams due to large emittance.

3.1.2 Fragment Separation

The A1200 fragment separator was constructed at the NSCL [47] to separate out the radioactive beams of interest. Figure 3.3 presents the fragment separator which is achromatic with two intermediate images between two sets of dipoles that bend in opposite directions. Two images allow for the use of degrading wedges and provide space for momentum measurement. Since nuclear fragmentation beams, such as those produced in the A1200, may contain more than one isotope it is necessary to identify them on an event-by-event basis. A typical pattern of isotopes produced by the A1200

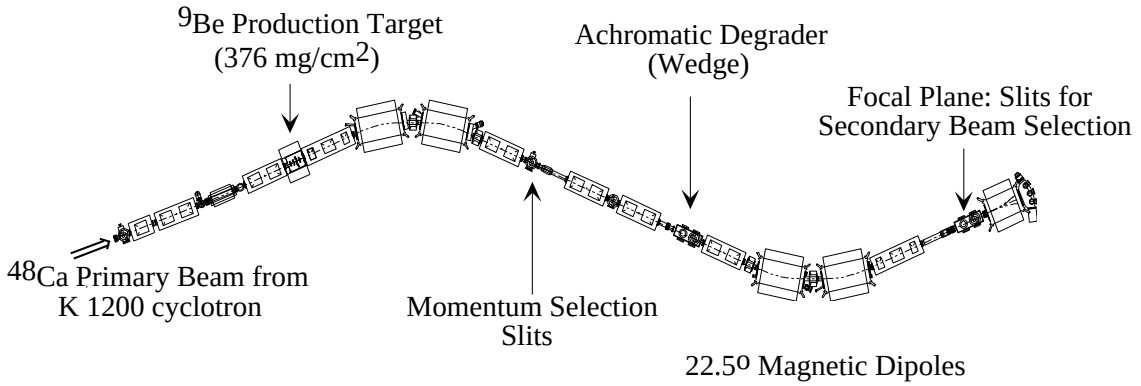

Figure 3.3: The A1200 fragment separator of the NSCL. A ^{48}Ca primary beam strikes a ^{9}Be production target and produces a variety of light nuclei. The radioactive beam of interest is selected by using two sets of dipole magnets [46].

fragment separator is presented in Figure 3.4.

For the identification of the isotope of interest several techniques can be used. A time of flight (TOF) method in combination with an energy loss measurement and knowledge of the magnetic rigidity (Bρ) of the A1200 allows the identification of the beam particle before the secondary target. The magnetic rigidity is measured in [Tesla·meter] and is equal to the momentum of the particle divided by its charge[2] . The TOF method is based on the measurement of velocity of the projectile nucleus using the time signals from two separate detectors. For this purpose a thin plastic scintillator located after the A1200 focal plane and a PIN silicon detector placed before the NaI(Tl)-array (secondary target area) can be used. The PIN detector, which is described in 3.2.3, is also good for energy loss (δE) measurements, which uniquely define the atomic number of the nuclear fragment. This Z-measurement is based on the fact that energy losses in the thin absorbers are small and the velocity of the projectile (β) is roughly constant. The mean energy loss, of the fully stripped

[2]It is convenient to express magnetic rigidity as $B\rho = 3.10715 \cdot \frac{A}{q}\left[\left(\frac{E}{931.5}\right)^2 + \frac{2E}{931.5}\right]^{0.5}$ [52], where A is a number of nucleons, q is the charge of the isotope and E is an energy in MeV/nucleon.

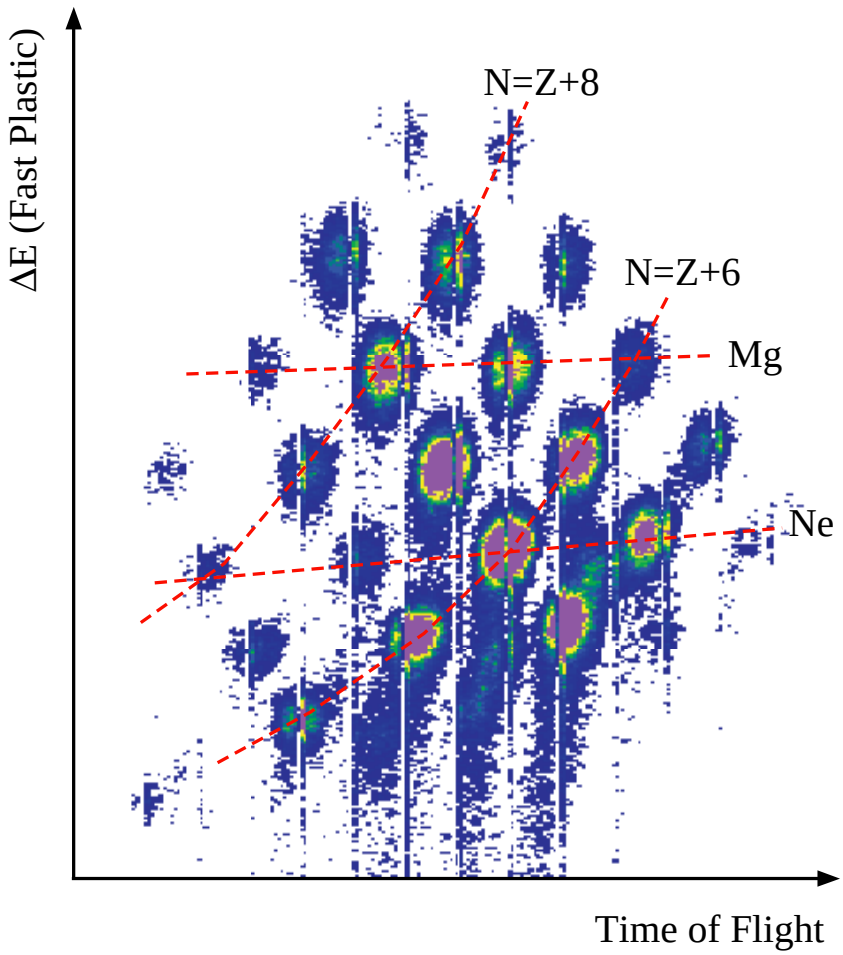

Figure 3.4: Typical isotope identification pattern. Energy losses in a thin fast plastic scintillator are plotted vs. time of flight. Light isotopes were produced by fragmentation of a ^{48}Ca primary beam on a ^{9}Be target at 80 MeV/nucleon (Bρ = 3.15 T·m).

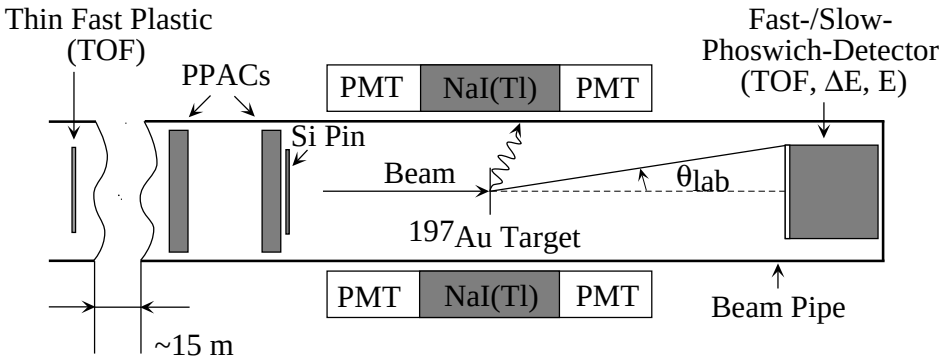

Figure 3.5: Schematic view of the experimental apparatus around the secondary target.

nucleus, can be approximated by the Bethe-Bloch formula [53]:

$$\delta E = 2\pi N_a {r_e}^2 m_e c^2 \rho \frac{z}{a}\left(\frac{Z}{\beta}\right)^2 x\,, \tag{3.1}$$

where are $2\pi N_a {r_e}^2 m_e c^2 = 0.1535$ MeV cm^2/g and ρ, z and a are properties of the absorbing material and x is the absorber thickness. At the same time, it is important to know the isotopic composition of the beam after the secondary target because nuclear reactions can take place in the target. Such information is necessary for the identification of gamma rays from the isotope of interest. For this purpose, we measure the energy loss and total energy of each nuclear fragment in the Coulomb excitation experiments with the plastic phoswich detector (discussed in subsection 3.2.2), located at zero degrees with respect to the beam.

3.2 Experimental Setup

The experimental apparatus (NSCL NaI(Tl) array, silicon PIN, TOF and ΔE/E and tracking detectors) was located on the F-line in the transfer hall of the NSCL. A schematic view of the experimental apparatus is presented in Figure 3.5. The position and direction of each fragment incident on the 702 and 518 mg/cm^2 secondary gold

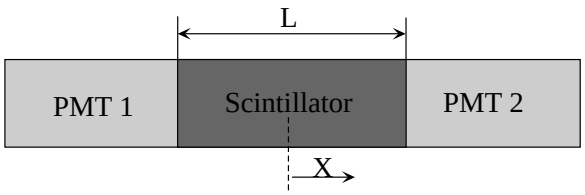

Figure 3.6: One-dimensional position sensing by light division in the position-sensitive NaI(Tl) crystal.

targets were measured with two parallel-plate avalanche counters (PPAC) [54] and identified in the phoswich detector. Photons were measured in coincidence with the scattered beam fragments by the NSCL NaI(Tl) array [45].

3.2.1 The NSCL NaI(Tl) Array

The NSCL NaI(Tl) array consists of 38 detectors, which are arranged in 3 concentric rings, of 11 (inner), 17 (middle) and 10 (outer) detectors, respectively. The radii of the three detector rings are 10.8 cm, 16.9 cm and 21.8 cm, respectively. The crystals are cylindrical, approximately 18.0 cm long and 5.75 cm in diameter and placed into a 0.45 mm thick aluminum shield. A 1 cm thick quartz window is attached to each end. Optical glue was used to connect 5 cm in diameter photomultiplier tubes (PMTs) to each window. To shield the NaI(Tl) detector array from photons originating at the phoswich detector, the PPACs, and natural radioactivity, the entire array was placed into a 16 cm thick lead shield.

In intermediate-energy Coulomb excitation experiments with radioactive nuclear beams, position sensitivity of the γ-array is necessary for Doppler shift correction of the photons' energies and has been presented in section 2.5. For sensing position in one dimension, long cylindrical crystals can be used with PM tubes positioned at each end as illustrated in Figure 3.6. For this geometry, the intensity of light measured at each end of the crystal drops off exponentially with the distance from the origin of the scintillation light [55]. Thus, the signal amplitude $E_1(E_2)$ for PMT1(PMT2) is

given by

$$E_1 = \frac{E_\gamma P}{E_0}\exp[-\alpha(L/2+x)] \tag{3.2}$$

$$E_2 = \frac{E_\gamma P}{E_0}\exp[-\alpha(L/2-x)]\,, \tag{3.3}$$

where E_γ is the energy deposited by the γ-ray, P is probability that a light quantum produced at one end will generate a photoelectron in an adjacent tube, E_0 is the energy deposited per photon created in the scintillator and α is the light attenuation coefficient and x is the distance between the end of the crystal and the origin of the scintillation light. The position of the interaction can be found by

$$x = \frac{1}{2\alpha}\log\frac{E_2}{E_1} \;\sim\; \log\frac{E_2}{E_1}\,. \tag{3.4}$$

It is convenient to keep x always positive by introducing an additional offset of 2000, which will be discussed in subsection 3.3.2. By multiplying equations 3.2 and 3.3, we find the deposited energy E_γ is independent of the position within the crystal

$$E_\gamma = \sqrt{E_1 E_2}\frac{E_0}{P}\exp[\alpha L/2] \;\sim\; \sqrt{E_1 E_2}\,. \tag{3.5}$$

3.2.2 Zero-Degree Detector

After passing through the secondary target, the secondary beams are stopped in a cylindrical fast-slow plastic phoswich detector (called the zero-degree detector, or ZDD) which allowed charge identification of the secondary beam particles. The secondary beams are often run in "cocktails" which contain several species in a single separator setting. The ZDD and time of flight measurements in the beam line provide positive isotope identification. In addition, the zero-degree detector serves the following purposes:

- Provides a trigger and time signal for particle-γ coincidences.
- Selection of beam particles scattered into laboratory angles $\leq \theta_{lab}$.
- Counts the number of nuclear fragments during the experiment.

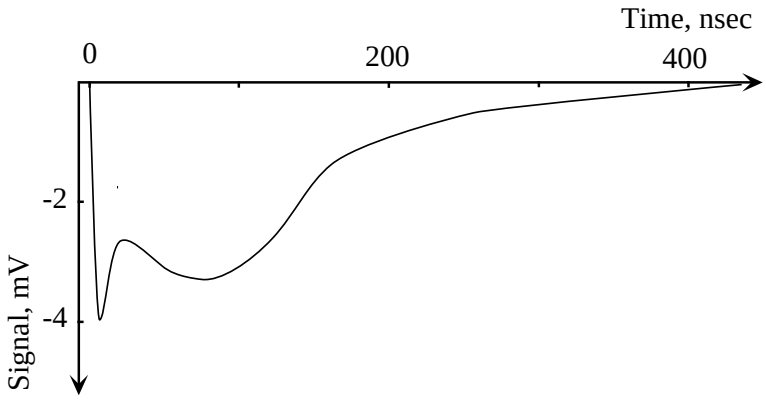

Figure 3.7: Schematic time characteristics of the phoswich zero-degree detector.

The phoswich detector has a diameter of 101.6 mm and is made of 100 mm thick slow plastic scintillator (Bicron 444) and a thin layer (0.6 mm thick) of fast plastic scintillator (Bicron 400) is glued to it. The zero-degree detector is viewed through a lightguide by 2 PMTs (THORN EMI ElectronTubes 9807B02). The PMTs were attached by using Tracon F113 epoxy. In addition, a water cooling system was installed to cool down the PMT voltage dividers [56] because the detector operates in a vacuum. To improve the light collection, 1.5 μm aluminized polyester foil was placed on the front part of the detector, and Teflon tape and reflecting paint (Bicron 620) were used on its side.

Figure 3.7 illustrates that ZDD signals consist of two different time components. The thin fast plastic is responsible for a sharp ($\sim$10 nsec) pulse at the beginning of the time scale and the slow plastic produces rather broad ($\sim$400 nsec) pulse. The different time responses in combination with pulse shape discrimination allow the use of one PMT for detection of both signals.

The thickness of the fast plastic was chosen so that fragments would lose up to 20 % of their energy and their velocity would be roughly constant. For example, after passing through the thin fast plastic scintillator, ^{32}Mg ions at 49 MeV/A will lose 5.8% of their kinetic energy and ^{30}Mg ions with 26.1 MeV/A will lose 20.7% of theirs. Equation 3.1 indicates that energy losses in the fast plastic provide an opportunity to

measure Z for each fragment. Time of flight (fragment mass) measurements are based on the start signal from the thin fast plastic scintillator located after the A1200 focal plane and stop signal from the phoswich as shown in Figure 3.5. The rate capability of the phoswich is as high as 50,000 - 70,000 ions/sec. It is convenient to present the zero-degree detector data as follows:

- Energy loss in thin fast plastic scintillator versus time of flight (for nuclear fragment identification and corresponding gates for particle-γ coincidences).
- Energy loss in thin fast plastic versus slow plastic scintillator (to test that particular nuclear fragments are passing through the secondary target, if some of the fragments are missing the target then the $\Delta E/E$ spectrum has two particle groups with the same ΔE but different E values).
- Energy loss in slow plastic scintillator versus time of flight (for separation of the isotopically pure secondary beams).

3.2.3 Fragment Identification with Silicon Detector

The basic ideas behind fragment identification in a thin ($\sim 300\mu m$) silicon detector are the same as in the case of the thin fast plastic scintillator. Moreover, silicon detectors have better energy resolution and the detector response function is more uniform over the active area of the detector.

The silicon detector data also provides an additional possibility for fragment identification. From the Bethe-Bloch formula (see equation 3.1), the ratio of energy loss for two different fragments in the cocktail beam is

$$\frac{\delta E_1}{\delta E_2} \approx \left(\frac{Z_1 \beta_2}{Z_2 \beta_1}\right)^2, \tag{3.6}$$

where β_1, β_2 are fragment velocities and Z_1, Z_2 are their respective electric charges. The same ratio can be experimentally measured as a ratio of vertical positions of the particle group centroids, when energy losses are plotted versus time of flight

Table 3.1: Ratio of energy losses in the silicon detector for different nuclei.

Nuclei	Calculated Ratio of Energy Losses	Measured Ratio of Energy Losses
^{35}Al/^{32}Mg	1.195	1.187(32)
^{32}Mg/^{29}Na	1.216	1.221(34)
^{29}Na/^{26}Ne	1.242	1.250(34)

(see Figure 3.4). Table 3.1 demonstrates a successful test of this method of particle identification with secondary beams from ^{48}Ca.

3.2.4 Electronics

The basic electronics setup for Coulomb excitation experiments was already described in [39, 45]. In Figure 3.8 I will present the set of nuclear electronics which was used in the present experiments.

In general, nuclear fragments produce photons while passing through the secondary target and some of those photons interact with NaI(Tl) crystals. PMTs convert scintillations (optical signals) into electrical signals, which are directed into custom built NSCL/MSU fast amplifiers and splitters. The splitter produces two data streams which are used for recording of timing and energy information. The first data stream is directed into a constant fraction discriminator (LeCroy 3420 or MSU 1806), which is used for an event trigger, timing and scaler signals. The second data stream is directed into a 16-channel CAMAC shaping amplifier with a shaping time of about 5 μsec (Pico systems) and signals are digitized in 16-channel CAMAC peak-sensing ADCs (Phillips Scientific 7164H). The signals from the zero-degree detector are amplified and split into three different paths. The first group of signals is directed into

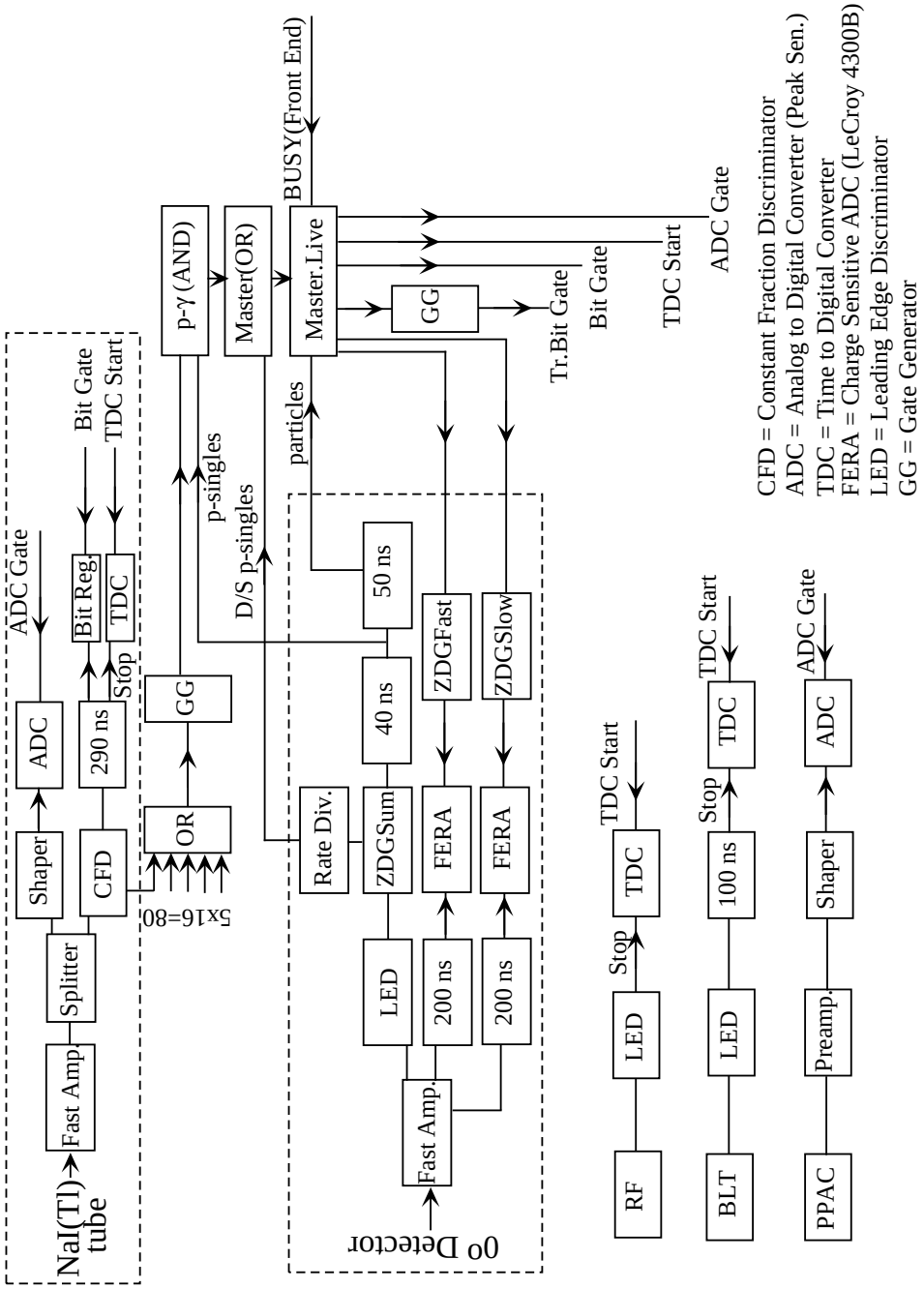

Figure 3.8: Electronics Diagram.

Leading Edge Discriminator (LED) and used for determination of the beam intensity and particle-γ coincidences. The second and third groups are delayed and directed into the first and second QDCs (FERAs), which are gated on the zero-degree fast and zero-degree slow gates, respectively.

The event trigger requires two simultaneous signals within $\leq$200 nsec from any of the NaI(Tl)-crystals and the zero-degree detector. The coincidences between γ-signals from the CFDs and particle signals from the phoswich detector were realized in the Quad four-fold coincidence unit (Phillips Scientific 755), which contains particle-γ coincidence, master-gate and master-gate-live signals. The master-gate-live signal produces an ADC gate, a trigger-bit gate, a bit gate, a TDC-start signal and gate for the zero-degree detector QDCs (LeCroy 4300B).

CAMAC crates are read out via crate controllers (Bi-Ra systems). The VME crate contains the Master processor, the Slave processor and a Branch driver, which perform following functions:

- Master broadcasts data over ethernet.
- Slave sends commands to CAMAC modules through the branch driver.
- Branch Driver connects the slave to the CAMAC modules via the branch highway cables and crate controllers.

The data is collected by DEC 300 alpha workstations via ethernet and recorded onto DLT and 8 mm tapes. The dead time of the data acquisition system arises from the fact that a typical event read-out time is $\sim$300 μsec. The front end produces a veto signal for the master-gate-live unit when it processes an event. Typical data acquisition rates for the ^{48}Ca secondary beams were $\sim$500 events/sec with a life time of 99.8%. The high voltage ($\sim$+1400 V) for the NSCL NaI(Tl)-array was provided by a multi-channel power supply (LeCroy Systems 1440).

3.3 Calibration and Gain Matching of the NaI(Tl) Detectors

Position, energy and efficiency calibrations are an important part of the data analysis. The ideas behind the calibrations are the topic of this section and a detailed description of the corresponding procedure is presented in Appendix C.

3.3.1 Gain Matching

The gain matching of PMTs in the NaI(Tl) array, which usually precedes the calibrations, was performed with a collimated γ-ray source placed in the center of the array. The collimator consists of two "HeviMet" (tungsten/copper alloy) cylinders each 7.62 cm long and 14 cm in diameter arranged co-axially with a 4.6 mm gap in between. A 0.5 MBq ^{60}Co source is centered between the two cylinders. An aluminum stick with glued measuring tape is attached to one of the cylinders. The gain matching procedure with the collimated source in the center of the array was conducted as follows:

- The voltage for each phototube was adjusted to produce a negative $\sim$70 mV response signal into 50 Ohm impedance.
- The shaper gains were adjusted to produce simultaneously an energy calibration of $\sim$2 keV/channel (see equation 3.5) and a position peak in channel $\sim$2000 (see equation 3.4).

A typical position spectrum is shown in Figure 3.9 and typical gain-matched γ-spectrum of ^{88}Y is shown in Figure 3.10.

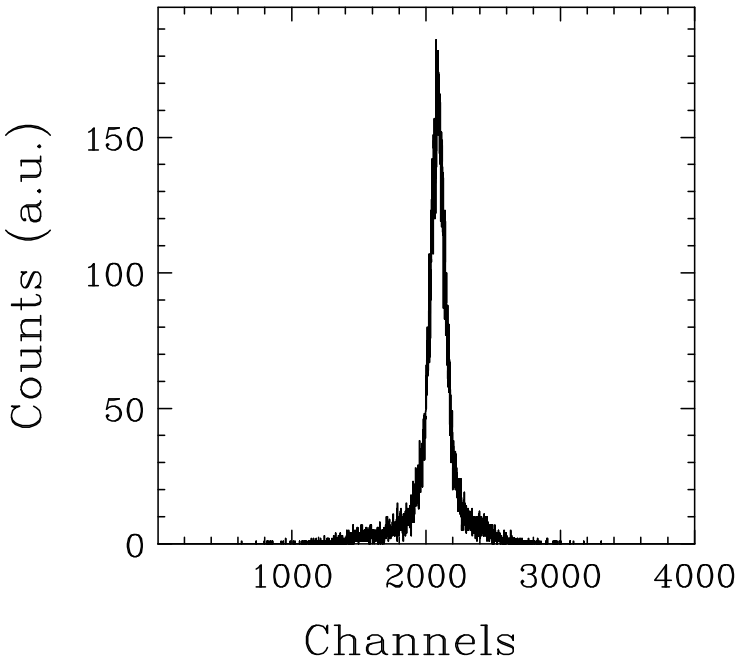

Figure 3.9: Position spectrum of a NaI(Tl) detector.

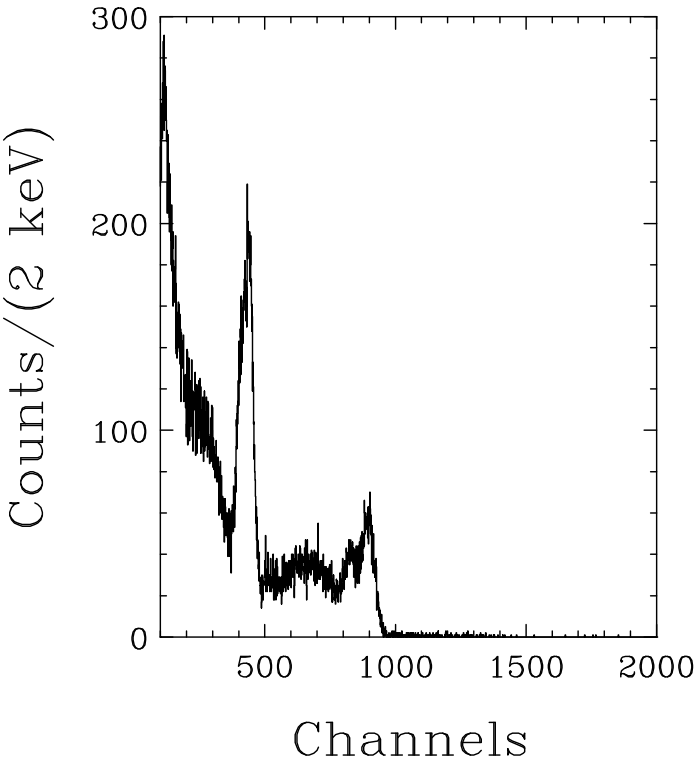

Figure 3.10: The γ-spectrum of ^{88}Y in a NaI(Tl) detector.

3.3.2 Position Calibration

The position calibration of the array is required for the Doppler correction of the photon energy and efficiency calculations. A detailed description of the position calibration procedure is presented in Appendix C.1.

The position calibrations are usually performed before and after the Coulomb excitation experiments by moving a collimated γ-source through the center of the NaI(Tl) array and measuring the detector response. The whole collimator can be inserted into the beam pipe for simultaneous position calibration of the entire array. A reference location for the NSCL NaI(Tl) array is the beam pipe flange. A typical position calibration is done in steps of 1.27 cm and signals from both PMTs for each detector and the geometrical position of the collimated source are recorded by the data acquisition system.

The SMAUG histogrammer [57] is used to produce 1-dimensional spectra of the reconstructed position. The reconstructed position was pameterized as

$$X_r = 2000 + 1000 \cdot \log(Y_1/Y_2)\,, \tag{3.7}$$

where (Y_1/Y_2) is the ratio of PMT signals for each detector. A typical position spectrum is shown in Figure 3.9. The offset of 2000 was added into equation 3.4 for convenience (to avoid negative numbers for X_r). Peaks in the position spectra were fitted with the GF2 (GeLi Fit) peak fitting program [58]. The detector's response was fitted in PHYSICA [59] with a third order polynomial

$$X_r = a + b \cdot x + c \cdot x^2 + d \cdot x^3\,, \tag{3.8}$$

where a is the offset and b, c, d are fit parameters. The parameterization of the detector position response is appropriate for the center of the detector. This polynomial also includes the turnover of the curve close to the edges of the detector. However, edge-related effects (due to non-uniform conditions for light collection) are definitely

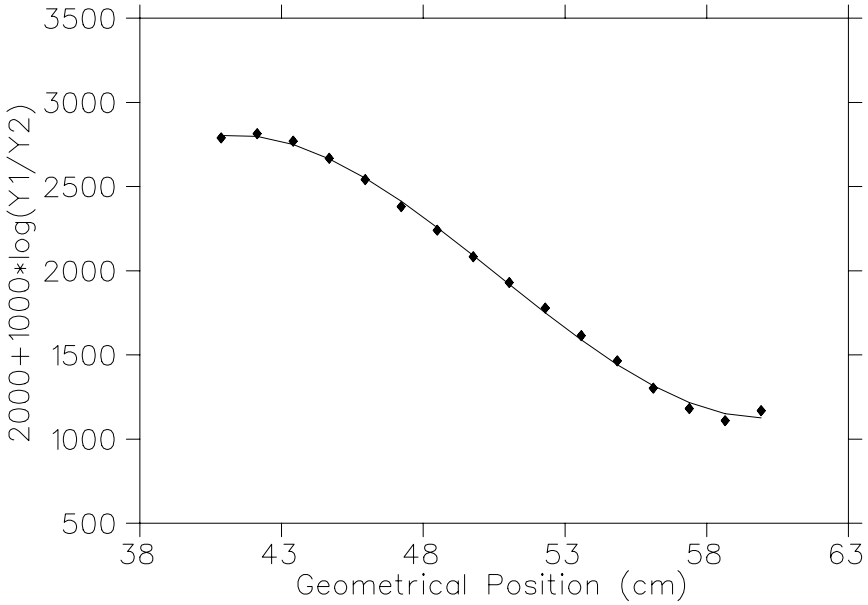

Figure 3.11: Position response of a NaI(Tl) detector. The reconstructed position (see equation 3.7) is plotted versus geometrical position with respect to the beam pipe flange for any γ-ray from a ^{60}Co source.

present and the curve flattens there. These regions close to the edges are excluded from the data analysis.

Figure 3.11 shows the position response for detector #3 plotted versus geometrical position.

This procedure produces an average position resolution of about 2 cm and an angular resolution of emitted photons for the inner-ring detectors better than 10°. This angular uncertainty yields an uncertainty in the reconstructed energy of about 5% (see equation 2.37),which is small compare to the intrinsic detector resolution of 8%.

3.3.3 Energy Calibration

Differences between the NaI(Tl)-detectors and the dependence of the uncalibrated energy on position creates a need for a position-dependent energy calibration as demonstrated in Figure 3.12 for detector #3.

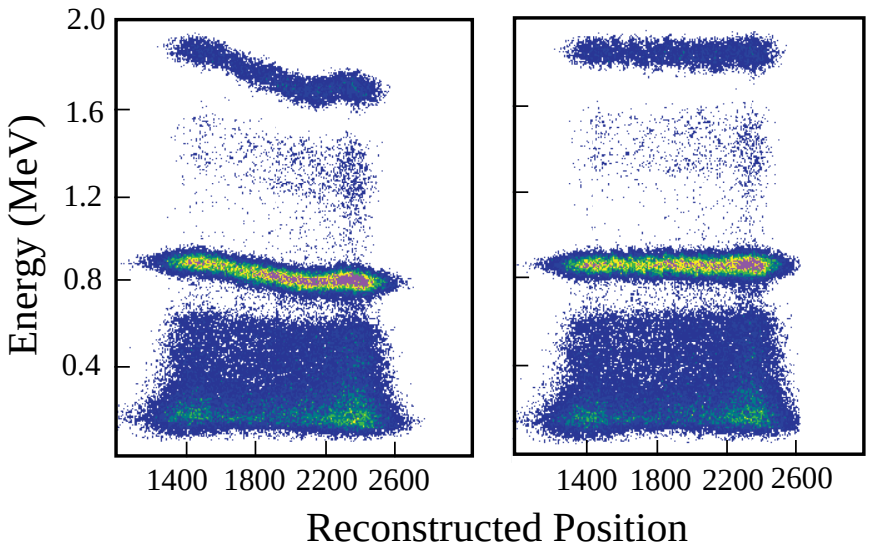

Figure 3.12: Position-dependent energy calibration. The left panel shows the measured energy versus position for an ^{88}Y source before application of a position-dependent energy calibration. The right panel depicts the same spectrum after the position-dependent energy calibration.

Suitable photon sources for the energy calibrations of NaI(Tl) crystals are ^{22}Na and ^{88}Y, because they have two well-separated and easily-identifiable γ-lines. Among other γ-sources, ^{228}Th is valuable because of its high-energy (2.614 MeV) and low-energy (0.24 MeV) γ-lines. In the current thesis, energy calibrations were done by using ^{22}Na (0.511 and 1.275 MeV) and ^{88}Y (0.898 and 1.836 MeV) γ-sources. Each detector was split into 20 virtual slices of reconstructed position (see equation 3.7) with a photon multiplicity of one (meaning that only one detector in the array triggered). A typical γ-spectrum of ^{88}Y collected for one slice is shown in Figure 3.13. Experimental details are described in Appendix C.2.

Photoabsorption peaks [53, 55] from the γ-transitions in the calibration sources were fit with the GF2 routine. Their centroid positions are plotted for each slice as measured energy versus known energy and fit in PHYSICA with a linear fit. The linear fit reflects the fact that the response function of the NaI(Tl) detector is close to linear over most of the energy range significant in this work [55]. The immediate impact

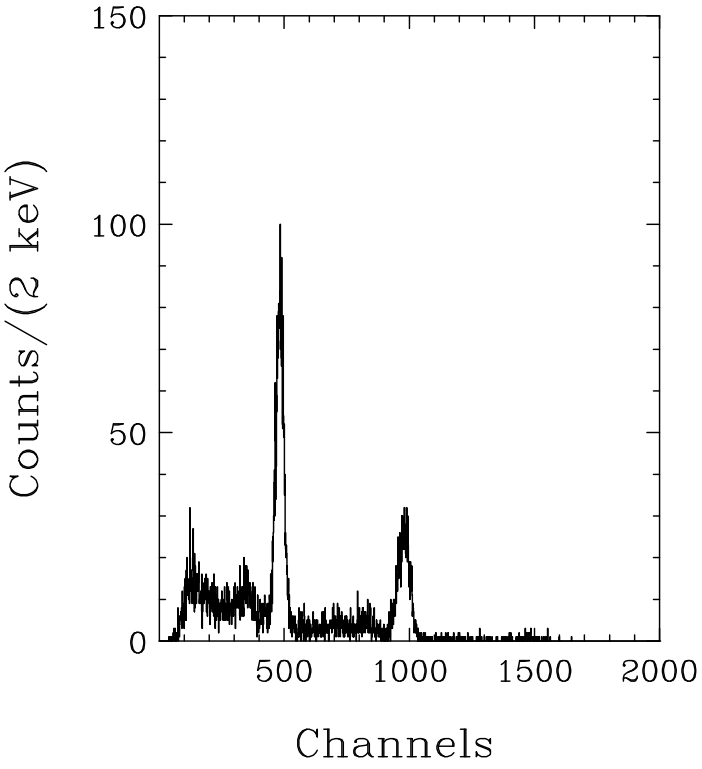

Figure 3.13: The γ-spectrum of ^{88}Y collected for one slice.

of the position-dependent energy calibration is demonstrated in the right panel of Figure 3.12. The energy resolution of a typical detector is usually $\sim$8% at 662 keV. The position-dependent energy calibrations were tested in-beam by comparing the experimentally measured (calibrated) energies for transitions in the projectile and laboratory frames in the ^{197}Au target ($E_\gamma = 547.3(5)$ keV) and ^{36}Ar projectile ($E_\gamma =$ 1971.2(2.0) keV) with the known energies: 547.5 keV and 1970.4 keV (see discussion on the test beam experiment in section 4.2).

3.3.4 Stability of Calibrations

The stability of the array calibrations during the experiment is important for successful measurements. In our case, the NaI(Tl) detectors' instability is mainly defined by an instability of the photomultiplier tubes, which have gains on the order of 10^6. An

overall gain for a PMT is defined by [55]

$$Gain = \alpha\delta^N \,, \tag{3.9}$$

where α is the fraction of all photoelectrons collected by the multiplier structure, δ is a number of electrons produced by the first dynode for each incident photoelectron and N is the number of stages. Equation 3.9 implies that the tube's gain is a sensitive function of the applied voltage V. For conventional dynodes, δ varies as some fractional power of the interdynode voltage so that for a 10-stage tube the overall gain is typically proportional to $V^6 - V^9$.

Three major factors can contribute to PMT gain instability during the experiment:

- High voltage power supply instability.
- Temperature and humidity variations.
- External magnetic fields.

In the present thesis experiments an air conditioner in the transfer hall was not operational and the array was in a hot and humid environment. During the calibrations conducted after completion of the experiments a sliding door to the vault was open and the temperature change led to 3-5 % PMT gain increase over the next 24 hours. This phenomenon was recognized during the data analysis and only position calibrations and ^{22}Na-energy calibration data (collected in the first 4 hours after the Coulomb excitation experiments) were used. The remaining calibration data came from the measurements performed before and during the experiments.

3.4 Efficiency Estimations

The following is a description of the efficiency calibrations for the NSCL NaI(Tl) array. A good knowledge of the array's efficiency ϵ_{tot} is important for a precise determination of excitation cross sections (see equation 2.34).

3.4.1 Efficiency for an Isotropic Source

In general, the detection efficiency is a function of photon energy and detection geometry (overlap between the angular distribution of the γ-rays and the detector geometry). Assuming that photons are emitted from the center of the target, the efficiency for a certain fixed angle (θ,ϕ) and energy E_γ is given by

$$\epsilon = \epsilon(E_\gamma, \theta, \phi) = \frac{\#\text{ of detected } \gamma\text{-rays of energy } E_\gamma \text{ with direction } (\theta,\phi)}{\#\text{ of emitted } \gamma\text{-rays of energy } E_\gamma \text{ into direction } (\theta,\phi)}. \quad (3.10)$$

In the current thesis, calibrated radioactive sources of ^{22}Na, ^{88}Y and ^{228}Th (see Appendix C.3), placed in the secondary target position, were used to measure the position- and energy-dependent detector efficiency. The interaction of γ-rays with matter has been described by many authors [53, 55] and I will present only a short summary. At low energies, the photoelectric process (photon absorption by atomic electrons and further emission of electrons by atoms) dominates the total cross section. Compton scattering, which reduces the photon energy by producing electron recoils, becomes dominant in the approximately 0.2-5 MeV energy range. Pair production has a threshold of 1.022 MeV and is important for high energy photons. Coherent scattering, which preserves the energy of photons, is important for so-called narrow beam experiments, where both the source and the detector are well collimated, and this is not the case for secondary beams. In this work we used the efficiency of total absorption, i.e. a photon is absorbed in a single crystal due to photoeffect or multiple scattering effects followed by the photoeffect. Consequently, the number of counts under the photoabsorption peak indicates the total number of absorbed photons.

The efficiency for an isotropic angular distribution was deduced from the experimentally measured photoabsorption peak efficiencies for different energies as follows

$$\epsilon(E_\gamma)^{(\mathrm{iso})} = \frac{1}{4\pi} \int_\Omega \epsilon(E_\gamma, \theta, \phi)\, d\Omega\,. \quad (3.11)$$

This is integrated over the solid-angle range (Ω) efficiency with the weight ($= \frac{1}{4\pi}$).

To calculate the efficiency for an isotropic source each detector was split into 10 virtual slices over calibrated position (approximately 18 mm each). Depending on the individual detector and the experiment, the first and last slice were discarded in the data analysis and efficiency calibrations due to poor energy resolution. Efficiency calibration data were analyzed for each slice and photoabsorption peaks were fit using the GF2 routine [58]. The total number of counts under each peak, combined with the length of the measurements and the data acquisition live time was divided by the intensity for the particular γ-line. This intensity is equal to the source activity multiplied by the branching ratio for the particular γ-line. This procedure yields an experimental efficiency for each slice (differential efficiency $\epsilon(E_\gamma, \theta, \phi)$). Finally, the total array efficiency ($\epsilon^{(\mathrm{iso})}(E_\gamma)$) was obtained as a sum of the differential efficiencies. The measured total efficiency of the array was fitted in Physica [59] with an efficiency function of the form

$$\epsilon(E_\gamma)^{(iso)} = exp(-(A + B{\cdot}log(E_\gamma/E_0))){\cdot}exp(C/(log(E_\gamma/E_0)))\,, \tag{3.12}$$

where A, B and C are fit parameters and $E_0 = 50$ keV. The second factor accounts for low-energy ($\leq$400 keV) threshold effects. During this fit an additional systematic error ($\sim$5%) associated with the judgment of the fit boundaries, was assumed. The fit parameters with χ^2/degree of freedom = 1.151 are presented in table 3.2. The root mean square statistical errors are the square roots of the diagonal elements of the covariance matrix. The covariance matrix for this fit is given in (3.13)

$$\begin{vmatrix} \sigma_A^2 & \sigma_A\sigma_B & \sigma_A\sigma_C \\ \sigma_B\sigma_A & \sigma_B^2 & \sigma_B\sigma_C \\ \sigma_C\sigma_A & \sigma_C\sigma_B & \sigma_C^2 \end{vmatrix} = \begin{vmatrix} 0.29286 & -0.05545 & 0.34847 \\ -0.05545 & 0.01074 & -0.06460 \\ 0.34847 & -0.06460 & 0.42612 \end{vmatrix} \tag{3.13}$$

The results of the fit are graphically presented in Figure 3.14. The relatively large errors for the ^{88}Y measured efficiencies are explained by the large uncertainty (+30%,

Table 3.2: Efficiency for an isotropic source fit to equation 3.12.

Parameter	Value	Root Mean Square Statistical Error of Estimate	Root Mean Square Total Error of Estimate (Standard Error)
A	-3.4055	0.54117	0.58071
B	1.3712	0.10365	0.11122
C	-4.0446	0.65278	0.70047

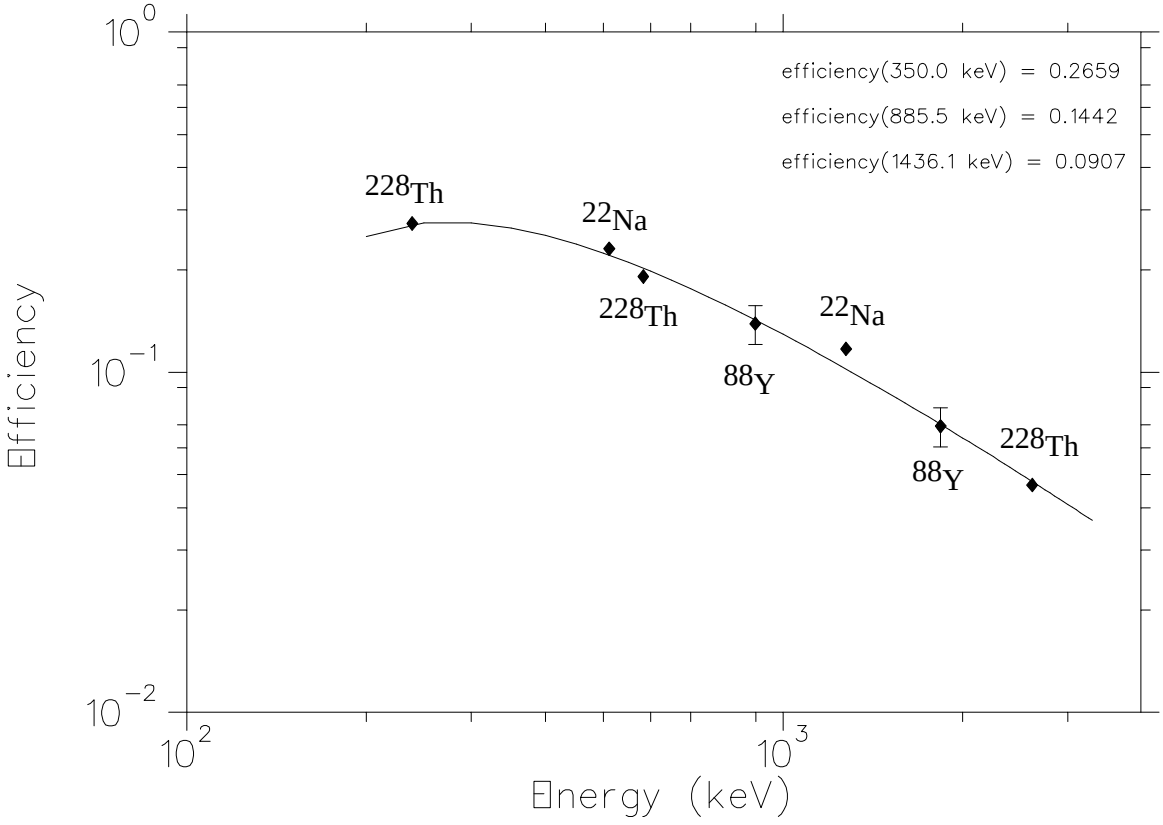

Figure 3.14: The NSCL NaI(Tl) array efficiency. The efficiency for isotropic angular distribution was measured with ^{228}Th, ^{22}Na and ^{88}Y γ-sources located at the target position.

-0%) of the radioactive source intensity.

The efficiency error is defined by the error propagation equation [60]

$$\sigma_\epsilon^2 \simeq \sigma_A^2\left(\frac{\partial\epsilon}{\partial A}\right)^2 + \sigma_B^2\left(\frac{\partial\epsilon}{\partial B}\right)^2 + ... + 2\sigma_A\sigma_B\left(\frac{\partial\epsilon}{\partial A}\right)\left(\frac{\partial\epsilon}{\partial B}\right) + ..., \tag{3.14}$$

where σ_A^2, σ_B^2, $\sigma_A\sigma_B$ are diagonal and off-diagonal covariance matrix elements and $\frac{\partial\epsilon}{\partial A}$, $\frac{\partial\epsilon}{\partial B}$ are partial derivatives of the efficiency function 3.12.

3.4.2 Efficiency for De-excitation Photons

It was found in section 2.3 that the angular distribution of γ-rays in Coulomb excitation ($W(\theta)$) is nonisotropic. Therefore, such angular distributions can lead to over/underestimations of the detection efficiency. A detailed discussion of this problem is presented in [39], here I will present a short summary.

The total efficiency can be obtained by folding the detector efficiency $\epsilon(E_\gamma, \theta, \phi)$ with the calculated angular distribution $W(\theta)$ as follows

$$\epsilon_{\rm tot}(E_\gamma) = \frac{\int\limits_{\Omega} W(\theta)\cdot\epsilon(E_\gamma,\theta,\phi)\,d\Omega}{\int\limits_{4\pi} W(\theta)\,d\Omega}\,. \tag{3.15}$$

The angular distribution of the γ rays integrated over all space is normalized to unity

$$\int\limits_{4\pi} W(\Omega)\,d\Omega = 1. \tag{3.16}$$

Thus, if one assumes the efficiency to be constant over the range of Ω_i

$$\begin{aligned}
\epsilon_{\rm tot}(E_\gamma) &= \int\limits_{\Omega} W(\theta)\,\epsilon(E_\gamma,\theta,\phi)\,d\Omega \\
&= \sum_i \int\limits_{\Omega_i} W(\theta)\,\epsilon(E_\gamma,\theta,\phi)\,d\Omega \\
&= \sum_i \epsilon(E_\gamma,\theta_i,\phi_i)\int\limits_{\Omega_i} W(\theta)\,d\Omega\,.
\end{aligned}$$

The efficiency $\epsilon(E_\gamma, \theta_i, \phi_i)$ is related to the efficiency for an isotropic source in equation 3.11 through

$$\epsilon(\Omega) = \frac{4\pi}{\Omega}\epsilon_\Omega^{(\mathrm{iso})} \,. \tag{3.17}$$

Therefore, the total photopeak efficiency can be expressed in terms of the measured isotropic efficiency and the calculated angular distribution as follows:

$$\epsilon_{\mathrm{tot}} = \sum_i \frac{4\pi}{\Omega_i}\epsilon^{(\mathrm{iso})}(E_\gamma) \int_{\Omega_i} W(\theta)\, d\Omega \,, \tag{3.18}$$

where $\epsilon^{(\mathrm{iso})}(E_\gamma, \theta_i, \phi_i)$ is obtained from the efficiency calibration and $W(\theta)$ is defined by equation 2.31.

Besides an efficiency correction for a particular experimental angular distribution, the efficiency calculation code presented in Appendix C.3 also calculates an efficiency correction for photon absorption in the target, which is discussed in section 3.4.3.

3.4.3 Photons Absorption in the Target

Absorption of photons in the secondary target modifies the efficiency in the Coulomb excitation experiments from the efficiency for an isotropic source. This modification is especially crucial for low-energy photons and thick targets, such as the $E_\gamma = 350(20)$ keV photons emitted by ^{31}Na in the 702 mg/cm^2 ^{197}Au target. The present method closely follows the description found in [61, 62] and assumes that the life time for an excited state is less than 10^{-12} sec, i.e. the photon is emitted in the target.

The decrease in intensity of a parallel beam of photons passing through an absorber of thickness d is given by [61]

$$I = I_0 \cdot 2^{\frac{-d}{d_{1/2}}} \,, \tag{3.19}$$

where I_0 and I are the beam intensities before and after passing through the target. $d_{1/2}$ is an absorber half-thickness. For a monoisotopic absorbing material (such as the gold target) the quantity $d_{1/2}$ can be expressed in terms of the photon energy E_γ

Table 3.3: Fit parameters for equation 3.21 for the absorption cross section of photons in gold.

Parameter	Value	Root Mean Square Statistical Error of Estimate	Root Mean Square Total Error of Estimate (Standard Error)
$A1$	7.6767	0.29609	0.08605
$A2$	76.891	23.916	6.9503
$A3$	344.10	49.868	14.492
$A4$	1763.8	533.73	155.11
$A5$	79.207	10.083	2.9301

and properties of the material

$$d_{1/2} = \frac{A \cdot \log 2}{N_A \cdot \rho \cdot \sigma(E_\gamma)}\,, \tag{3.20}$$

where N_A is Avogadro's number, ρ is the density of the absorbing material and $\sigma(E_\gamma)$ is an atomic cross section. The atomic cross section includes contributions from the coherent (Rayleigh) and incoherent (Compton) scattering, photoelectric effect and positron-electron pair production [53, 55, 63].

To estimate the efficiency corrections for a gold target the total absorption cross sections [63] were fitted with a second order exponential

$$\sigma(E_\gamma) = A1 + A2 \cdot \exp(-E_\gamma/A3) + A4 \cdot \exp(-E_\gamma/A5)\,, \tag{3.21}$$

where E_γ is the energy of the emitted photon. $A1$, $A2$, $A3$, $A4$ and $A5$ are fit parameters, which are presented in table 3.3 and $\sigma(E_\gamma)$ is expressed in mb. Figure 3.15 graphically represents this fit (with a total χ^2/degree of freedom = 0.0845 and a confidence level of 99.47 %). The fit results were folded with the photons angular

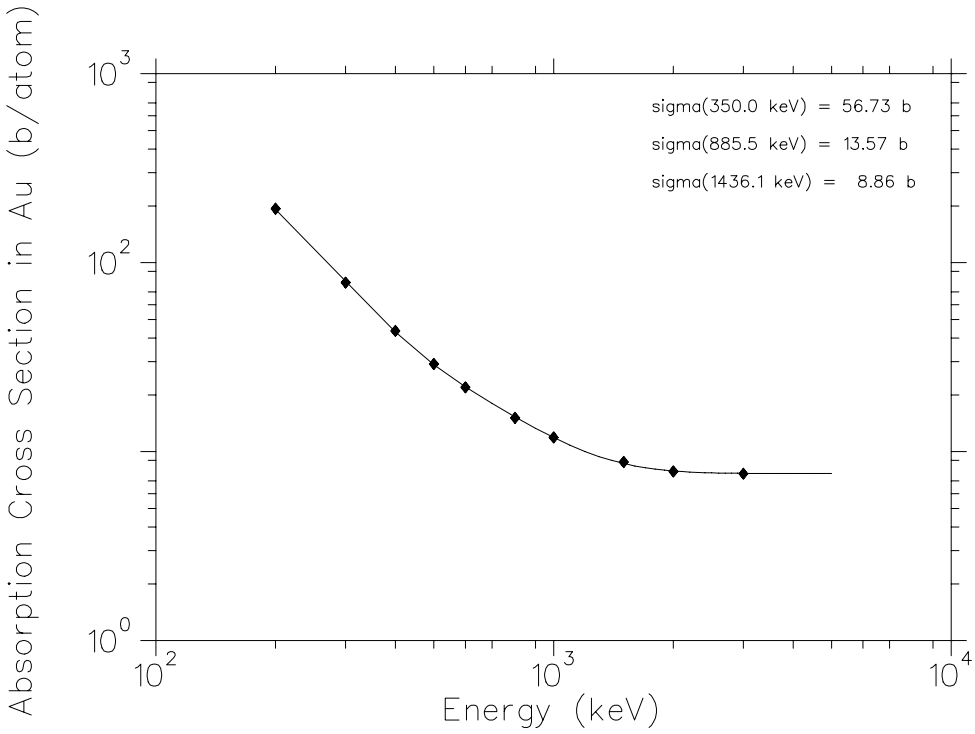

Figure 3.15: Absorption cross sections in gold versus photon energy.

distribution of photons and used for efficiency calculations.

The reliability of this procedure was tested with a ^{36}Ar test beam and a ^{197}Au target, which will be discussed in section 4.2. During this test the known Coulomb excitation cross sections were reproduced with good accuracy.

3.5 Data Analysis

This section describes the principles of data analysis for the NSCL NaI(Tl) array. The accuracy of the present analysis procedure is discussed and limitations are given.

3.5.1 Experimental Gates and Particle Groups

The sensitivity of the experiment depends on the separation of Coulomb excitation events from the radioactive background. To select events originating from the projectile and target de-excitations, only NaI(Tl)-detector signals which coincided within

$\sim$200 nsec with signals from the phoswich detector were recorded. This group of events is called particle-γ coincidences. Figure 3.4 demonstrates the projectile identification in this experiment. It is easy to see that good particle identification is necessary for experiments with cocktail beams.

3.5.2 Calculation of Incoming Flux

The total number of incoming beam particles (particle-singles) needs to be known for a cross section calculation. This number of particle-singles is usually recorded with a down-scale (d/s) factor (a d/s factor of 100 indicates that only one out of 100 events in the phoswich detector was recorded), which allows an increased live time of the data acquisition system [3] .

Figure 3.8 demonstrates that phoswich-detector signals are processed by Quad four-fold-unit which generates trigger bits. Bits spectrum (particle-γ, particle-singles) signals with a gate on the isotope of interest is plotted in Figure 3.16.

The total number of incoming nuclei is equal to the number of down-scaled particle-singles events multiplied by the down-scale factor, which usually varies from 30 to 500. The total number of counts under the particle-γ peak on the plot provides the total number of particle-γ coincidences. Particle-γ coincidences can be created by photons from de-excitations in the target and the phoswich detector. Further background rejection is achieved by applying a time cut (which will be discussed in subsection 3.5.3), effectively reducing the coincidence window from 200 nsec to a few nsec.

The down-scaled incoming beam flux can be calculated by applying particle-singles gate to a particle ID spectrum (see for example Figure 3.4). The number of counts

[3]The recorded number of incoming particles is affected by the live time of the data acquisition system. However, for cross section calculation (see equation 2.34) this correction is not necessary because the number of detected de-excitation photons N_γ is identically affected.

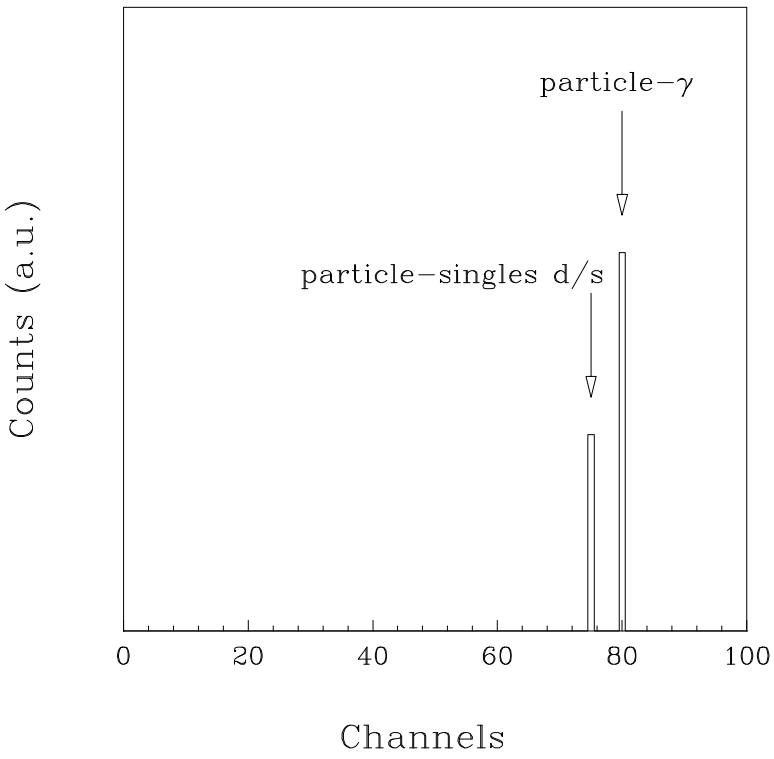

Figure 3.16: Bits Spectrum. The particle-singles and particle-γ events are defined as single-channel histograms.

in this gate multiplied by the down-scale factor is also equal to the total number of incoming nuclei of this particular isotope.

3.5.3 Time Cut

In the current experiments the average target/first-ring detector and target/phoswich distances (see Figure 3.5) were ∼10 cm and ∼1 m, respectively. For a typical projectile velocity of ($v_p \sim 0.3c$) these distances define times of flight for photons emitted from the target area (∼0.3 nsec) and the zero-degree detector (∼13 nsec). This separates target/projectile de-excitations from de-excitations in the ZDD by ∼10-15 nsec. To prevent accidental coincidences, the time difference between the detection of the photon in the NaI(Tl) detectors and the detection of the scattered fragment in the ZDD was recorded for each event. During the data analysis theses two classes of data can be separated as shown in Figure 3.17.

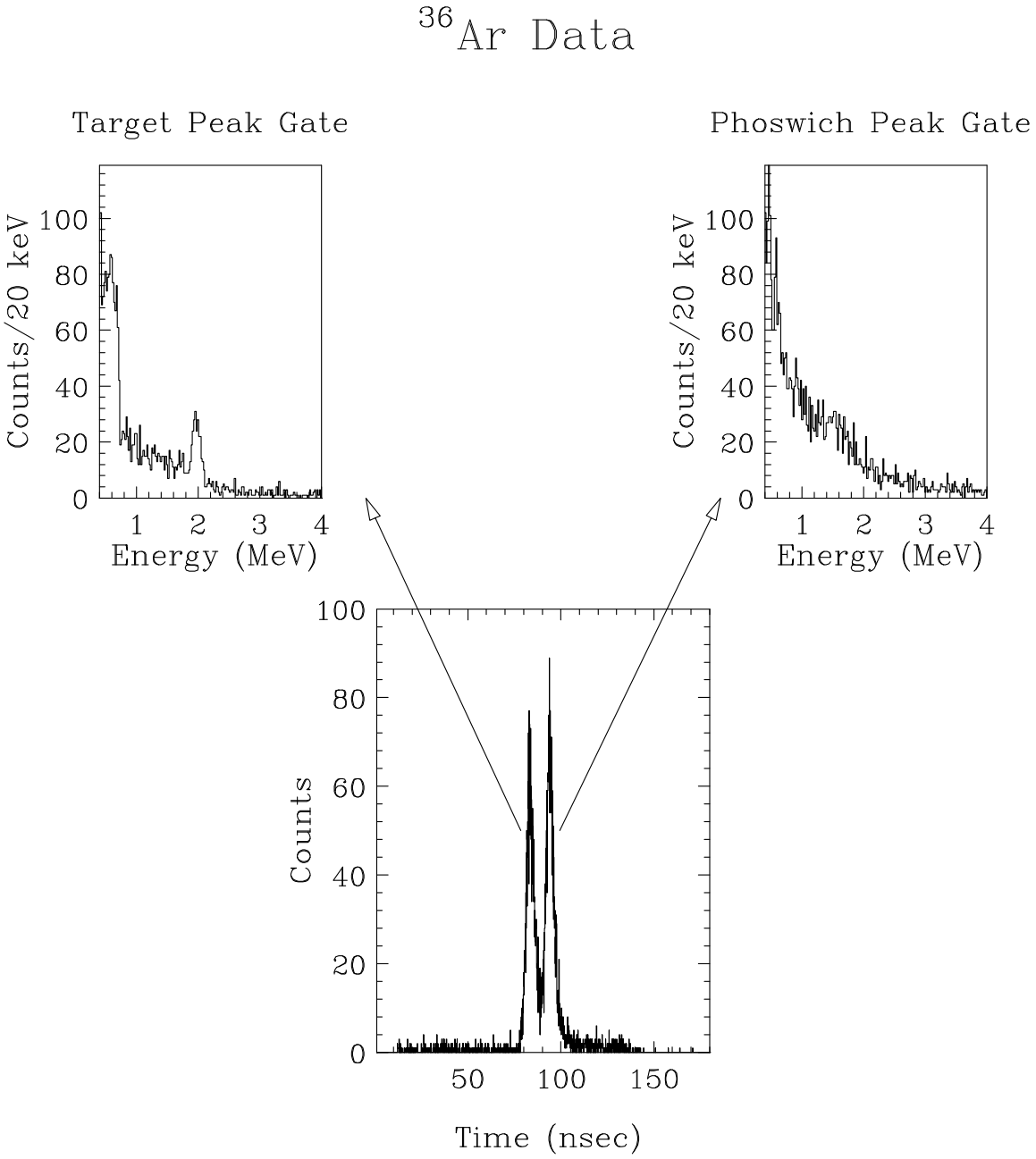

Figure 3.17: The time spectrum contains two peaks, the peak on the left is created by photons from the target or projectile de-excitations in the target and the peak on the right is due to de-excitations in the phoswich detector.

3.5.4 Photon Multiplicity

The photon multiplicity is the number of photons emitted in each event. In intermediate-energy scattering, many different reactions such as Coulomb and nuclear excitations, neutron removal and nuclear fragmentation take place. Coulomb excitation creates a few photons due to de-excitation while other nuclear reactions such as projectile fragmentation produce many γ-rays. Coulomb de-excitation events can be enhanced by selecting events with low multiplicities.

The impact of different multiplicity gates on the ^{32}Mg γ-data is shown in Figure 3.18. The figure indicates that, for large multiplicity events the γ-background increases and the 885 keV transition in ^{32}Mg becomes less pronounced.

3.5.5 Experimental Errors

The three major sources of errors in the experimental data are

- A statistical error associated with the number of detected photons.
- The efficiency error, which is 3.5-4.5 % in the 0.3-2.0 MeV energy range.
- A phoswich detector position uncertainty, which creates an uncertainty in the scattering angle of $\theta_{lab}^{max} \approx 0.1^{\circ}$.

Contributions from other errors such as uncertainties in beam velocity, transition energies, and cross sections for absorption in the target are much smaller. The errors, considered here, are independent and the total error is equal to the square root of the sum of quadratures [60].

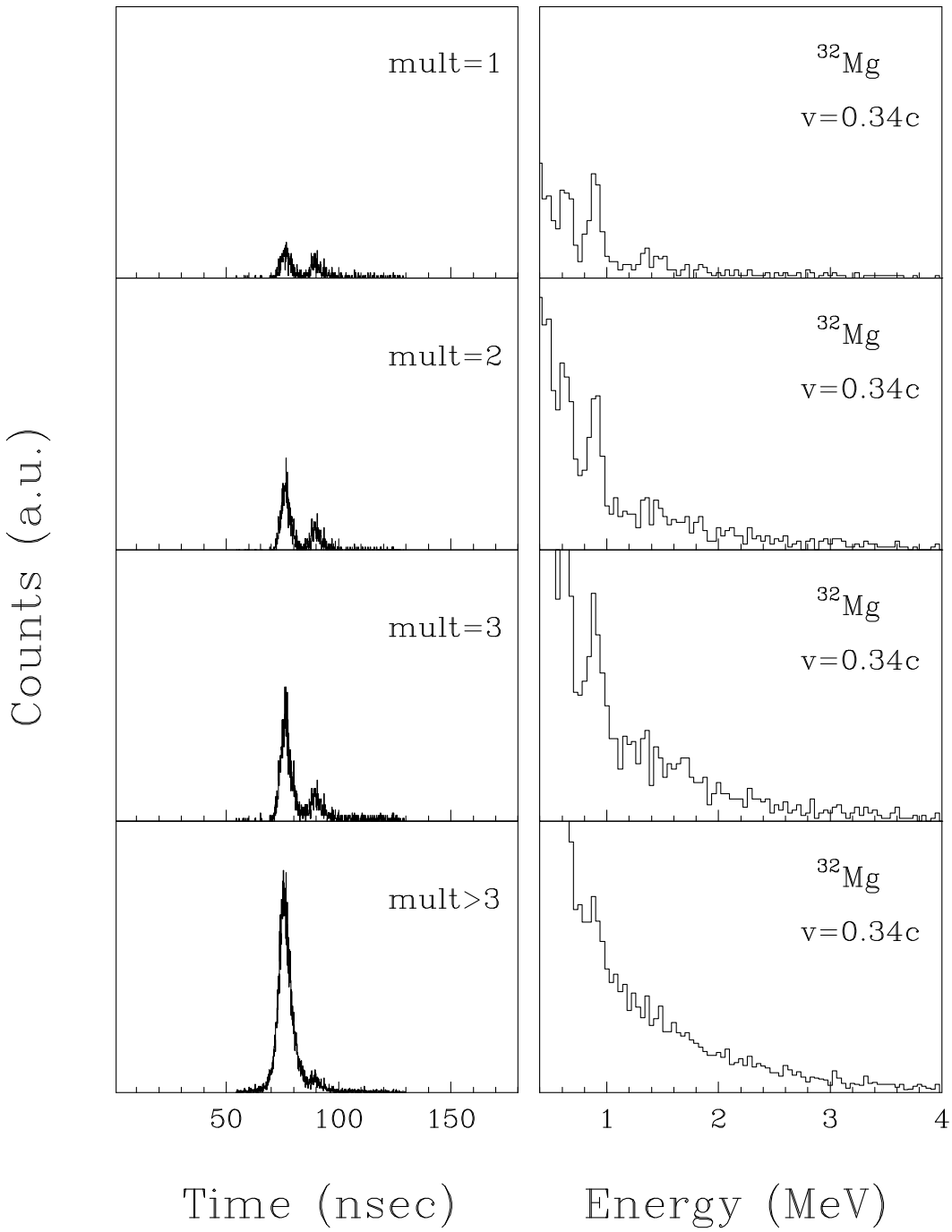

Figure 3.18: ^{32}Mg data as a function of multiplicity. The left panels contain time spectra and the right panels show the corresponding γ-spectra for different multiplicities gated on the ^{32}Mg particle group. The nuclear fragmentation events (large multiplicity) produce many photons in the target area and increase the γ-background in the ^{32}Mg data.

Chapter 4

Experimental Results

The present chapter is dedicated to the description of experimental results. The experimental data for even-even and odd nuclei were analyzed using the method discussed in section 3.5 and interpreted on the basis of nuclear models which were described in chapter 1. Possible physical explanations of the experimental results are discussed and conclusions are given.

4.1 Primary and Secondary Beams

Primary beams of $^{48}Ca^{13+}$ with an energy of 80 MeV/nucleon and intensity as high as 8 particle-nA[1] and $^{40}Ar^{12+}$ having energy of 90 MeV/nucleon and intensity of 80 particle-nA were produced with the NSCL superconducting electron cyclotron resonance ion source and the K1200 superconducting cyclotron.

Table 4.1 presents the secondary beams of ^{26,28}Ne, $^{28-31}$Na, $^{30-34}$Mg and ^{34,35}Al, ^{33}Si and ^{34}P which were made via fragmentation of the calcium or argon primary beams in a ^{9}Be primary target located at the mid-acceptance target position of the A1200 fragment separator [47] and delivered onto a ^{197}Au secondary target located

[1] 1 particle-nA $= 10^{-9} \cdot \frac{1}{1.6 \cdot 10^{-19}} \frac{\text{particles}}{s} \approx 6.2 \cdot 10^{9} \frac{\text{particles}}{s}$

in the middle of the NSCL NaI(Tl) array. Typical beam rates for the particles of interest ranged between one and a few hundred particles per second. Substantial amounts of ^{21,22}O, $^{22-25}$F, ^{24,25,27}Ne, ^{26,27}Na, ^{29}Mg, $^{30-33,36,37}$Al, ^{32,36,37}Si and ^{40,41}P were also produced in the present experiments, however electromagnetic transitions between band states in these isotopes were not observed in the range of 200 keV $< E_\gamma <$ 4 MeV.

All nuclei described here were subjected to the same data analysis procedure, nevertheless the data interpretation was different. From the nuclear properties of even-even nuclei [33] one can predict 0^+ and 2^+ spin and parity assignment for the ground and first excited state, respectively. Such spin and parity assignments indicate E2 electromagnetic transitions (see equations 2.28, 2.29). Odd isotopes provide a challenge for data interpretation, because spin and parity assignments for the ground and first excited states are often unknown and electromagnetic transitions are not uniquely defined (different transitions such as $E1$, $E2$, $M1$ and $M2$ are allowed). Therefore additional theoretical and experimental considerations provide an avenue for the odd-nuclei data interpretation.

4.2 ^{36}Ar Test Beam

The data analysis procedure was checked for two known nuclei: a ^{36}Ar beam and the ^{197}Au target.

Figure 4.1 contains results for the ^{36}Ar test beam. ^{36}Ar was selected for calibrations because of the well-established adopted value of reduced transition probability for the first excited state of $B(E2; 0^+_{g.s.} \rightarrow 2^+) = 298(30)$ e^{2}fm^4 [64]. This value is in excellent agreement with the present experimental result of $B(E2; 0^+_{g.s.} \rightarrow 2^+) = 286(23)$ e^{2}fm^4. Besides, results of the current measurement are also in agreement with the results from inelastic electron scattering: $B(E2; 0^+_{g.s.} \rightarrow 2^+) = 280(16)$ e^{2}fm^4

Table 4.1: Beam parameters for the isotopes with observed γ-transitions.

Primary beam	^{9}Be target (mg/cm^2)	Secondary beam	Total beam particles/10^6	^{197}Au target (mg/cm^2)	θ_{lab}^{max} (deg)
^{48}Ca	376	^{28}Ne	1.46	702	2.8
		^{29}Na	12.96		
		^{30}Na	3.30		
		^{31}Na	1.28		
		^{31}Mg	8.0		
		^{32}Mg	13.0		
		^{33}Mg	1.70		
		^{34}Mg	0.22		
		^{34}Al	5.52		
		^{35}Al	5.35		
^{40}Ar	564	^{26}Ne	39.83	518	3.96
		^{28}Na	82.44		
		^{30}Mg	98.35		
		^{33}Si	1020.4		
		^{34}P	106.34		

[65].

Target excitations in ^{197}Au with the ^{36}Ar beam were used to find the excitation cross section in ^{197}Au. Data analysis of the target excitations was based on the fact that scattering angle in the c.m. system between projectile and target nuclei is exactly the same as between target and projectile nuclei and the beam velocity is known. For this case, Z and A for target and projectile nuclei were interchanged in the MATHEMATICA reduced transition probability calculation routine, given in Appendix A. The present experimental value for ^{197}Au of $B(E2; 3/2^+_{g.s.} \rightarrow 7/2^+) =$ 4899(351) e^{2}fm^4 agrees with the adopted value of $B(E2; 3/2^+_{g.s.} \rightarrow 7/2^+) = 4988(170)$ e^{2}fm^4 [66].

4.3 Even-Even Isotopes of ^{26,28}Ne and ^{30,32,34}Mg

The following is a presentation of the Coulomb excitation results for ^{26,28}Ne and ^{30,32,34}Mg. The data are discussed using the single-particle approach (presented in section 1.2). These results have been published in Physics Letters B [17].

4.3.1 Experimental Results

The γ-ray spectra, both without the Doppler correction (laboratory frame) and with the Doppler correction (projectile frame) for ^{26,28}Ne and ^{30,32,34}Mg are shown in Figure 4.1. The laboratory frame and projectile frame spectra from the test measurement of the stable nucleus ^{36}Ar are also included. Photons de-exciting the previously observed 2^+_1 states in ^{30}Mg and ^{32}Mg (at 1482 and 885 keV, respectively) are apparent in the projectile-frame spectra for those two nuclei. A strong peak occurs in the projectile-frame spectrum for ^{26}Ne at 1990(12) keV, while a somewhat weaker (though still clear) peak appears in the corresponding ^{28}Ne spectrum at 1320(20) keV. On the basis of these observations, we propose that the 2^+_1 states occur at these energies

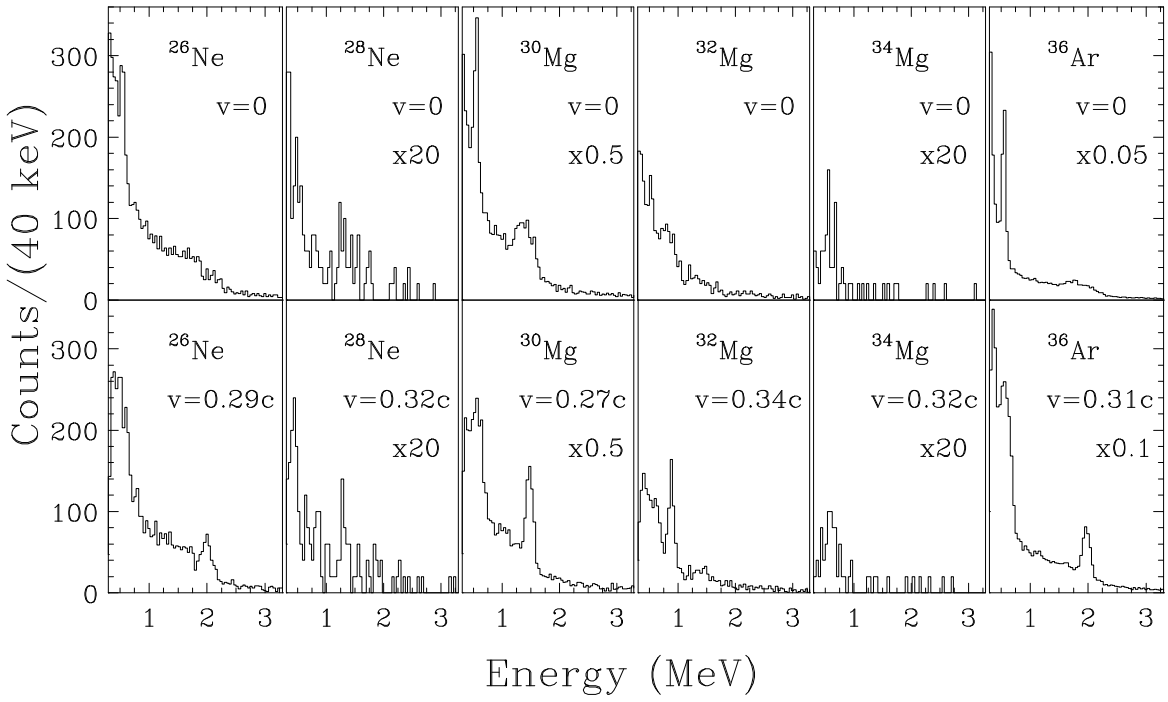

Figure 4.1: Experimental results for even-even isotopes. The upper panels show photon spectra in the laboratory frame. The 547 keV ($7/2^+ \rightarrow g.s.$) transition in the gold target is visible as a peak, while the ($2^+ \rightarrow g.s.$) transitions in each projectile are very broad. The lower panels show Doppler-shifted γ-ray spectra. The $2^+ \rightarrow g.s.$ transitions in each projectile sharpens.

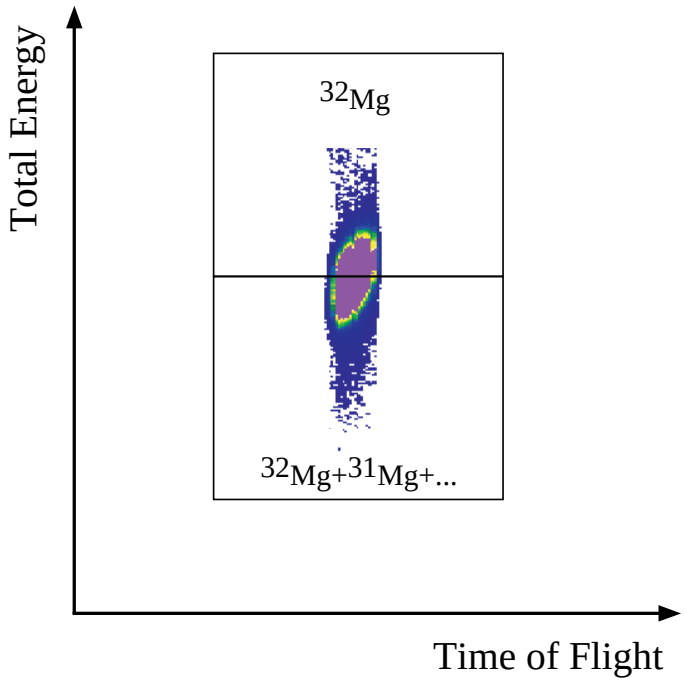

Figure 4.2: ^{32}Mg gates. The upper gate contains ^{32}Mg beam and the lower gate has a possible admixture of neutron-stripping events (^{32}Mg + ^{31}Mg + ...).

in ^{26,28}Ne. The results on the 2_1^+ state energies in the neon isotopes are consistent with those reported at a recent conference [67, 68]. Only a few counts appear in the ^{34}Mg spectrum above a Doppler-shifted energy of 800 keV. Below this energy, there is background due to the Coulomb excitation of the gold target.

It is useful to analyze the Doppler-shifted spectrum of ^{32}Mg in more detail. Along with the peak from the $2^+ \rightarrow 0^+_{g.s.}$ transition another broad peak around 1.45 MeV is visible. From previous experience, we assume that radioactive background in this region is due to stripping of neutrons and subsequent de-excitations of ^{31}Mg or ^{30}Mg. If this assumption is true, then such stripping events can be distinguished because the total energy of ^{31}Mg or ^{30}Mg ions is smaller than total energy of ^{32}Mg. To test this, all ^{32}Mg events were separated into two groups: the higher (^{32}Mg) and the lower than average total energy (^{32}Mg + ^{31}Mg + ...) events (see Figure 4.2). The corresponding γ-ray spectra are shown in Figure 4.3.

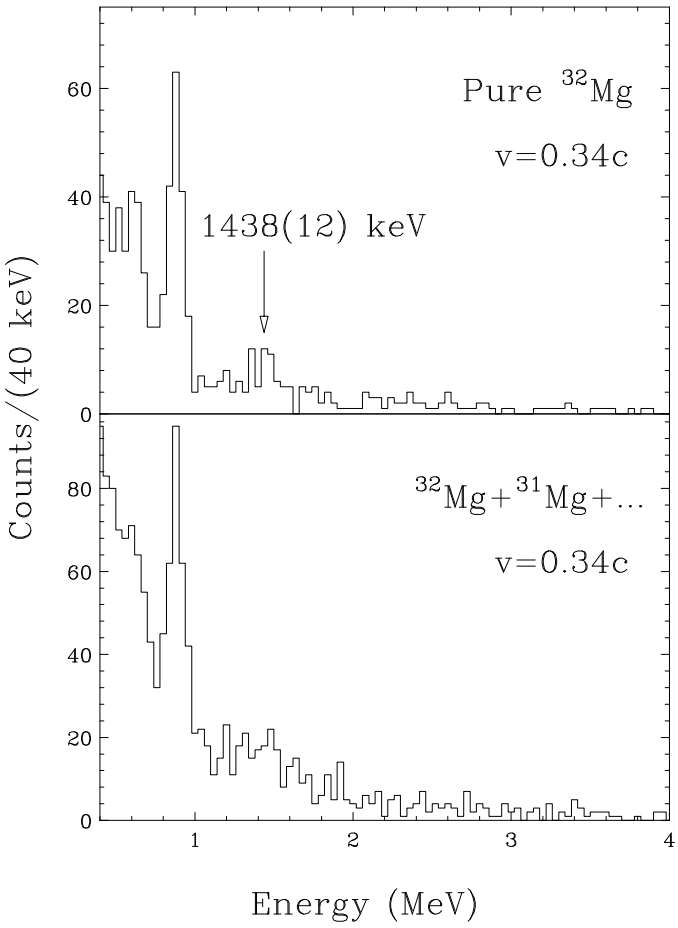

Figure 4.3: ^{32}Mg data with total energy gates. Doppler-shifted γ-ray spectra for ^{32}Mg and ^{32}Mg + ^{31}Mg + ...

The important feature in the ^{32}Mg beam γ-spectrum (top part of Figure 4.3) is a small peak at 1438(12) keV, an energy which agrees with a γ-ray observed at 1436(1) keV in the β-decay of ^{32}Na [13, 14, 15]. Klotz *et al.* [15] determined that the 1436 keV γ-ray is in coincidence with the 885 keV $2_1^+ \rightarrow 0_{gs}^+$ γ-ray and, therefore, it de-excites a state at 2321 keV.

For ^{26,28}Ne and ^{30}Mg, where the 2_1^+ states do not appear to be fed by higher-lying states, the cross sections for populating the 2_1^+ states can be determined by using equation 2.34. Results are listed in Table 4.2. The population cross sections for the 2_1^+ states of these nuclei can then be used to obtain $B(E2; 0_{gs}^+ \rightarrow 2_1^+)$ values using the formalism of Winther and Alder [35] (see equation 2.23), and these reduced matrix

Table 4.2: Experimental parameters and results for even-even nuclei.

Nucleus	$E_{beam}^{midtarget}$ (MeV/A)	$E(2_1^+)$ (keV)	σ (mb)	θ_{cm}^{max} (deg)	$B(E2; 0_{g.s.}^+ \rightarrow 2^+)$ (e^2fm^4)
^{26}Ne	41.7	1990(12)	74(13)	4.48	228(41)
^{28}Ne	53.0	1320(20)	68(34)	3.20	269(136)
^{30}Mg	36.5	1481(3)	78(7)	4.56	295(26)
^{32}Mg	57.8	885(9)	80(17)	3.25	333(70)
^{34}Mg	50.6		≤ 164	3.28	≤ 670

elements are also listed in Table 4.2.

In the case of ^{32}Mg, the 2_1^+ state is not only populated directly in the intermediate energy Coulomb excitation reaction but is also fed via the 1436 keV γ-ray decay from the 2321 keV state. Therefore, the population cross section for the 2_1^+ state is the difference between the production cross sections for the 885 and 1436 keV γ-rays. Since the 885 keV transition has $E2$ ($2_1^+ \rightarrow 0_{gs}^+$) character [14], the production cross section for this state can be unambiguously determined from the experimental yield to be 107(13) mb. However, there is some uncertainty about the cross section for production of the 1436 keV γ-ray because the efficiency for detection of a γ-ray depends on its angular distribution, which in turn depends on the multipolarity of the transition and the spins of the initial and final states. We do not know the spin and parity of the 2321 keV state. However, a coupled-channels Coulomb excitation calculations RELEX [69] allows us to exclude the possibility of a two-step excitation of the 2321 keV state via 885 keV and 1436 keV transitions and only direct excitation of the 2321 keV state can occur. The possible J^π values for this state are limited to 1^- and 2^+ by requiring that the reduced matrix elements $B(\lambda; 0_{gs}^+ \rightarrow \lambda^\pi)$ corresponding

Table 4.3: Possible excitations of the 2321 keV state in ^{32}Mg.

Transition ($E\lambda$)	Energy (keV)	σ(1436 keV) (mb)	$B(E\lambda)$ (e^{2}fm$^{2\lambda}$)
$E1; 0^+ \rightarrow 1^-$	2321	28(11)	0.040(16)
$E2; 0^+ \rightarrow 2^+$	2321	26(10)	105(42)

to the observed experimental yield for the 2321 keV state are less than or equal to the recommended upper limits listed by Endt [70, 71]. Table 4.3 contains possible reduced transition probabilities of the 2321 keV state assuming one-step excitation (2321 keV) and two-step de-excitation (1436 and 885 keV) processes.

The results in Table 4.3 indicate that the value of the de-excitation cross section for production of the 1436 keV γ-ray (feeding cross section) is only slightly affected by the multipolarity of the transition. Consequently, the $2^+, 1^- \rightarrow 2^+$ cross section is consistent with 26(10) mb. When the feeding cross section is subtracted from the γ-ray production cross section for the 885 keV γ-ray, we obtain a cross section of 80(13) mb for direct population of the 2_1^+ state, which then yields $B(E2; 0_{gs}^+ \rightarrow 2_1^+) = 333(70)$ e^{2}fm^4 for ^{32}Mg. This value is 27% lower than the value reported by Motobayashi *et al.* [16].

Motobayashi *et al.* did not report the observation of the 1436 keV γ-ray. However, it is worth noting that the difference between the $B(E2; 0_{gs}^+ \rightarrow 2_1^+)$ values obtained in Ref. [16] and the present work can be accounted for by the feeding correction applied here. Without the feeding correction, we would have obtained $B(E2; 0_{gs}^+ \rightarrow 2_1^+) = 440(55)$ e^{2}fm^4, which would be consistent with the result from Ref. [16] of $B(E2; 0_{gs}^+ \rightarrow 2_1^+) = 454(78)$ e^{2}fm^4.

The secondary ^{34}Mg beam was particularly weak, and the integrated number of

beam particles was small. However, we can still draw some conclusions from the γ-ray spectrum. The Doppler shifted spectrum for ^{34}Mg contains a significant background below 800 keV which results in part from γ-rays from the gold target. There are also several counts in the spectrum above 800 keV. The data are not sufficient to identify the energy of the 2_1^+ state. However, if we assume the 2_1^+ state is located between 0.9 and 1.4 MeV, we can place an upper limit of 670 e^{2}fm^4 on $B(E2; 0_{gs}^+ \rightarrow 2_1^+)$.

The systematic behavior of transition energies and reduced transition probabilities of even-even isotopes in the island of inversion region is presented in Figure 4.4. The small transition energy and large $B(E2)$ value in ^{32}Mg clearly indicate that this nucleus is dominated by intruder configurations. *sd*-shell model calculations [73] predict a large transition energy $E_\gamma = 1.677$ MeV and a smaller degree of collectivity of $B(E2\uparrow) = 172$ e^{2}fm^4.

4.3.2 Quadrupole Moments Calculation

While the spherical shell model has been used extensively to study nuclei in the vicinity of the island of inversion, the deformed shell model, or Nilsson model, provides another framework for gaining insights about isotopes in this region. If we assume that the nuclei studied here have static quadrupole deformations with axial symmetry, we can use the Nilsson model [29] to calculate intrinsic quadrupole moments for oblate and prolate shapes to see whether the data provide a preference for one shape over the other. The Nilsson diagram used for the present calculations (generated with $v_{ls} = -0.16$ and $v_{ll} = 0$, $v_{ls} = -0.127$ and $v_{ll} = -0.0382$ parameters used in the single-particle potential [30] for the *sd* and *pf* shells, respectively) is shown in Figure 1.2. The deformation parameter used in the diagram is δ, which is related to the usual spherical harmonic coefficient β_{20} (or just β_2) by equation $\beta_2 \approx \delta/0.95$ [30]. With this Nilsson model, the intrinsic electric quadrupole moments Q_0 have been recently

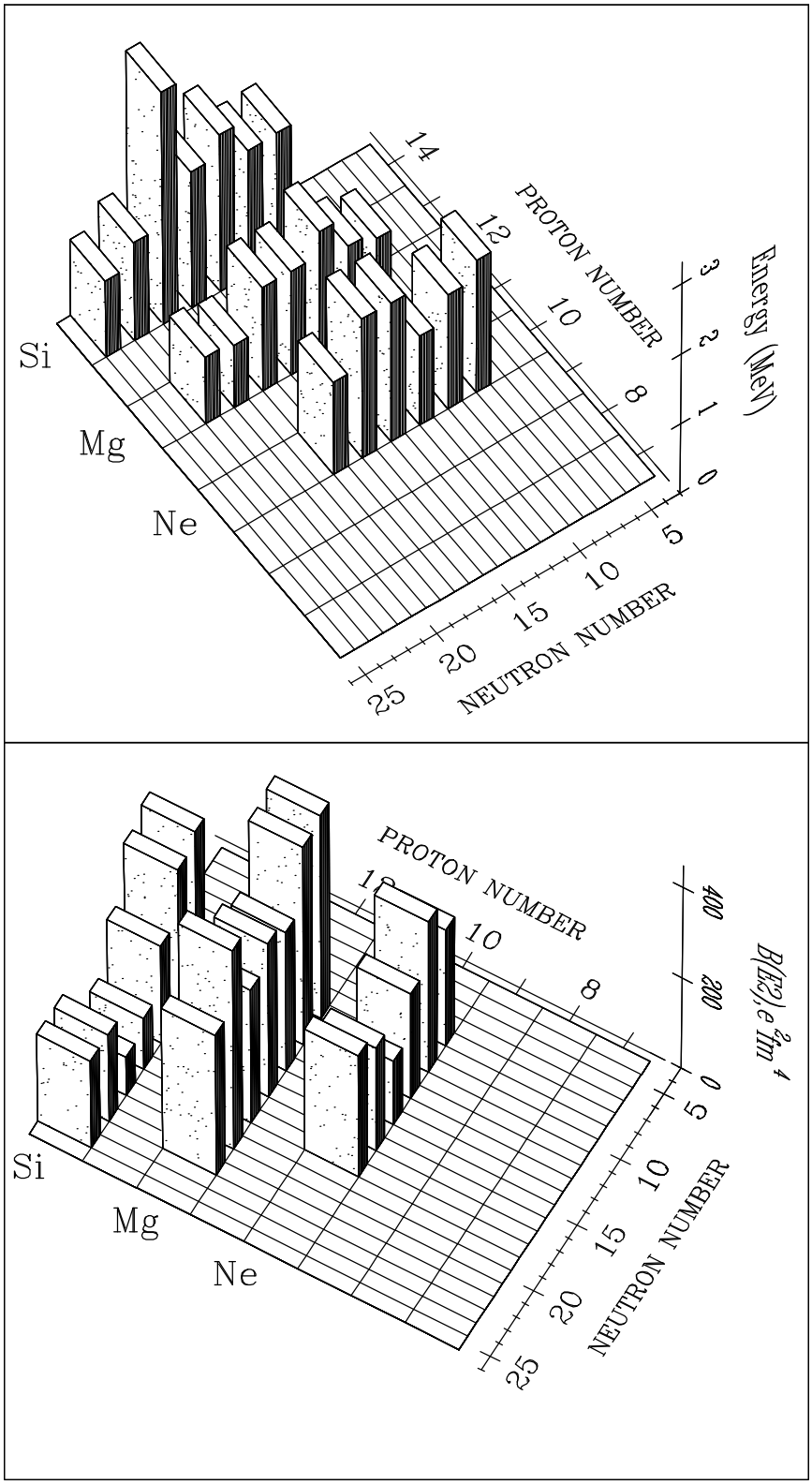

Figure 4.4: Systematic behavior of transition energies and reduced transition probabilities for the known even-even isotopes of Ne, Mg and Si. Data is taken from [17, 33, 76].

calculated in Ref. [17] for the nuclei studied here over a range of deformations by summing over the contributions of the individual protons

$$Q_0 = (16\pi/5)^{1/2} \sum_{\lambda} \langle \lambda | r^2 Y_{20} | \lambda \rangle \,, \tag{4.1}$$

where λ are the occupied proton orbitals. The intrinsic quadrupole moments are graphed as a function of δ for ^{26,28}Ne and ^{30,32,34}Mg in Figure 4.5. The figures do not include quadrupole moment results for the range of small δ values ($-0.1 < \delta < 0.1$) where the residual interaction outside of the standard Nilsson model becomes important. This figure also illustrates the "experimental" intrinsic electric quadrupole moments extracted from the measured $B(E2; 0^+_{gs} \rightarrow 2^+_1)$ values via the equation [30]

$$Q_0^2 = (\frac{16\pi}{5}) B(E2; 0^+_{gs} \rightarrow 2^+_1) \,. \tag{4.2}$$

The bands shown in Figure 4.5 as dashed lines correspond to the ranges of experimental uncertainty in the present work. Both positive and negative experimental values are shown in the graphs because our experiment cannot discriminate between prolate and oblate shapes. For all the nuclei in Figure 4.5, it is clear that the "experimental" quadrupole moments can be reproduced if the nuclei have substantial prolate deformations ($\delta \geq 0.3$). However, the quadrupole moments for all oblate deformation parameters shown have magnitudes which are much larger than the experimental values. We conclude that if these nuclei have static axially symmetric deformations, they must be prolate. The present conclusion that ^{32}Mg is prolate is consistent with the results of Refs. [5, 18] in which the spherical shell model is used.

These results provide a more complete picture of the extent of the island of inversion and the role of the intruder states outside the boundaries of the island of inversion. It is clear that the energies and $B(E2; 0^+_{gs} \rightarrow 2^+)$ values for the lowest 2^+ states in the $N = 16$ isotope ^{26}Ne and the $N = 18$ isotope ^{30}Mg can be explained using the normal $0\,\hbar\omega$ configurations[2] , while the energy of the 2^+_1 state in ^{28}Ne

[2]Normal ($0\,\hbar\omega$) configuration denotes the *sd*-shell while the intruder ($2\,\hbar\omega$) configuration has

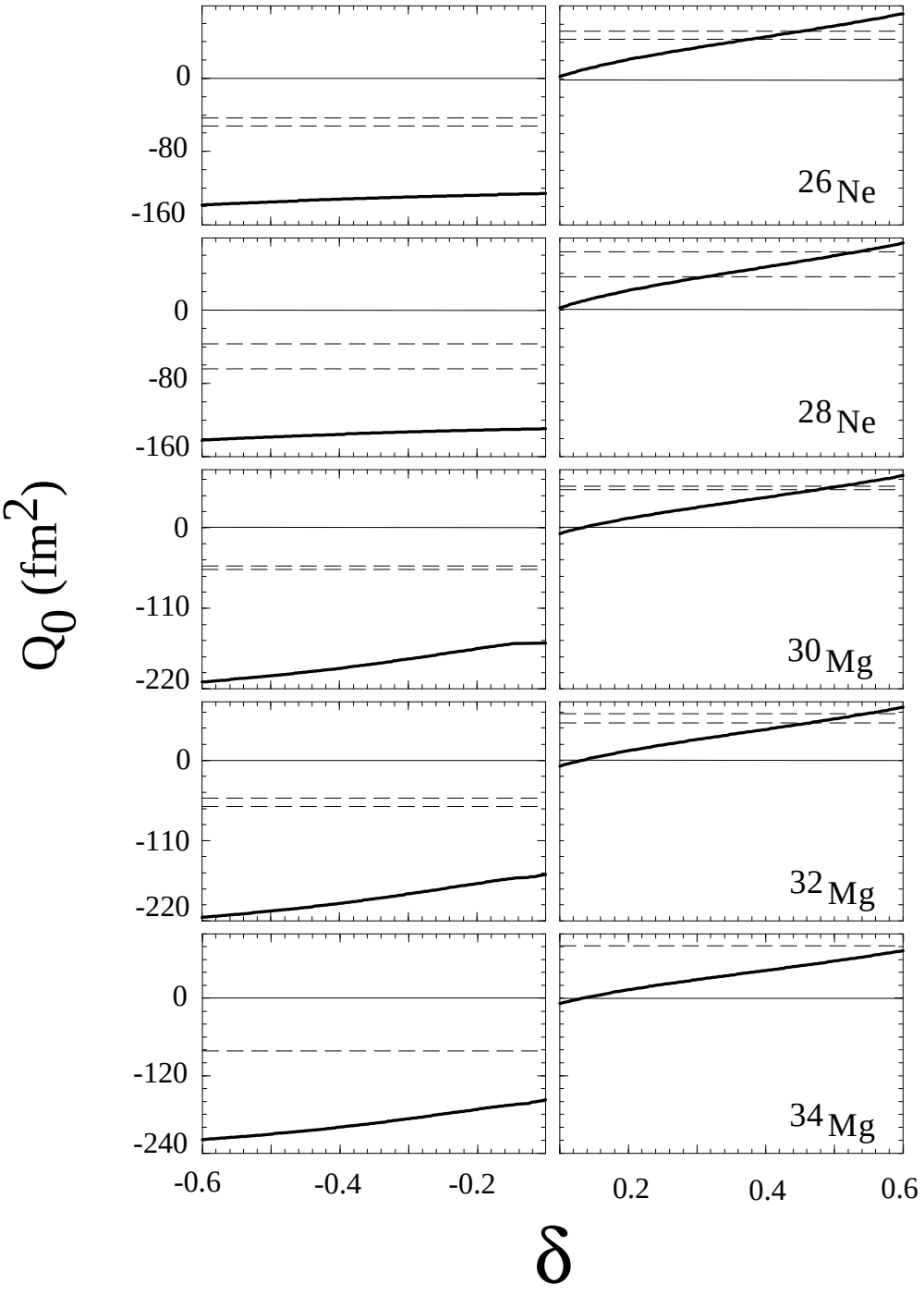

Figure 4.5: Calculations of electric quadrupole moments as a function of the deformation parameter δ for ^{26,28}Ne and ^{30,32,34}Mg. The "experimental" electric quadrupole moments are shown as bands bounded by dashed lines corresponding to experimental uncertainties. The bands are located at both positive and negative values since the experimental data cannot distinguish between prolate and oblate deformations.

suggests strong mixing between the intruder and normal configurations in this nucleus. We also determine the $B(E2; 0^+_{gs} \rightarrow 2^+)$ value for the lowest 2^+ state in ^{32}Mg to be 27% lower than the value reported by Motobayashi *et al.* [16]. The deformed shell model calculations demonstrate that if these nuclei have static axially symmetric deformations, they must be prolate.

4.4 Coulomb Excitation of Sodium Isotopes

Historically, the first evidence for the existence of the so-called island of deformed nuclei near the $N = 20$ shell closure was obtained in 1975 by Thibault *et al.* [10] from mass measurements of sodium isotopes. In particular, the authors of Ref. [10] wrote: "Then the behavior of the experimental data for the sodium isotopes at $N = 20$ is inconsistent with the classic shell closure effect, and more reminiscent of the behavior one observes when entering a region of sudden deformation." Experimental observation of the excited states in ^{28,29,30,31}Na is a main topic of this section. Nuclear properties of these isotopes will be presented and possible explanations will be discussed.

4.4.1 Experimental Observations for ^{28,29,30}Na

The cocktail beams used in this thesis work contained 38 different nuclei. This allowed us to study ^{28,29,30,31}Na fragments simultaneously. Figure 4.6 shows the Coulomb excitation data for ^{28,29,30}Na [72].

The 1240(11) keV transition is present in the ^{28}Na data. Two peaks are observed in the Doppler corrected spectrum of ^{30}Na. Additional tests, which were previously described in section 4.3, indicate that only the 433(16) keV transition belongs to ^{30}Na and the 700(20) keV line originates from the one-neutron-stripping reaction

two nucleons from the pf-shell [17].

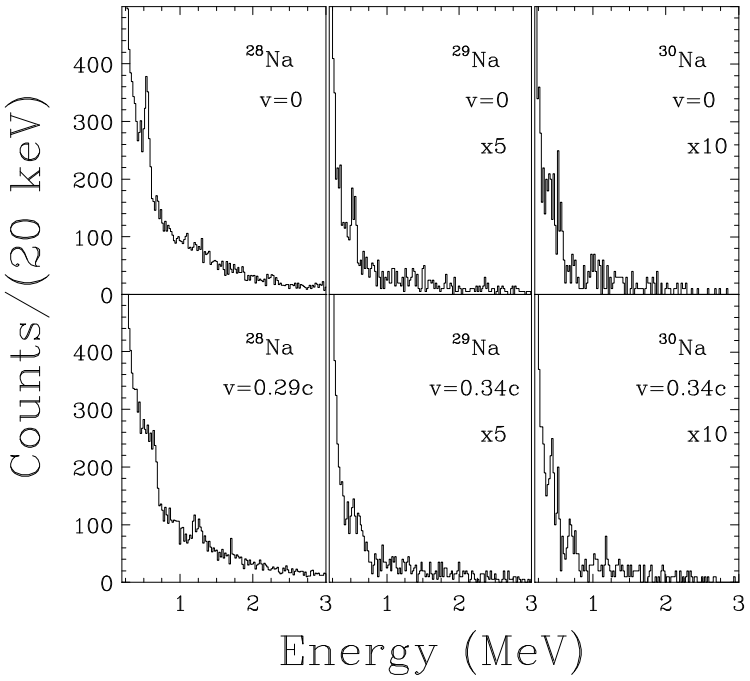

Figure 4.6: Experimental results for ^{28,28,30}Na. The upper panel show background photon spectra in the laboratory frame and the 547 keV ($7/2^+ \rightarrow g.s.$) transition in the gold target is visible as a peak. The lower panels show Doppler-corrected γ-ray spectra.

with $\sigma = 39.3(18.2)$ mb and further de-excitation of ^{29}Na. In fact a weak peak with such an energy can be seen in the ^{29}Na data. Observation of the one-neutron-stripping reaction in the ^{30}Na-data could be explained by the fact that ^{30}Na has the smallest neutron separation energy among the sodium isotopes ^{28,29,30,31}Na, which are 3520(80) keV, 4420(120) keV, 2100(130) keV and 4000(190) keV, respectively.

From the magnetic resonance measurements of ^{28,29,30}Na [74] we know that the spin and parity for the ground state are 1^+, $3/2$ and 2^+, respectively. Spin and parity assignments for the first excited states in ^{28,29,30}Na can be deduced assuming the rotational nature of collectivity as 2^+, $5/2^+$ and 3^+, respectively. These spin and parity assignments were used for the angular distribution in the calculation of excitation cross sections, which are presented in Table 4.4.

Table 4.4: Experimental parameters and results for sodium nuclei.

Nucleus	$E_{beam}^{midtarget}$ (MeV/A)	E_γ (keV)	σ (mb)	θ_{cm}^{max} (deg)
^{28}Na	43.11	1240(11)	26(6)	4.52
^{29}Na	59.97	700(20)	26(21)	3.21
^{30}Na	55.56	433(16)	42(14)	3.23
^{31}Na	51.54	350(20)	115(32)	3.24

4.4.2 Experimental Observations for ^{31}Na

Very little was known about the nuclear structure of ^{31}Na until the transition energy and excitation cross section for the first excited state were measured at the NSCL [72, 75]. Figure 4.7 demonstrates an observation of an excited state in ^{31}Na.

The low excitation energy $E_\gamma = 350(20)$ keV and the corresponding large cross section of $\sigma = 115(32)$ mb provide a clear indication that nuclear properties of ^{31}Na are very similar to those of ^{32}Mg. This is in agreement with a shell-model calculation of Caurier *et al.* [18] and B.A. Brown [73], who predicted that ground state of ^{31}Na is dominated by intruder configurations and the ground, first and second excited states should have spin and parity assignments $3/2^+$, $5/2^+$ and $7/2^+$, respectively. The theoretical prediction for the ground state spin in ^{31}Na agrees with an experimental value which can be deduced from optical measurements of G. Huber *et al.* [74], who wrote: "The spin assignment for ^{31}Na is based on a value of the hyperfine structure and the isotope shift which indicate that $I = \frac{3}{2}$ is the most probable value". In addition the shell-model calculation of Caurier *et al.* [18] predicts that the transition energy for the first excited state is $\sim$ 200 keV. The difference between theoretical and experimental transition energies can be explained by the incomplete knowledge

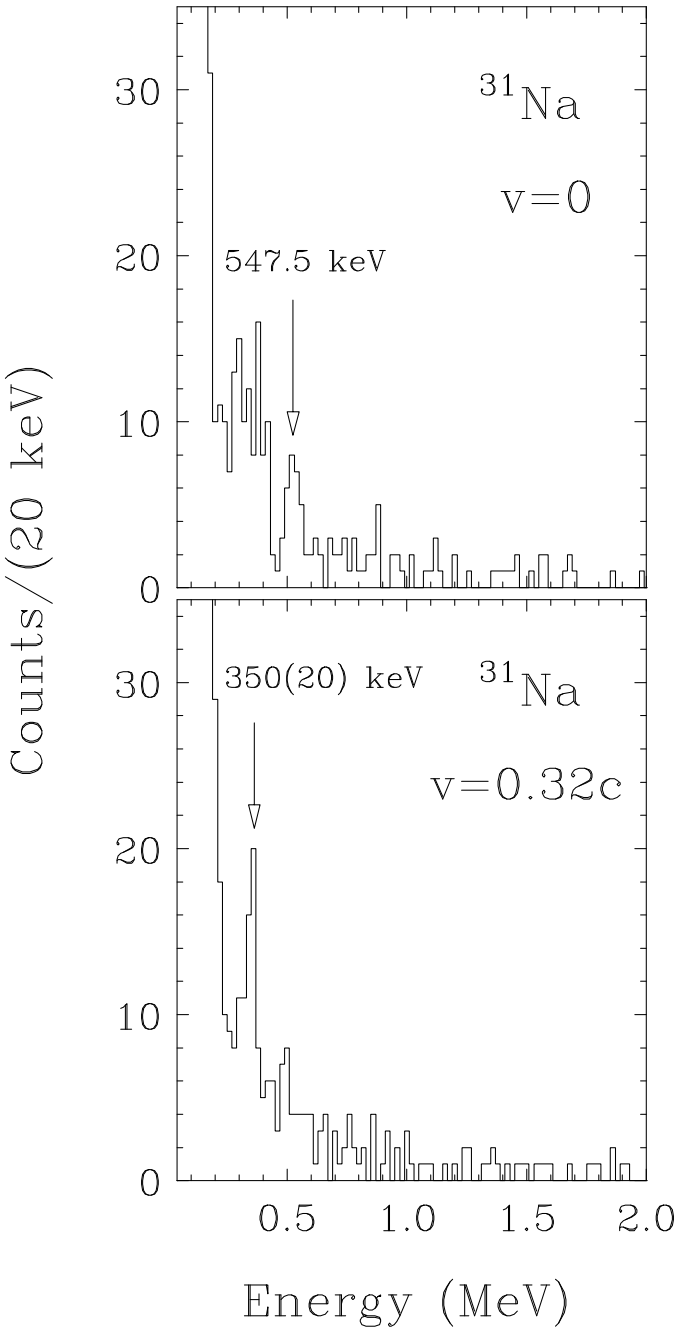

Figure 4.7: Energy spectrum of ^{31}Na. The upper panel shows photon spectra in the laboratory frame and the 547 keV ($7/2^+ \rightarrow g.s.$) transition in the gold target is visible as a peak. The lower panel shows Doppler-shifted γ-ray spectra and a peak at 350(20) keV becomes visible.

of nuclear interaction in this region [3] .

The relatively large error-bars for the Coulomb excitation cross section in Table 4.1 are predominantly statistical in origin due to the low intensity of the ^{31}Na beam. At the same time the observation of the 350 keV transition in ^{31}Na illustrates that in-beam γ-ray spectroscopy is possible with beam rates as low as 3 particles/sec.

4.4.3 Cross Section Corrections for ^{31}Na

The lack of the experimental decay scheme in ^{31}Na introduces additional uncertainties for the excitation cross section. The uncertainties associated with incomplete knowledge of the decay scheme, absorption of γ-rays in the secondary gold-target and conversion electrons are the main topics of the present subsection.

The experimental spin and parity assignment for the first excited state in ^{31}Na is unknown. Therefore the $5/2^+$ assignment is based on shell-model calculations for ^{31}Na by B.A. Brown (presented in subsection 4.4.4). Equations 2.28, 2.29 and 2.30 indicate that $E2$ and $M1$ transitions are possible and the experimental mixing ratio between them is unknown. The mixing ratio is defined as follows [31]

$$\delta^2 = \frac{W(E(\lambda+1); J_i \rightarrow J_f)}{W(M\lambda; J_i \rightarrow J_f)}, \tag{4.3}$$

where $W(\pi\lambda)$ are transition rates, which are directly proportional to reduced transition probabilities. Lets consider this problem in more detail:

- The $M1$ transition cannot be solely responsible for the excitation of ^{31}Na. This follows from the experiment because the corresponding $B(M1\uparrow)$ value would be roughly three times higher than the recommended upper limit [70, 71]. Such a conclusion is in agreement with the shell-model prediction for $B(M1, 3/2^+ \rightarrow 5/2^+)$

[3] In the most recent version of shell-model calculations of ^{31}Na, performed by the authors of Ref. [18], the first excited $5/2^+$ state is located at 284 keV.

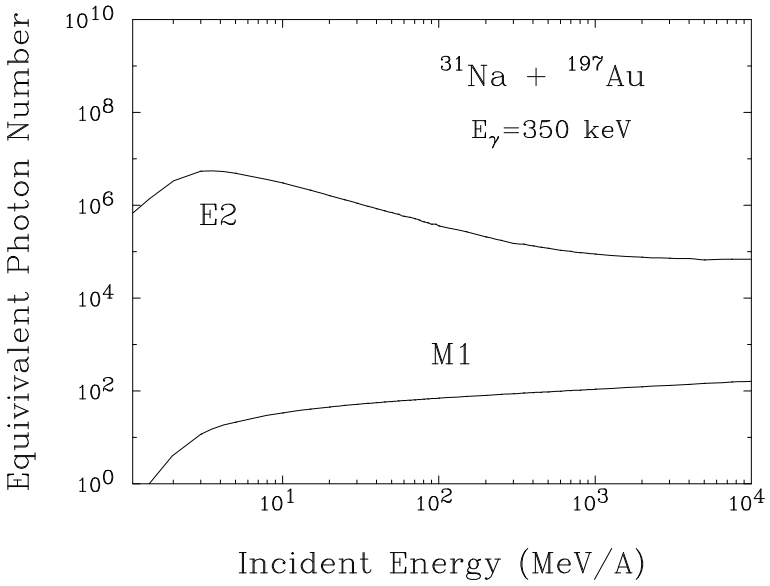

Figure 4.8: Equivalent photon numbers versus the incident beam energy for a ^{31}Na nucleus incident on a ^{197}Au target. The impact parameter distribution is integrated from $b_{min} = 16.46$ fm to infinity corresponding to a Coulomb excitation reaction. The transition energy in ^{31}Na is assumed to be $E_\gamma = 350$ keV.

$\approx 0.09\ \mu_N^2$ and corresponding excitation cross section of 0.236 mb . The small transition strength for the $M1$ excitation can be understood from the following argument. Coulomb excitation is often described as a photo-absorption of virtual photons [42, 77] and the total excitation cross section is proportional to a product of the equivalent photon number and photo-absorption cross sections. The numbers of equivalent photons for the $E2$ and $M1$ transitions are 669878.0 and 59.73, respectively. Assuming that the photo-absorption cross sections for $M1$ and $E2$ photons are of similar order of magnitude, one can conclude that $E2$ transitions are responsible for excitation of the $5/2^+$ state. The spectrum of equivalent photons for $M1$ and $E2$ multipolarities as a function of incident beam energy is presented in Figure 4.8.

• The $M1$ multipolarity dominates the de-excitation because the Doppler correction for fast beams ($v_p = 0.32c$) is applicable only when the life-time of the excited state is less than 10^{-10} sec and the decay occurs close to the target. A lifetime of 0.43 nsec for an $E2$ de-excitation would not allow a successful Doppler-shift proce-

dure. The observed peak at 350(20) keV indicates that the Doppler shift works and the de-excitations have an $M1$ nature. This is in agreement with the shell model prediction that $\delta^2 = W(E2)/W(M1) \approx 0$. In this particular case, a different mixing ratio would not change the angular distribution and thus the value of the excitation cross section, because the difference between detection efficiencies for the $M1$ and $E2$ multipolarities (0.1%) is much smaller than the efficiency error (4.1%).

Absorption of γ-rays in the Au-target is important for a correct determination of detection efficiency, especially for low-energy photons. Excited states in ^{31}Na can decay within the target or after passing it. Consequently the lifetime of the 350 keV state in ^{31}Na affects the detection efficiency as follows:

• Assuming that all gamma-emissions occur in the target, the detection efficiency for 350 keV photons has to be reduced from 18.5% to 13.4%. This increases the excitation cross section from 93(27) mb to 128(37) mb, and the corresponding $B(E2\uparrow)$ values from 394(115) e^2fm^4 to 543(159) e^2fm^4, respectively. For $E2$-transitions this would correspond to half-live time of 0.3 nsec. In this case 63.2% of the ^{31}Na nuclei decay within 42 mm from the target. The corresponding uncertainty for θ_{lab} in equation 2.36 is 15.9 %. Equation 2.37 indicates that this uncertainty in the photon scattering angle corresponds to a broadening in the energy resolution of $\left(\Delta E^{(\gamma)}_{lab}/E^{(\gamma)}_{lab}\right)_{\rm dopp} = 8.5$ %. Thus the energy resolution (FWHM) would decrease from the expected resolution of 11 % for a 350 keV photon [53, 55] to 14 %. This is inconsistent with the experimentally observed energy resolution (FWHM) of 9.3(2.7) % for the 350 keV photon shown in Figure 4.7. Therefore the decay has predominantly $M1$ multipolarity.

• If the decay is $M1$ in character, then the fraction of nuclei decaying in the target will be 6.2% (the half-life time for $B(M1\uparrow) = 0.09\ \mu_N^2$ is 15.3 psec and the flight distance in one half-life is 1.47 mm) and we correct for the absorption assuming that decays occur in the middle of the target. 99% of these nuclei decay within 7

half-life times, which correspond to a distance of 10.3 mm from the target. If the angular distribution was isotropic, we would have to correct for the absorption of half of these gammas (emitted backwards), using a correction about two times as much as compared to gammas emitted from the middle of the target. Since the fraction of nuclei decaying outside the target is 93.8%, and 12% of those go forward more than backwards, we should not apply the absorption correction to $0.12 \cdot 0.938 = 0.1126$ of the photons. The absorption correction is ~11.26% relative to the isotropic distribution, so we need to decrease the efficiency correction, which was 18.5% →13.43% by 11.26%, so the average efficiency will change $13.43\% \cdot 1.1126 = 14.94\%$. As the result of this, the cross section will be reduced from 128(37) mb to 115(32) mb or by 10%.

This cross section of 115(32) mb contains contributions from the electron conversion, nuclear excitations and a possible feeding contribution from the $7/2^+$ state which will be described in subsection 4.4.5. Conversion electrons are not a contributing factor because the beam is fully stripped. The beam can pick up electrons in the target producing a second-order effect (with an electron conversion coefficient ~4% [78]) and this correction is not included in the final cross section.

4.4.4 Shell-Model Calculations for ^{31}Na

In the first shell-model calculation of ^{31}Na, which was performed by Caurier *et al.* [18], spin and parity assignments and the transition energy of the first excited state were calculated. These parameters are not sufficient for interpretation of the ^{31}Na Coulomb excitation experiment [75]. Therefore a complete *OXBASH* shell-model calculation [4] of ^{31}Na was performed by B.A. Brown by using the same $sd - pf$ Hamiltonian and model space that was used in [80, 81, 76] for the neutron-rich Si, S and Ar isotopes.

[4] The *OXBASH* (Oxford-Buenos Aires-MSU) shell model code was developed by B.A. Brown, A. Etchegoyen and W.D.M. Rae in 1988 [79].

In this calculation, $2p-2h$ ($2\,\hbar\omega$) neutron excitations - which are responsible for the strong deformation in ^{32}Mg - were included in addition to the usual $0\,\hbar\omega$ configurations. The allowed $2\,\hbar\omega$ neutron configurations were $(d_{5/2})^6(d_{3/2}, s_{1/2})^4(f_{7/2}, p_{3/2})^2$, and the allowed proton configurations were $d^3_{5/2}$ and $d^2_{5/2}(s_{1/2}, d_{3/2})$. This calculation gives two concentrations of $E2$ strength. One is the first excited $J^\pi = 5/2^+$ state, as is observed in the experiment (although the energy is calculated to be 197 keV instead of the observed value of 350 keV). The second concentration of $E2$ strength is predicted to reside in a $J^\pi = 7/2^+$ state at 1.525 MeV. The $B(E2\uparrow)$ value for the $J^\pi = 7/2^+$ state is predicted to be 45% of the value for the $J^\pi = 5/2^+$ state. The absolute value of excitation cross section for $5/2^+$ state can also be affected by feeding from de-excitations of the $7/2^+$ state. The shell model predicts that $B(E2, 3/2^+ \rightarrow 7/2^+)$ = 87 e^{2}fm^4, which will correspond to 21.7 mb. This will result in 4.1 events at 1.1725 MeV, which is consistent with the experiment 3 ± 2 counts.

The shell model calculation of ^{31}Na also predicts a static axial quadrupole deformation with two deformation parameters, which reflect charge and matter density distributions. The *rms* radii [5] for charge and matter density distributions in ^{31}Na are presented in Table 4.5.

The first, the "Coulomb deformation" β_C, reflects the deformation of the proton fluid in the nucleus and corresponds to the electromagnetic matrix element $B(E2; I_{gs} \rightarrow I_f)$. In the rotational model [32], $B(E2; I_{gs} \rightarrow I_f)$ and β_C are related via the equations

$$B(E2; I_i \rightarrow I_f) = \frac{5}{16\pi} Q_0^2 < I_i K 20 | I_f K >^2 \qquad (4.5)$$

[5] The *rms* radii are related to the "rigid sphere" radii by equation:

$$R^2_{rms} = \frac{3}{5} R^2_{rigid}\,. \qquad (4.4)$$

Table 4.5: Charge and matter density distributions in ^{31}Na.

Particles	Shell model rms radii (fm)	Rigid sphere radii (fm)
Protons	2.9550	3.815
Neutrons	3.3232	4.290
Protons+Neutrons	3.1974	4.128

and

$$Q_0 = \left(\frac{16\pi}{5}\right)^{1/2} \frac{3}{4\pi} ZeR^2\beta\,, \tag{4.6}$$

where Q_0 is the intrinsic quadrupole moment. The rigid sphere radius R can be approximated by $R = r_0 A^{1/3}$, where we take $r_0 = 1.20\ fm$. For the $5/2^+$ state, the shell model result ($B(E2; 3/2 \rightarrow 5/2) = 196\ e^2fm^4$) gives a prediction of $\beta_C = 0.51$. In the case of the $7/2^+$ state, the shell model calculation gives $B(E2; 3/2 \rightarrow 7/2)$ $= 87.5\ e^2fm^4$, so that $\beta_C = 0.46$. Deformation parameters can be expressed as a function of $B(E2\uparrow)$ values and rigid sphere radii as the following:

$$|\beta_2| = \frac{4\pi}{3} \frac{\sqrt{B(E2)}}{ZeR^2} \frac{1}{\langle J_i K 20 | J_f K\rangle}\,, \tag{4.7}$$

where the corresponding Clebsch-Gordan coefficients for $3/2^+ \rightarrow 5/2^+$ and $3/2^+ \rightarrow 7/2^+$ transitions are $\sqrt{18/35}$ and $\sqrt{2/7}$, respectively.

The second deformation parameter in the calculation is the "nuclear deformation parameter" β_N. While the Coulomb deformation parameter is used to calculate the electromagnetic interaction between target and projectile, the nuclear deformation parameter is used to determine the interaction via the nuclear force. In the standard collective model, the neutron and proton fluids are assumed to have the same deformation. In such a case, the nuclear deformation parameter could be set in a trivial way: $\beta_N = \beta_C = \beta$ [16]. However, the present shell model calculations yield results for

neutron and proton transition multiple matrix elements which are not consistent with the standard collective model picture. The neutron transition matrix element for the $5/2^+$ state in ^{31}Na is $B(E2; 3/2 \rightarrow 5/2) = 252\ e^2fm^4$ and $\beta_C = 0.46$. In the case of the $7/2^+$ state, the shell model calculation gives $B(E2; 3/2 \rightarrow 7/2) = 171\ e^2fm^4$, so that $\beta_C = 0.51$. Transition matrix elements for the nuclear fluid (protons+neutrons) can be estimated as 0.5·(proton+neutron) values.

4.4.5 ECIS Calculations of ^{31}Na

The present shell model calculation predicts electromagnetic matrix elements connecting members of the ground state rotational band, but a reaction model is necessary to translate the shell model predictions into experimental cross sections for the 5/2 and 7/2 states in the present scattering experiment. These calculations were performed by L.A. Riley, who used the coupled-channels code ECIS88 [82] with an optical model parameter set determined for the ^{17}O+^{208}Pb reaction at 84 MeV/nucleon [83] to calculate the angular distributions, and then integrated the angular distribution out to the maximum scattering angle measured in the experiment ($\theta^{\rm lab}_{\rm max} = 2.8^\circ$) with an average beam energy of 51.5 MeV/nucleon. The phenomenological potentials and input data file for the ECIS calculation are presented in Appendix D.

The coupled-channels calculations using the predicted shell-model calculation deformation parameters yield 54 mb for the 5/2 state and 27 mb for the 7/2 state, see Table 4.6. If 95% of the decays of the 7/2 state go to the 5/2 state, the cross section for producing the 350 keV γ-ray would be 81 mb. Since the experimental result is 115 ± 32 mb, we conclude that the shell model calculation does reproduce the measurement.

One issue relevant to this study is understanding the role of the nuclear interaction in the scattering reaction measured here. We performed a calculation in which the

Table 4.6: ECIS calculation. Excitation cross sections (integrated over $\theta_{cm} \leq 3.25°$) for states in ^{31}Na from coupled channels calculations with an optical model parameter set determined for the ^{17}O + ^{208}Pb reaction at 84 MeV/A [83].

Transition	σ_{Coul} (mb)	σ_{Nucl} (mb)	σ_{Tot} (mb)	β_C	β_A
Shell model					
$3/2^+ \rightarrow 5/2^+$	49.1	7.8	54.2	0.510	0.470
$3/2^+ \rightarrow 7/2^+$	23.7	5.0	27.3	0.460	0.470
Fit to data					
$3/2^+ \rightarrow 5/2^+$	64.9	11.7	73.1	0.587	0.587
$3/2^+ \rightarrow 7/2^+$	39.4	7.5	44.6	0.587	0.587

nuclear interaction was set to zero (Coulomb only), another in which the Coulomb interaction was set to zero (nuclear only) and a third in which both interactions were used. The angular distributions for these calculations for inelastic scattering to the 5/2 state are shown in Figure 4.9. We conclude that the nuclear interaction accounts for $\approx$ 15% of the cross section for the angular range detected in this experiment. Coulomb excitation plays the dominant role in this experiment, but scattering via the nuclear force cannot be neglected.

We can also use the standard rotational model (where the proton and neutron deformations are equal) to directly extract a quadrupole deformation parameter β_2 from the data. For this fit, we assume that $\beta_C = \beta_N$, that the deformation parameters for the 5/2 and 7/2 states are equal, and that 95% of the de-excitations of the 7/2 state go to the 5/2 state. The result, $\beta_2 = 0.59(8)$, is close to the deformation parameters obtained for ^{32}Mg [16, 17]. This result reflects only the experimental uncertainty,

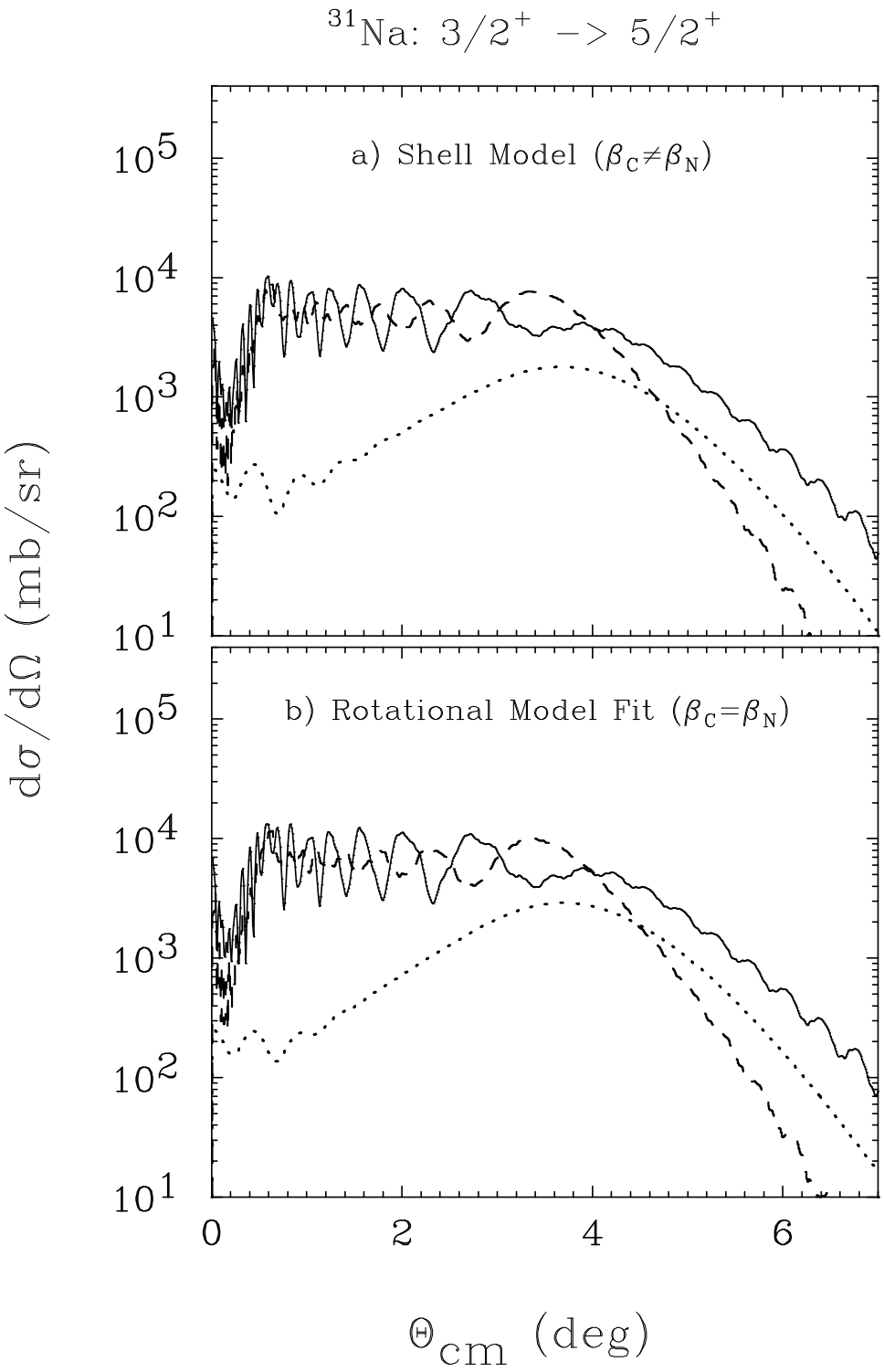

Figure 4.9: ECIS calculation. Shown is the angular distribution of the reaction ^{197}Au(^{31}Na,^{31}Na*)^{197}Au exciting the 5/2$^+$ state of ^{31}Na. The dotted and dashed curves represent the cross sections for the nuclear and Coulomb excitations, respectively. The solid curve corresponds to the coherent sum of two excitations.

Table 4.7: Experimental upper limits on reduced transition probabilities for assumed $E1, E2, M1$ and $M2$-transitions in ^{28,29,30,31}Na deduced from the measured excitation cross sections in Table 4.4.

Nucleus	$B(E1\uparrow)$ (e^2fm^2)	$B(E2\uparrow)$ (e^2fm^4)	$B(M1\uparrow)$ (e^2fm^2)	$B(M2\uparrow)$ (e^2fm^4)
^{28}Na	$\leq 0.0182(40)$	$\leq 86.7(19.3)$	$\leq 0.2912(634)$	$\leq 1234(276)$
^{29}Na	$\leq 0.0062(45)$	$\leq 47.7(35.1)$	$\leq 0.066(50)$	$\leq 436(321)$
^{30}Na	$\leq 0.0236(80)$	$\leq 186.2(62.8)$	$\leq 0.205(69)$	$\leq 1800(608)$
^{31}Na	$\leq 0.0452(128)$	$\leq 543.1(158.6)$	$\leq 0.540(153)$	$\leq 5489(1604)$

an additional theoretical uncertainty which reflects the model dependence can be introduced. Finally, the deformation parameter is $\beta_2 = 0.59 \pm (0.08)$ (experimental) $\pm$ (0.06) (theoretical).

4.4.6 Data Interpretation

All experimental excitation cross sections in Table 4.4 were corrected for possible theoretical and experimental uncertainties due to incomplete knowledge of spin and parity assignments and mixing ratios in ^{28,29,30,31}Na. These cross sections were used to deduce the upper limits on reduced transition probabilities in sodium isotopes by using the usual Winther and Alder formalism [35]. Table 4.7 presents the reduced transition probabilities for the sodium isotopes.

Table 4.8 presents the recommended upper limits for γ-ray strength for light isotopes ($21 \leq A \leq 44$) [70, 64, 71] and the Weisskopf (single-particle) estimates of the reduced transition strengths [31, 84]. The products of the recommended upper limits for γ-ray strength and the Weisskopf (single-particle) estimates are equal to the upper

Table 4.8: Recommended upper limits for reduced transition probabilities in light isotopes ($21 \leq A \leq 44$). Recommended γ-strengths are taken from [70, 71] and Weisskopf (single-particle) estimates of the reduced transition strengths are extracted from Refs. [31, 84].

Transition $E\lambda$ or $B\lambda$	Recommended γ-strength Γ_γ/Γ_w	Weisskopf (single-particle) estimates $e^2fm^{2\lambda}$ or $\mu_N^2 fm^{(2\lambda-2)}$
$E1$	0.1	$\leq 6.413 \cdot 10^{-2} \cdot A^{2/3}$
$E2$	100	$\leq 5.883 \cdot 10^{-2} \cdot A^{4/3}$
$E3$	100	$\leq 5.899 \cdot 10^{-2} \cdot A^{2}$
$E4$	100	$\leq 6.238 \cdot 10^{-2} \cdot A^{8/3}$
$M1$	10	≤ 1.777
$M2$	3	$\leq 1.645 \cdot A^{2/3}$
$M3$	10	$\leq 1.64 \cdot A^{4/3}$
$M4$		$\leq 1.736 \cdot A^{2}$

limits on collectivities. In fact, recommended γ-strengths and corresponding upper limits on reduced transition probabilities are for transitions from the upper to the lower levels. The ratio between reduced transition probabilities can be derived as

$$B(\uparrow) = \frac{2J+1}{2J_0+1} B(\downarrow)\,, \tag{4.8}$$

where J_0 and J are spins of the lower and upper levels, respectively. It is often more convenient to present results for magnetic excitations in units of μ_N instead of e·fm. This can be accomplished with a ratio 1 $\mu_N = \frac{e\,\hbar}{2M_p c} = 0.105$ e·fm.

Figure 4.10 presents recommended and experimental upper limits on reduced transition probabilities for $E1, E2, M1$ and $M2$-transitions in ^{28,29,30,31}Na. Comparison

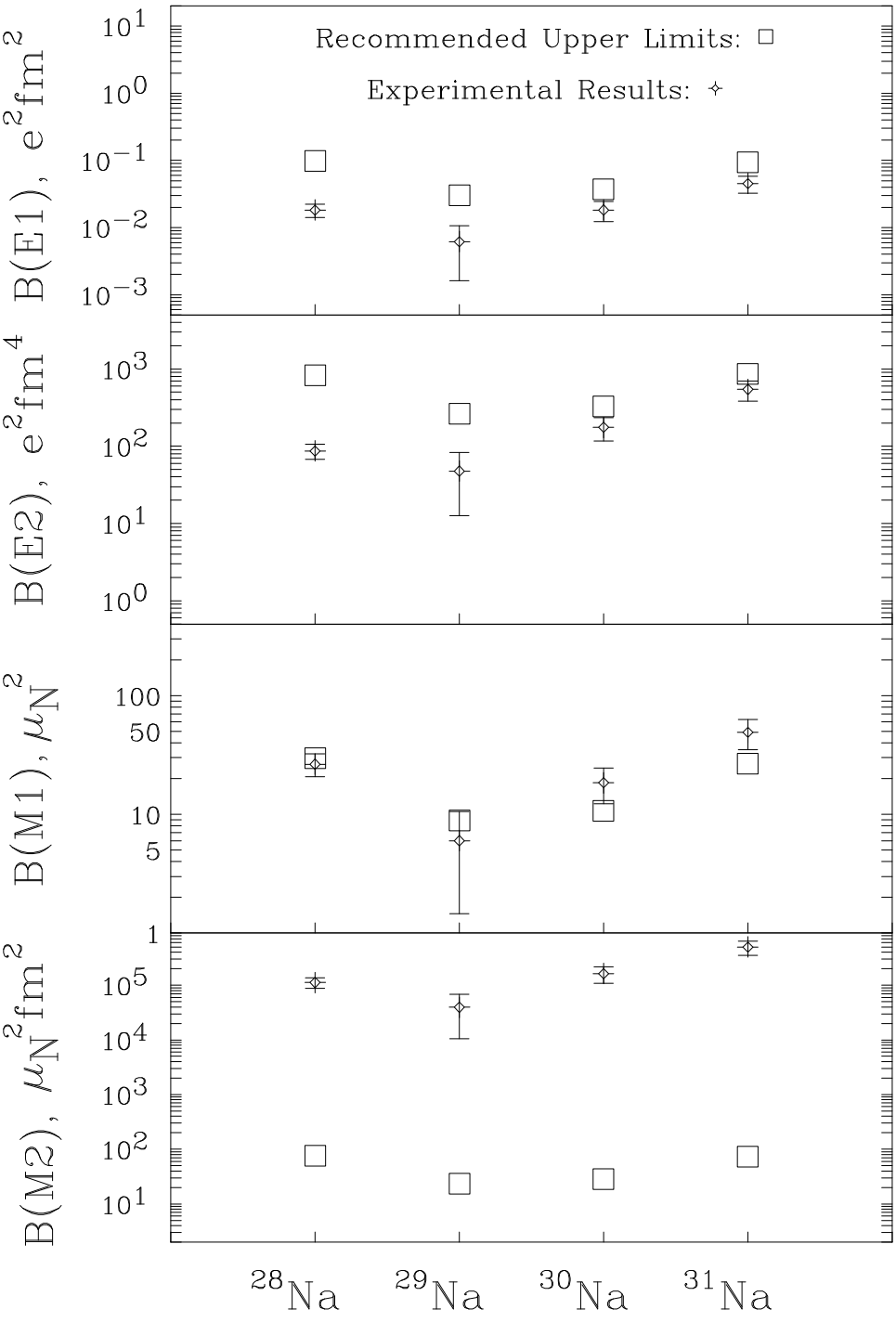

Figure 4.10: Recommended and experimental upper limits on reduced transition probabilities for $E1, E2, M1$ and $M2$-transitions in ^{28,29,30,31}Na.

between recommended and experimental upper limits on reduced transition probabilities indicate that the experimental cross sections are consistent with $E1$, $E2$ and $M1$ (for ^{28,29}Na) nature of excitation and $M2$ excitations are completely excluded as a possible explanation.

4.4.7 Intrinsic Quadrupole Moments in ^{28,29,30,31}Na

In the previous section the ^{31}Na data was explained on the basis of shell model calculations. The same data could have another interpretation if the possible feeding corrections are ignored. To understand the nature of deformation in sodium we will compare our data with the measured values of the intrinsic electric ground state quadrupole moments. The intrinsic electric ground state quadrupole moments can be extracted from [85] using the formalism described in [30] and our knowledge of the ground state spin assignments. The same values for the transition moments can be obtained from our results on $B(E2)$ (assuming pure $E2$ excitations) and the formalism described in [32].

In general, intrinsic electric quadrupole moments values for static deformations (rigid rotator) are not affected by excitations. On the contrary, for dynamic deformations transition intrinsic electric quadrupole moments are always larger than ground state quadrupole moments. The results (presented in Figure 4.11) suggest that ^{28,29,30}Na are statically deformed (rotational nuclei). At the same time the observed difference between intrinsic electric quadrupole moments for the ground and transition states in ^{31}Na would indicate the presence of dynamic deformation (a vibrational nucleus) [72]. The experimental data do not allow us to discriminate between the two possible interpretations (rotational or vibrational) of collectivity in ^{31}Na. A measurement of the energy level structure of ^{31}Na would elucidate this question.

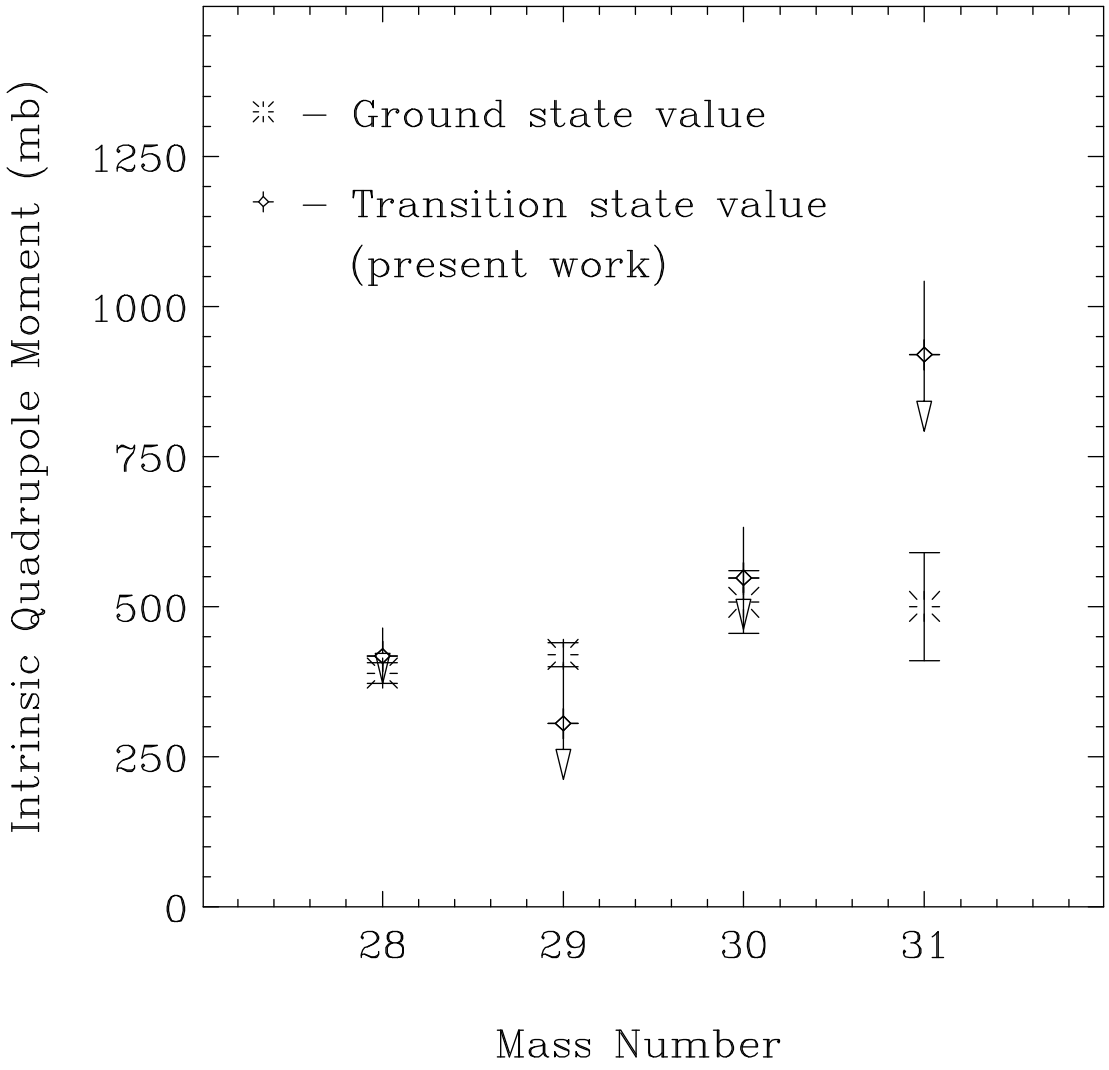

Figure 4.11: Intrinsic electric quadrupole moments for the ground and transition states in sodium isotopes (ignoring possible feeding from the higher-lying states). Data for the intrinsic electric ground state quadrupole moments were taken from [85].

Table 4.9: Coulomb excitation of ^{31,33}Mg, ^{34,35}Al, ^{33}Si and ^{34}P. Spin and parity assignments for electromagnetic transitions from the shell-model calculations [5] (denoted by $*$), [73] (denoted by $\star$) and spin and parity assignments extracted from the nuclear systematics [62] (denoted by †).

Nucleus	$E_{beam}^{midtarget}$ (MeV/A)	E_γ (keV)	J^π (assumed)	σ (mb)	θ_{cm}^{max} (deg)
^{31}Mg	62.08	905(13)	$3/2^{+*}_{g.s.} \rightarrow 5/2^{\pm\dagger}$	30.7(11.5)	3.24
^{33}Mg	53.82	478(5)	$7/2^{-*}_{g.s.} \rightarrow 3/2^{\pm\dagger}$	81.3(25.0)	3.27
^{34}Al	59.70	657(9)	$4^{-*}_{g.s.} \rightarrow 3^{\pm\dagger}$	24.2(9.5)	3.28
^{35}Al	55.83	1023(8)	$5/2^{+*}_{g.s.} \rightarrow 3/2^{\pm\dagger}$	30.3(13.5)	3.30
^{33}Si	40.84	1010(7)	$3/2^{+*}_{g.s.} \rightarrow 1/2^{+\star}$	4.1(0.80)	3.96
		4200(100)	$3/2^{+*}_{g.s.} \rightarrow 5/2^{+\star}$	11.6(2.2)	4.62
^{34}P	44.38	422(7)	$1^{+}_{g.s.} \rightarrow 2^{+\star}$	5.2(2.4)	4.64
		627(9)	$1^{+}_{g.s.} \rightarrow 2^{+\star}$	6.8(3.0)	3.96

4.5 Coulomb Excitation of ^{31,33}Mg, ^{34,35}Al, ^{33}Si and ^{34}P

Odd isotopes such as ^{31,33}Mg, ^{34,35}Al and ^{33}Si, ^{34}P were also produced as ^{48}Ca and ^{40}Ar fragments and studied. The first four nuclei are located in the island of inversion region and they are important for understanding the collectivity among odd isotopes in the region. ^{33}Si and ^{34}P provide a test case for comparison of the N$\sim$20 isotones, because these two nuclei are not dominated by intruder configurations. Results of the experimental observations are presented in Table 4.9.

In the present data analysis the ground state spin and parity assignments are

Table 4.10: Experimental upper limits for reduced transition probabilities in odd nuclei. n/a - denotes multipolarities excluded by selection rules in the cases of known spins and parities.

Nucleus	E_γ (keV)	$B(E1\uparrow)$ (e^2fm^2)	$B(E2\uparrow)$ (e^2fm^4)	$B(M1\uparrow)$ (e^2fm^2)
^{31}Mg	905(13)	$\leq 0.019(7)$	$\leq 124.6(46.5)$	$\leq 0.200(74)$
^{33}Mg	478(5)	$\leq 0.035(10)$	$\leq 343.5(105.5)$	$\leq 0.401(120)$
^{34}Al	657(9)	$\leq 0.013(5)$	$\leq 101.1(39.7)$	$\leq 0.135(52)$
^{35}Al	1023(9)	$\leq 0.020(9)$	$\leq 124.6(55.7)$	$\leq 0.240(106)$
^{33}Si	1010(7)	n/a	$\leq 16.5(3.2)$	$\leq 0.044(8)$
^{34}P	422(7)	n/a	$\leq 20.2(9.6)$	$\leq 0.025(11)$
	627(9)	n/a	$\leq 26.5(11.7)$	$\leq 0.16(7)$

taken from the shell-model calculations by Warburton *et al.* [5] and excited states assignments are deduced from shell-model calculations by Brown [73] and the systematic behavior of light nuclei [62]. Different spin and parity assignments for the excited states can change excitation cross sections by 5-10%.

The observed excitation cross section of ^{33}Mg is much larger than cross sections in ^{31}Mg and ^{34,35}Al and comparable to that of ^{32}Mg. This indicates that ^{33}Mg belongs to the island of inversion, while ^{31}Mg, and ^{34,35}Al lie outside the island. These cross sections contain possible contributions from nuclear excitation and feeding from the higher-lying levels. These results are in very good agreement with the theoretical predictions for light nuclei [5, 12, 18].

Table 4.10 presents the upper limits on reduced transition probabilities for different transitions in odd isotopes.

Excitation cross sections and reduced transition probabilities in ^{33}Si and ^{34}P are small and consistent with Weisskopf (single-particle) estimates of the reduced transition strengths, which are presented in Table 4.8.

Figure 4.12 shows results of the data analysis and the recommended upper limits [70, 71] for odd isotopes. Comparison between them indicates that this experiment is consistent with $E1$, $E2$, and $M1$ excitations while $M2$ excitations are completely excluded as a possible explanation.

4.5.1 Odd Isotopes of ^{31,33}Mg and ^{34,35}Al

Beams of the neutron-rich radioactive isotopes ^{31,33}Mg and ^{34,35}Al have been produced by fragmentation of a ^{48}Ca primary beam at 80 MeV/nucleon. The energies and excitation cross sections to the lowest excited states were measured via intermediate-energy Coulomb excitation on a ^{197}Au target. Study of these nuclei is important because shell-model calculations of Caurier *et al.* [18] predict that intruder states can be also observed in $N = 21$ nuclei such as ^{31}Ne, ^{32}Na and ^{33}Mg. Figure 4.13 shows the Coulomb excitation spectrum of ^{33}Mg. This spectrum contains a 484.9(1.0) keV line, which was previously observed but not identified as belonging to ^{33}Mg in the β-decay of ^{33}Na [14]. Observation of the 484.9(1.0) keV transition with a large excitation cross section of 81(25) mb is consistent with the presence of intruder configurations in ^{33}Mg.

Neutron-stripping reactions in ^{33}Mg were observed as two small peaks with energies $\sim$900 keV and $\sim$1450 keV, which are equivalent to the transition energies in ^{32}Mg. To prove this hypothesis two different particle gates (see discussion in subsection 4.3.1 were created for ions with higher than average (pure ^{33}Mg beam) and lower than average total energy (^{33}Mg + ^{32}Mg beam). The γ-spectra collected in coincidence with these gates are presented in Figure 4.14. This data cut shows that

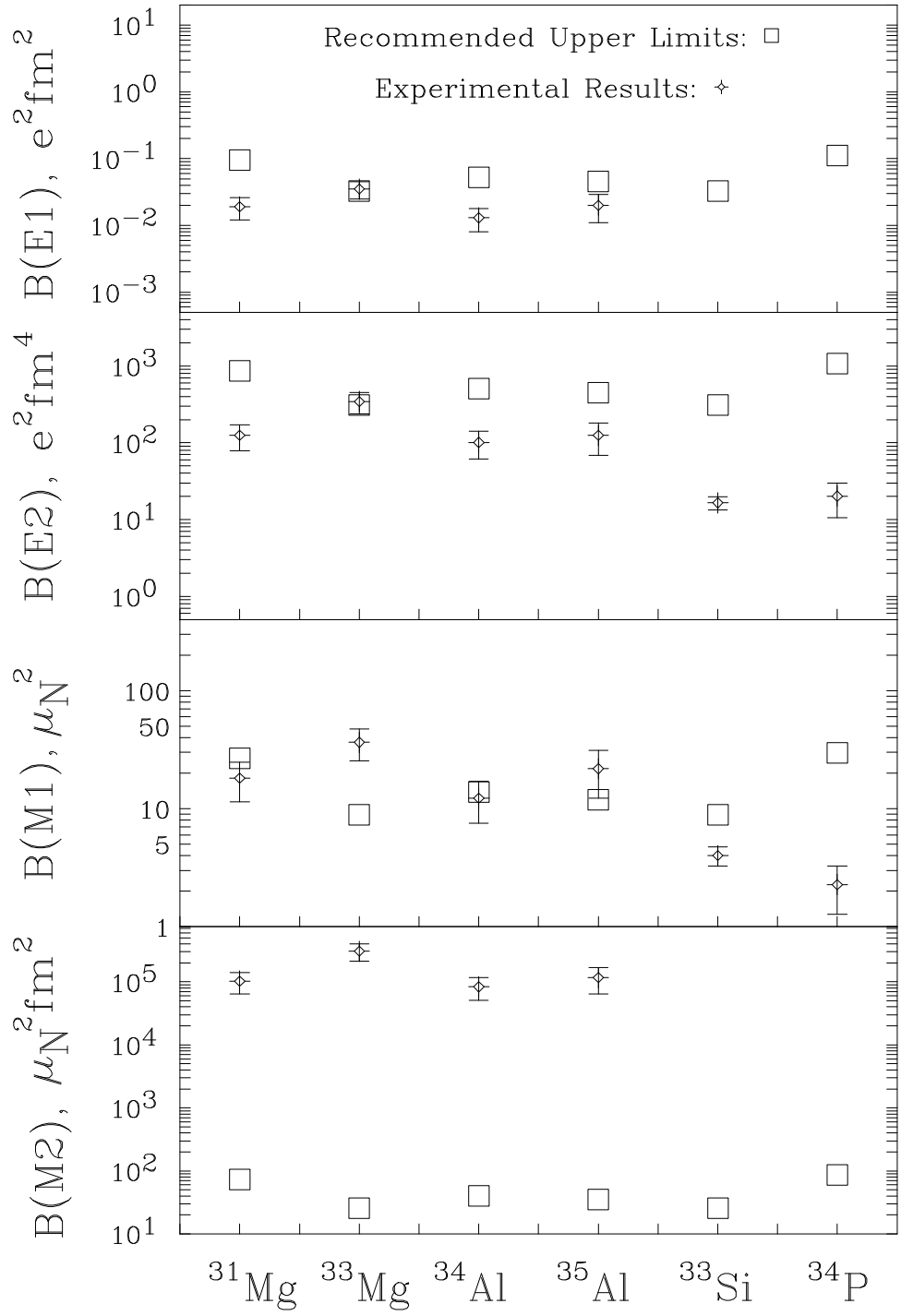

Figure 4.12: Recommended upper limits and experimental results in ^{31,33}Mg, ^{34,35}Al, ^{33}Si and ^{34}P. Recommended upper limits are extracted from [70, 71] and experimental upper limits are deduced using the formalism described in [35].

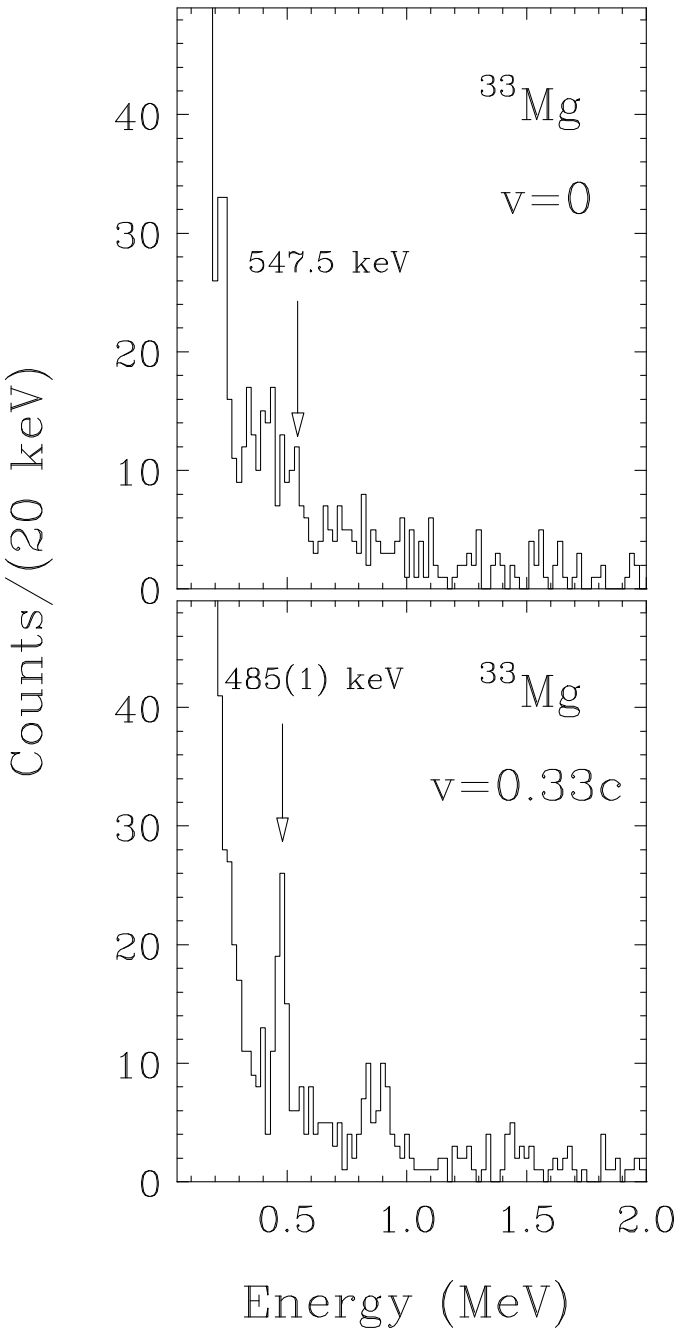

Figure 4.13: Energy spectrum of γ-rays emitted from the ^{33}Mg+^{197}Au reaction at 54.3 MeV/nucleon. Upper panel contains photon spectra in the laboratory frame and lower panel contains Doppler-shifted γ-ray spectra.

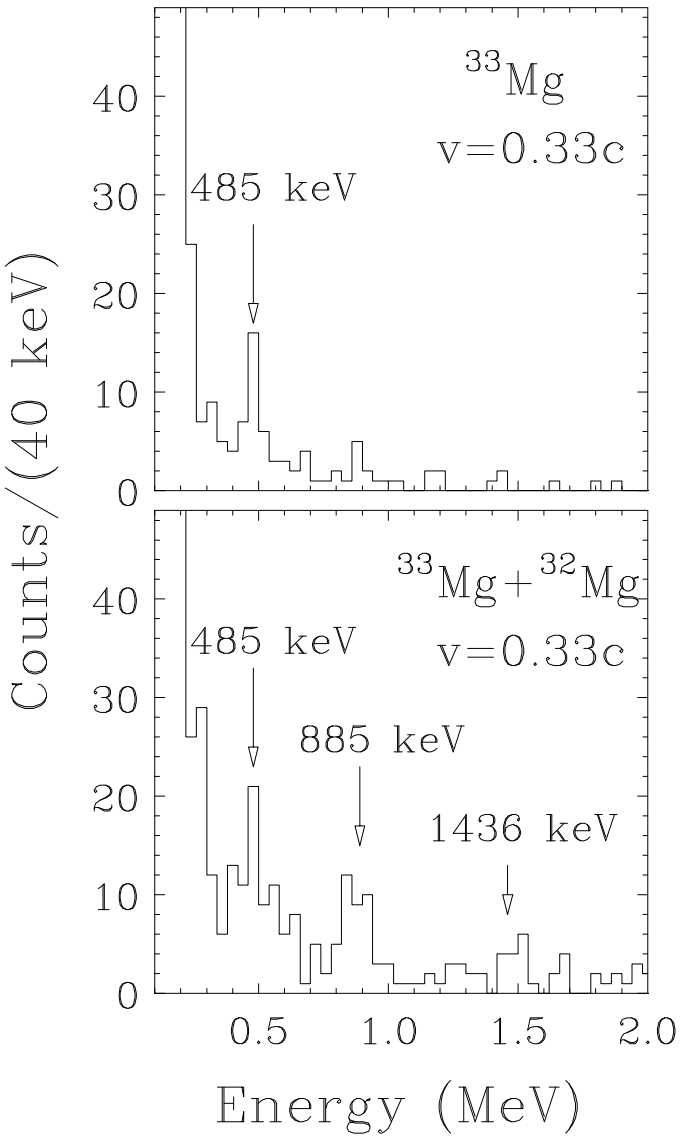

Figure 4.14: One-neutron removal in ^{33}Mg. Doppler-shifted γ-spectra for the ^{33}Mg and ^{33}Mg +^{32}Mg particle gates.

the 484.9(1.0) keV transition belongs to the ^{33}Mg level scheme and the ∼900 keV and ∼1450 keV transitions originate from de-excitations in ^{32}Mg. The partial cross sections for neutron stripping in ^{33}Mg which lead to the excitation of 885.5 keV and 1436.1 keV transitions in ^{32}Mg are $\sigma = 98(30)$ mb and $\sigma = 45(25)$ mb, respectively.

In contrast, ^{31}Mg has a smaller excitation cross section than ^{32}Mg and its value is comparable with that of another $N = 19$ nucleus, ^{30}Na. This result provides experimental indication that the properties of ^{31}Mg can be explained in the context of $0\,\hbar\omega$ configurations.

Transition energies and excitation cross sections for ^{34,35}Al are presented in Table 4.9. The present result for ^{35}Al is in agreement with the previous work of R.W. Ibbotson *et al.* [86], while the excitation cross section for ^{34}Al is smaller than that of another $N = 21$ isotope ^{33}Mg. Comparison of the nuclear properties of ^{34,35}Al and ^{32,33}Mg indicates that the properties of aluminum isotopes can be understood within the normal $0\,\hbar\omega$ configurations.

4.5.2 N = 19 Isotopes of Silicon and Phosphorus

Beams of ^{33}Si and ^{34}P were produced via fragmentation of a primary ^{40}Ar beam at 90 MeV/nucleon. The γ-ray spectra of ^{33}Si and ^{34}P are presented in Figure 4.15.

The observed excitation cross section of the first excited state in ^{33}Si is substantially smaller than those in ^{32,34}Si [76] and comparable to its single-particle value estimate. Shell-model calculations of B.A. Brown [73] predict that in ^{33}Si the ground state is a $d_{3/2}$ neutron hole and the 1010(7) keV excited state is the $s_{1/2}$ neutron hole state. The calculated $B(E2\uparrow) = 19$ e^{2}fm^4 is in very good agreement with the measured value of $B(E2\uparrow) = 17(3)$ e^{2}fm^4. The relatively strong $E2$ transition strength arises from the change in the orbital angular momentum of $2\,\hbar$ between the $d_{3/2}$ and $s_{1/2}$ nuclear orbitals.

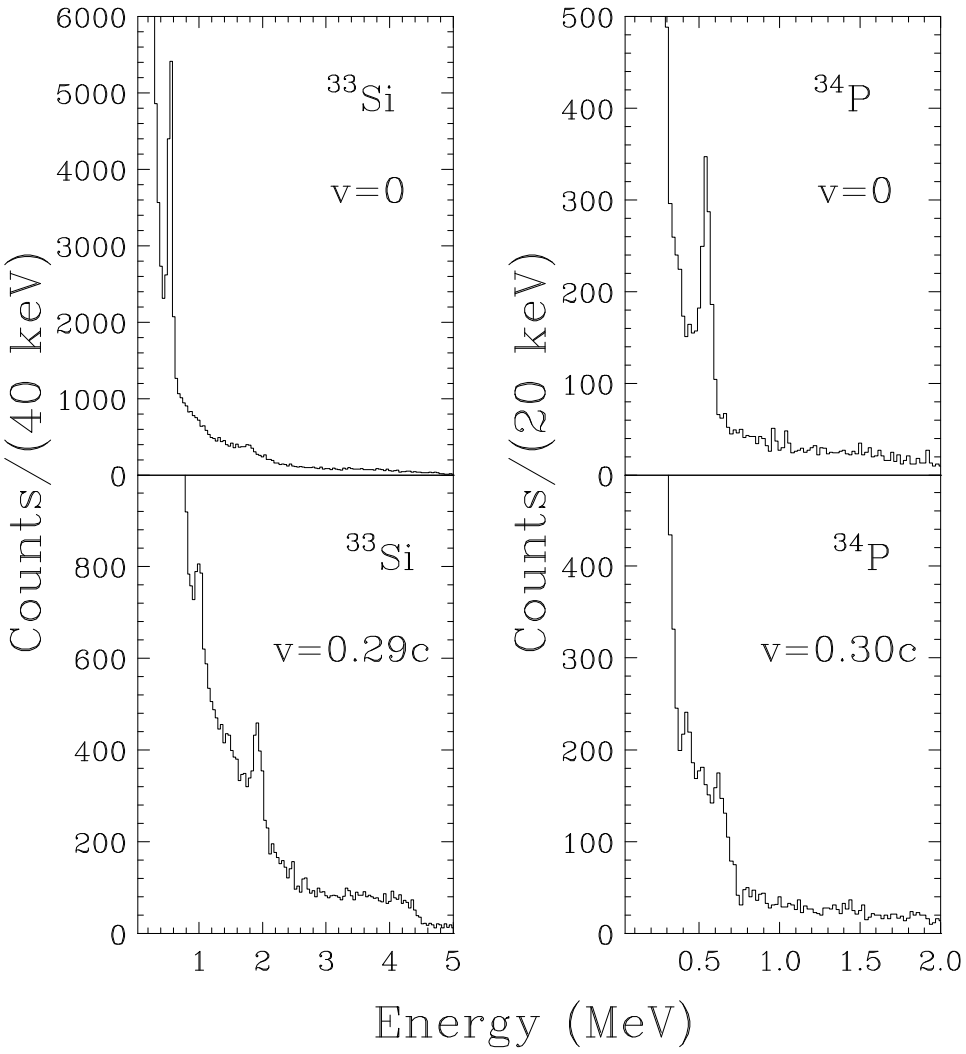

Figure 4.15: Experimental γ-ray spectra of ^{33}Si and ^{34}P. Upper panels contain photon spectra in the laboratory frame and lower panels contain Doppler-shifted γ-ray spectra. The 547 keV ($7/2^+ \rightarrow g.s.$) transition in the gold target is visible as a peak, while 1010 keV, 1941.5 keV and 429 keV, 625 keV transitions are present in the Doppler-shifted γ-ray spectra of ^{33}Si and ^{34}P, respectively.

The shell model predicts the next concentration of $E2$ strength to occur at 4 MeV, and this might correspond to the 2^+ state built on the ground state in ^{34}Si. The high-energy part of the ^{33}Si spectrum behaves like a step-function at 4.2-4.3 MeV, which indicates a possible excitation of the 4330(30) keV state in ^{33}Si [62] or a neutron-stripping reaction and further de-excitation of the second 2^+ state in ^{32}Si at 4230.8 keV. The extracted cross section of 11.6(2.2) mb and corresponding $B(E2\uparrow)$ = 69(13) e^{2}fm^4 are in a very good agreement with the theoretical prediction for the $E2$ strength at 4 MeV.

A neutron-stripping reaction in ^{33}Si with further 1941.5 keV transitions in ^{32}Si and a corresponding cross section σ = 11.7(1.4) mb was observed. The difference in cross section values for neutron-stripping reactions in magnesium and silicon can be explained by the neutron separation energies, which are 2070(170) keV and 4483(16) keV in ^{33}Mg and ^{33}Si, respectively.

According to the shell-model calculations of B.A. Brown [73] in ^{34}P both the ground state and the 429 keV state are members of the multiplet formed by the coupling of a $s_{1/2}$ proton to the $d_{3/2}$ neutron hole. Multiplet members are usually connected by $M1$ transitions, not $E2$ transitions. The difference between the shell-model predicted $B(E2\downarrow)$ = 0.18 e^{2}fm^4 and the experimentally measured upper limit on $B(E2\downarrow)$ = 12(6) e^{2}fm^4 supports the $M1$ nature of decay. The $M1$ nature of de-excitation is also in agreement with the observation of the 429 keV transition in the Doppler-reconstructed energy spectrum of ^{34}P because at intermediate energies the ^{34}P ions will travel up to 28.7 cm before decaying via $E2$ transition.

The next multiplet up in energy is one formed by the coupling of the $d_{3/2}$ neutron hole to a $d_{3/2}$ proton. This gives possible 1^+, 2^+ and 3^+ states, and these states should be connected to the ground state via fairly strong $E2$ transitions because of the orbital angular momentum change of $2\,\hbar$ between the $d_{3/2}$ and $s_{1/2}$ orbits. In

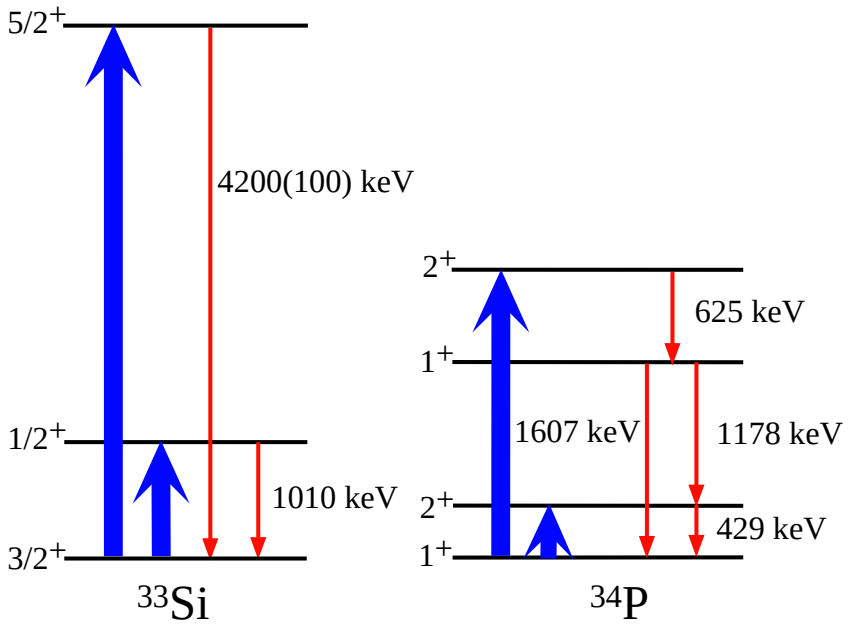

Figure 4.16: Level schemes of ^{33}Si and ^{34}P.

fact, calculations predict a 1^+ state at 1.4 MeV that connects to the ground state via a 3.3 e^2fm^4 $E2$, a 2^+ state at 2.2 MeV with $B(E2) = 5.8$ e^2fm^4, and a 3^+ state at 2.7 MeV with $B(E2) = 6.9$ e^2fm^4. Figure 4.16 demonstrates that the 1.4 MeV state probably corresponds to a previously known 1^+ state at 1607.6(2) keV. The relatively large $B(E2)$ values for the second multiplet are in agreement with an observed cross section for the 627(9) transition in ^{34}P, which is probably due to de-excitation of the second excited 2^+ state at 2232 keV to the first excited 1^+ state at 1607 keV.

Unfortunately our experimental result is in partial disagreement with the shell-model calculations [73], which predict that the branching ratio from the 2232 keV state to the 1607 keV state is only 1.9% and in 67.4% of cases this state de-excites via the 429 keV state. A similar problem exists between the calculated and experimentally known branching ratios for the decay of the 1607 keV state into the 429 keV state [62], which are 97% and 64%, respectively. An alternative explanation of the disagreement between the shell-model model calculations and the experimental observations is a negative parity state at 625 keV.

A more complete understanding of the experimental level scheme of ^{34}P is necessary to clarify this problem.

Chapter 5

Summary

Two intermediate-energy Coulomb excitation experiments with nuclear radioactive beams produced via nuclear fragmentation of ^{40}Ar and ^{48}Ca primary beams have been performed at the National Superconducting Cyclotron Laboratory. In the first experiment the neutron-rich radioactive nuclei of ^{26}Ne, ^{30}Mg, ^{28}Na, ^{33}Si and ^{34}P were produced and studied. In the second experiment, neutron-rich radioactive nuclei of ^{28}Ne, ^{29,30,31}Na, ^{31,32,33,34}Mg and ^{34,35}Al were investigated.

A primary motivation for these experiments was the study of the nuclear structure of the $N \sim 20$ neutron-rich nuclei. Only recently, modern accelerator technologies provided an opportunity to study this region. The ^{32}Mg measurements, which were conducted at CERN and RIKEN [13, 14, 15, 16], indicate that this isotope has large deformation, high collectivity and a low energy of the first excited state. Such a combination of nuclear properties is explained by the inversion of the normal shell ordering (the $\nu(f_{7/2})$-neutron orbitals lowering in energy into the $\nu(sd)$-shell). Nuclear theory [5, 18] indicates that intruder configurations are also present in ^{33}Mg, ^{31,32}Na and ^{30,31}Ne, which form the so-called island of inversion or island of deformed nuclei.

The scientific objective of this thesis was to create a more complete and comprehensive experimental picture of deformed light nuclei in this region. Properties

of the first excited states in 15 different nuclei were studied, including ^{32,33}Mg and ^{31}Na. Results for ^{32}Mg are in good agreement with the previous measurement. The observation of the 1436(1) keV transition indicates feeding, which can reduce the $B(E2)$ value for ^{32}Mg by 27%. Due to the uncertainty in spin and parity assignments in odd isotopes, the results on ^{33}Mg are not conclusive. However, the large observed excitation cross section and transition energy in ^{33}Mg are comparable to that of ^{32}Mg.

The current work is the first study of the excited states in ^{28,29,30,31}Na. Intrinsic ground state and transition electric quadrupole moments in sodium isotopes, in which possible feeding from higher-lying excited states was ignored, were compared. Agreement between absolute values of the ground and transition state moments in ^{28,29,30}Na indicates a rotational nature of deformation while a relatively large transition quadrupole moment in ^{31}Na could indicate the vibrational nature of the deformation. However, this experimental study of the nuclear properties of the first excited state in ^{31}Na is not sufficient for a definite conclusion.

The study of transition energies and excitation cross sections for the first excited states in ^{34,35}Al, ^{31}Mg and ^{30}Na experimentally proves that the island of inversion is centered at $N = 20$ and $Z \leq 12$. Other isotopes which were studied in this thesis, such as ^{30,34}Mg, ^{26,28}Ne, ^{33}Si and ^{34}P provide information about nuclear properties in the vicinity of the island, such as the energy of the 2_1^+ state and collectivity in ^{28}Ne, which suggest strong mixing between the intruder and normal configurations in this nucleus.

An ongoing upgrade of the NSCL accelerator facility combined with the development of the NSCL segmented Ge-detectors and a new NaI(Tl) array will provide additional capabilities to complete Coulomb excitation studies of the island of inversion region. At the same time strong progress in this field is expected at RIKEN, REX-ISOLDE and GANIL, which will result in a better understanding of nuclear

structure and collectivity in this interesting region.

Appendix A

Cross Section Calculations

Cross sections for electric and magnetic transitions were calculated by using the `boris_wi79.m` code, which is based on equation 2.23 and located in the `/usr/TruCluster/users/prityche/math` subdirectory. This code uses definitions and constants which are located in `/usr/TruCluster/users/prityche` directory. Consequently, constants and definitions are loaded first by using an `incl.m` file which is located in `/usr/TruCluster/users/prityche` directory.

```
<</usr/local/math/Packages/Graphics/Graphics.m
<</usr/TruCluster/users/prityche/constants.m
<</usr/TruCluster/users/prityche/gen_defs.m
<</usr/TruCluster/users/prityche/em_trans.m
<</usr/TruCluster/users/prityche/lboost.m
LoadInclude=True
```

Finally, the actual cross section calculation code (`boris_wi79.m` code) is presented below.

```
(* make sure the constants and definitions are loaded *)
<</usr/TruCluster/users/prityche/incl.m
```

```
ShowParm[t_]:=Do[
    Print[t[[i]][[2]],"   =   ",t[[i]][[1]]],{i,1,Length[t]} ]

Xibeta[]:=Block[{temp,tempA,Ecm,mu,gamma,a0} ,
    gamma=Evaluate[Sqrt[1-BetaBeam^2]^-1];
    mu = mNucl * Atarget*Aprojectile/(Atarget+Aprojectile);
 (* reduced mass in  MeV *)
    tempA = Ztarget*Zprojectile * FineAlpha * HBarC ;
(* define this since we have to use it later on *)
    Ecm = gamma mu BetaBeam^2 /2;
    a0 = tempA / (2 Ecm) ;
(* half distance of closest approach in head on
collisions (fm) *)
    BMin=N[a0 Cot[ThetaMax/2]];
(* minimum impact parameter (fm)*)
    RMin=N[tempA/(2 Ecm) + Sqrt[(tempA/(2 Ecm))^2 + BMin^2]];
(* distance of closest approach *)
    Xi=DeltaEnergy/(HBarC*gamma*BetaBeam) * BMin;
     (* adiabaticity parameter xi w/o correction term *)
    XiHigherOrder=DeltaEnergy/(HBarC*gamma*BetaBeam)*
(BMin + Pi/2 Ztarget Zprojectile FineAlpha *
(* w/ correction term *)
        HBarC / (mu gamma BetaBeam^2) );
    temp=Evaluate[a0/gamma * DeltaEnergy/
(HBarC*gamma*BetaBeam)];
```

```
    Clear[XiFuncTh];
    XiHigherOrder
    ]
GE[lam_,mu_,invbeta_]:=
Block[{GEposmu,posmu},
    posmu=Abs[mu];
        GEposmu=Evaluate[Simplify[I^(lam+posmu) *
        Sqrt[16 Pi]/(lam*(2 lam +1)!!) *
        Sqrt[(lam-posmu)!/(lam+posmu)!] *
        Sqrt[invbeta^2 - 1]^-1 *
        ((lam+1)(lam+posmu)/(2 lam + 1 ) *
(Evaluate[LegendreP[lam-1,posmu,3,xxx
        ]]/.xxx->invbeta) -
        lam * (lam-posmu+1)/(2 lam + 1 ) *
(Evaluate[LegendreP[lam+1,posmu,3,xxx
         ]])/.xxx->invbeta)]];
    If[mu>=0,GEposmu,(-1)^mu * GEposmu,
Print["siw in GE[]"] ]
    ]
GM[lam_,mu_,invbeta_]:=
Block[{GMposmu,posmu},
    posmu=Abs[mu];
        GMposmu=Evaluate[Simplify[I^(lam+posmu+1) *
        Sqrt[16 Pi]/(lam*(2 lam +1)!!) *
        Sqrt[(lam-posmu)!/(lam+posmu)!] *
        Sqrt[invbeta^2 - 1]^-1 *
```

```
        ( posmu * (Evaluate[LegendreP[lam,posmu,3,xxx
 ]]/.xxx->invbeta))]];
    If[mu>=0,GMposmu,(-1) * ((-1)^mu) * GMposmu,
Print["siw in GM[]"] ]
    ]
gAl[mu_,xi_]:=Block[{mupos},
    mupos=Abs[mu];
    Pi xi^2 ( Abs[BesselK[mupos+1,xi]]^2 -
Abs[BesselK[mupos,xi]]^2 -
        2 mupos/xi BesselK[mupos+1,xi] BesselK[mupos,xi]) ]

SigmaCE[xi_]:=N[(Ztarget*FineAlpha)^2 * (DeltaEnergy/HBarC)^
(2 (LambdaExcitation-1)) *
    If[EorM==1,BeELam,BeMLam] *
    Sum[If[EorM==1,Abs[GE[LambdaExcitation,mu,1/BetaBeam]]^2,
Abs[GM[LambdaExcitation,mu,1/BetaBeam]]^2] *
    gAl[mu,xi],{mu,-LambdaExcitation,LambdaExcitation}],7]

Clear[ThetaMax,DeltaEnergy,BetaBeam,Atarget,Ztarget,
Aprojectile,Zprojectile,LambdaExcitation,BeELam,BeMLam,EorM]

InputSigma[]:=(
    ThetaMax         =
Input["Max. sc. angle in CM in Degrees : "] Degree;
    DeltaEnergy      =
Input["Excitation energy  in MeV       : "];
```

```
    BetaBeam         =
Input["Beam velocity in c              : "];
    Atarget          =
Input["A of target                     : "];
    Ztarget          =
Input["Z of target                     : "];
    Aprojectile      =
Input["A of projectile                 : "];
    Zprojectile      =
Input["Z of projectile                 : "];
    LambdaExcitation =
Input["Multipolarity of transition     : "];
    EorM             =
Input[" Is it electric - 1 or
magnetic - 0 transition?  : "];
    If[EorM==1,Print["B(E",LambdaExcitation,") in e^2 fm^",
2 LambdaExcitation],
    Print["B(M",LambdaExcitation,") in e^2 fm^",
2*LambdaExcitation]];
    If[EorM==1,BeELam           = Input["    : "],
BeMLam          = Input["    : "]];
    If[EorM==1,BeMLam=0,BeELam=0];
(*    Print["B(E",LambdaExcitation,") in e^2 fm^",
2 LambdaExcitation];
    BeELam           = Input["    : "];
    Print["B(M",LambdaExcitation,") in muN^2 fm^",
```

```
2*LambdaExcitation-2];
    BeMLam            = Input["    : "]; *)
    )


SigmaList:={
            {ThetaMax,         "ThetaMax"},
            {DeltaEnergy,      "DeltaEnergy"},
            {BetaBeam,         "BetaBeam"},
            {Atarget,          "Atarget"},
            {Ztarget,          "Ztarget"},
            {Aprojectile,      "Aprojectile"},
            {Zprojectile,      "Zprojectile"},
            {LambdaExcitation,"LambdaExcitation"},
            {BeELam,           "BeELam"},
            {BeMLam,           "BeMLam"},
            {EorM,             "EorM"}
           }


CheckDef[t_]:= Block[{notdef},
    notdef=False;
    Do[
    If[N[t[[i]]][[1]]==0,Null,Null,Print[t[[i]][[1]],"
is not defined;"];notdef=True],
{i,1,Length[t]
```

```
    }];
    notdef]

Sigma[]:=Block[{sigma},
    If[CheckDef[SigmaList],InputSigma[]];
(* start calculation *)
    Xibeta[];
    sigma = SigmaCE[XiHigherOrder];
    sigmaNoCor = SigmaCE[Xi];
    Print[" "];
    Print[" "];
    Print["---------------------------------"];
    Print["Target     : A = ",Atarget,"  Z = ",Ztarget];
    Print["Projectile : A = ",Aprojectile,"   Z = ",Zprojectile];
    Print["---------------------------------"];
    Print["ThetaMax             = ",ThetaMax];
    Print["Beam velocity        = ",BetaBeam," c "];
    Print["BMin (impact parm.)  = ",N[BMin]," fm"];
    Print["RMin (closest appr.) = ",N[RMin]," fm"];
    Print["---------------------------------"];
    Print["Excitation Energy         = ",
DeltaEnergy," MeV  "];
    Print["Mulipolarity of Transition: ",
LambdaExcitation];
    Print["Xi   =",N[Xi],"        xi w/ higher order =",
N[XiHigherOrder]];
```

```
    If[EorM==1,
    Print["B(E",LambdaExcitation,")                    = ",
BeELam," e^2 fm^",
2 LambdaExcitation],
    Print["B(M",LambdaExcitation,")                    = ",
BeMLam," e^2 fm^",
2*LambdaExcitation]];
    Print["---------------- -----------------"];
    Print["Projectile excitation cross section:"];
    Print["Values in parenthesis are w/o the correction
term for Xi"];
    Print["sigma  = ",sigma,"(",sigmaNoCor,")"," fm^2  = ",
10 sigma," mb "];
    Print["---------------------------------"];
    sigma
    ]


Print["Use Sigma[] to calculate Coulomb Excitation
cross sections"]
Print["Use AngDis[] to calculate Angular Distributions"]
Print["Use An[] to calculate Angular Distributions;
only \n changing the variables in AngDisList"]
Print["Use ShowParm[SigmaList] and ShowParm[AngDisList]
to see \nwhich variables to change "]
```

This code allows the calculation of experimental cross sections when Z_p, Z_t, A_p, A_t, θ_{cm}^{max}, v_p, energy of the first excited state and reduced transition probability ($B(\pi, \lambda)$)

are known (see equation 2.23). In practice, the analysis of experimental data produces excitation cross section which allows the present code to calculate $B(\pi, \lambda)$.

The Winther and Alder functions ($G_{\pi\lambda\mu}\left(\frac{c}{v}\right)$, $g_\mu(\xi(b_{min}))$) can be calculated as follows:

```
troy.nscl.msu.edu> math
Mathematica 4.0 for Digital Unix
Copyright 1988-1999 Wolfram Research, Inc.
 -- Motif graphics initialized --

In[1]:= <<boris_wi79.m
 -- File graphics initialized --
loaded constants.m
Use Sigma[] to calculate Coulomb Excitation cross sections
Use AngDis[] to calculate Angular Distributions
Use An[] to calculate Angular Distributions; only
 changing the variables in AngDisList
Use ShowParm[SigmaList] and ShowParm[AngDisList] to see
which variables to change

In[2]:= N[GE[1,1,x]]

                                  1. + x
        1.67109 (-1. + x) x Sqrt[-------]
                                  -1. + x
Out[2]= ---------------------------------
                              2
```

```
                 Sqrt[-1. + x ]

In[3]:= N[GM[2,1,x]]

                                    1. + x
        0.289441 (-1. + x) x Sqrt[-------]
                                    -1. + x
Out[3]= ----------------------------------
                                2
                  Sqrt[-1. + x ]

In[4]:= N[gAl[1,x]]

                 2                          2                        2
Out[4]= 3.14159 x  (-1. Abs[BesselK[1., x]]  + Abs[BesselK[2., x]]  -

       2. BesselK[1., x] BesselK[2., x]
>      --------------------------------)
                      x

In[5]:= Quit
```

These calculated values reproduce the values tabulated in [35].

Appendix B

Calculation of Angular Distributions

The angular distribution of Coulomb de-excitation γ-rays was calculated by using a `boris_ang_dis.m` code which is based on equation 2.31 and located in `/usr/TruCluster/users/prityche/math` subdirectory. The `boris_ang_dis.m` code was written in MATHEMATICA and presented below.

```
<</usr/TruCluster/users/prityche/math/boris_wi79.m

Unprotect[F]
F[k_,Jf_,L1_,L2_,Ji_]:=(-1)^(Jf-Ji-1) * Sqrt[(2*L1 + 1)(2*L2 + 1) *
    (2*Ji+1)] * ClebschGordan[{L1,1},{L2,-1},{k,0}] *
    RacahW[{Ji,Ji,L1,L2},{k,Jf}]

Clear[Ji,Jf,Jff,DeltaMixing,ParityChange]

InputAngDis[]:=(
    If[CheckDef[SigmaList],InputSigma[]];
```

```
       Ji          = Input[" Initial angular momentum            : "];
       Jf          = Input[" Angular momentum of excited state   : "];
       Jff         = Input[" Final   angular momentum            : "];
       DeltaMixing = Input[" mix. ratio for mixed multip. de-exc. : "];
       ParityChange= Input[" Paritychange between Jf and Jff?
1/0 (= y/n)  : "];
(*EorM = Input[" Is it Electr. or Mag. transition? 1/0 (= y/n) : "];*)
    )
AngDisList:={
            {Ji,        "Ji"},
            {Jf,         "Jf"},
            {Jff,        "Jff"},
            {DeltaMixing,"DeltaMixing"},
            {ParityChange,"ParityChange"}
            }

CheckInputAngDis[]:=Block[{temp},
    If[Abs[Ji-Jf]>LambdaExcitation,Print["Abs[Ji-Jf] >
LambdaExcitation"];temp=True];
    If[Ji+Jf<LambdaExcitation,     Print["Ji+Jf < LambdaExcitation"];
temp=True];
    temp]

AngDis[]:= Block[{kMax,LamMin,LamMax},
    If[CheckDef[AngDisList],InputAngDis[]];
    If[CheckDef[SigmaList],InputAngDis[]];
```

```
    If[N[XiHigherOrder]==0,Null,Xibeta[],Xibeta[]];
    If[CheckInputAngDis[],Print["Calculation aborted"];Return[0]];
(* Ji gets excited to Jf which then decays to Jff;
   in  most cases we have Ji=Jff                    *)
(* find out what multipolarities for de-excitation are possible *)
    LamMin=Abs[Jf-Jff];
    If[(LamMin==0)&&(Jf+Jff>0),LamMin=1,Null,Print["siw"] ];
              (* there is no M0 or E0 transition *)
    If[ ((Mod[LamMin,2]==0)&&(ParityChange==0)) ||
((Mod[LamMin,2]==1)&&(ParityChange==1)),
        LamMax=LamMin,                 (* Pure ELamMin transition *)
        LamMax=Min[LamMin+1,Jf+Jff],
(* for Mlam transition consider next higher E transition if at all
possilble *)
        Print["siw AngularDistrib"]];
(*        Print["LamMax ",LamMax];
        Print["LamMin ",LamMin];  *)
(* now we can determine the coeff. in front of the P_lm *)
(* first we determine kMax *)
    kMax=Max[2Jf,2LambdaExcitation];
    Do[A[k]=Sum[
(*        Print["l1 ",l1];
        Print["l2 ",l2];
        Print["mu ",mu];  *)
            If[l1==LamMin,1,DeltaMixing,Print["siw AngularDistrib 2"]]
If[l2==LamMin,1,DeltaMixing,Print["siw AngularDistrib 3"]] *
```

```
            If[EorM==1,
            Abs[GE[LambdaExcitation,mu,1/BetaBeam]]^2,
            Abs[GM[LambdaExcitation,mu,1/BetaBeam]]^2] *
            gAl[mu,XiHigherOrder] (-1)^mu *
            ThreeJSymbol[{LambdaExcitation,mu},{LambdaExcitation,-mu},
{k,0}] *SixJSymbol[{Jf,Jf,k},{LambdaExcitation,LambdaExcitation,Ji}]
F[k,Jff,l1,l2,Jf]  Sqrt[2k+1],
            {l1,LamMin,LamMax},{l2,LamMin,LamMax},
(* sum over the possible de-excitation multipolarities *)
            {mu,-LambdaExcitation,LambdaExcitation}
(* sum over magnetic QN of excitation   *)
            ] (* close Sum *)
        ,{k,0,kMax,2}];  (* close do-loop *)
    Do[ Print["a",k,"  =  ", N[A[k]/A[0]]] ,{k,0,kMax,2}];
    Print["W = 1/(4 Pi) (a0 P0 + a2 P2 + ...)\n\n"];
    Clear[W,Wboosted];
    W[theta_]:=Evaluate[Sum[ N[A[k] /A[0] /4 /Pi,15]
LegendreP[k,Cos[theta]],{k,0,kMax,2}]];
(* angular distrib normal. to one *)
    Wcontracted[thetacm_]:=W[thetacm]*DomCmDomLab[thetacm,BetaBeam];
    Wboosted[thetalab_]:=Wcontracted[ThetaCm[thetalab,BetaBeam]];
    Print["W[theta] defined as Angular distribution in
projectile frame "];
    Print["Wboosted[theta] defined as Angular distribution
in labframe "];
    ]
```

```
An[]:=(InputAngDis[];AngDis[])
```

The boris_ang_dis.m code requires information on target and projectile parameters, which are set by the boris_wi79.m code. The boris_wi79.m code is located in the same directory and discussed in Appendix A. An example of use of the boris_ang_dis.m for Coulomb cross section calculations for $E2\uparrow$ transitions is presented below.

```
troy.nscl.msu.edu> math
Mathematica 4.0 for Digital Unix
Copyright 1988-1999 Wolfram Research, Inc.
 -- Motif graphics initialized --

In[1]:= <<boris_ang_dis.m
 -- File graphics initialized --
loaded constants.m
Use Sigma[] to calculate Coulomb Excitation cross sections
Use AngDis[] to calculate Angular Distributions
Use An[] to calculate Angular Distributions; only
 changing the variables in AngDisList
Use ShowParm[SigmaList] and ShowParm[AngDisList] to see
which variables to change

In[2]:= Sigma[]
ThetaMax is not defined;
DeltaEnergy is not defined;
BetaBeam is not defined;
Atarget is not defined;
```

```
Ztarget is not defined;
Aprojectile is not defined;
Zprojectile is not defined;
LambdaExcitation is not defined;
BeELam is not defined;
BeMLam is not defined;
EorM is not defined;
Max. sc. angle in CM in Degrees : 3.24
Excitation energy  in MeV       : 0.35
Beam velocity in c              : 0.3195
A of target                     : 197
Z of target                     : 79
A of projectile                 : 31
Z of projectile                 : 11
Multipolarity of transition     : 2
 Is it electric - 1 or magnetic - 0 transition?  : 1
B(E2) in e^2 fm^4
    : 100



-------------------------------------------------
Target     : A = 197  Z = 79
Projectile : A = 31   Z = 11
-------------------------------------------------
ThetaMax             = 0.0565487
Beam velocity        = 0.3195 c
```

```
BMin (impact parm.)  = 16.4614 fm
RMin (closest appr.) = 16.9336 fm
-------------------------------------------------
Excitation Energy         = 0.35 MeV
Mulipolarity of Transition: 2
Xi   =0.0865958        xi w/ higher order =0.0904428
B(E2)                     = 100 e^2 fm^4
-------------------------------------------------
Projectile excitation cross section:
Values in parenthesis are w/o the correction term for Xi
sigma  = 2.35695(2.56844) fm^2  = 23.5695 mb
-------------------------------------------------

Out[2]= 2.35695

In[3]:= Quit
```

Finally, it is worth to mention that this code is good for both $E\lambda\uparrow$ and $M\lambda\uparrow$ transitions.

Appendix C

Detector Calibrations

The present appendix contains a description of the standard calibration procedure of the NSCL NaI(Tl)-array, which includes position, energy and efficiency calibrations and the generation of calibrated position, energy and efficiency data files for the nuclear data analysis.

C.1 Position Calibrations

Usually position calibrations of the NSCL NaI(Tl) array are conducted before and after each experimental run by using the special collimator described in subsection 3.3.1. A ^{60}Co radioactive source inserted between two discs made of HeviMet can be installed and moved inside the beam pipe with a calibrated stick (measuring tape is attached to it). This allows to calibrate all detectors at the same time by moving the source in 1.27(0.635) cm-long steps. The duration of a typical calibration run is 5 minutes.

The physical principles of position calibrations are described in subsection 3.3.2. Here I will present a practical recipe for development of a calibrated position data file:

• Convert position on the stick into metric system (cm) and add the distance from the end of stick to the actual position of ^{60}Co radioactive source in the HeviMet assembly (7.62 cm + 0.23 cm = 7.85 cm).

• Create Smaug spectra by using the `position.def` file from `nscl_nuclear:[96037.boris.position]` subdirectory. For each run (certain position on the stick) one has to dump raw position files.

• Convert Smaug files into GeLi fit standard and fit it using modified command file `gf1.cmd`. Rename `gf2.out` files into `pos_*.out`. `Pos_*.out` files contain information about position fit for each detector.

• Create `detNN_fit.dat` files by cutting and pasting from `pos_*.out` files. These files should have two columns. The first is position in cm the second one is channel number (see for example `det01_fit_example.dat`).

• Start Physica by typing `setup physica` and after that `physica`. Start the fitting routine by typing `@fitall`. It will produce files called `detNN.out` and will print position curves.

• Update a `maketable2.for` code (east and west edges of the array) and run it. It will produce file `poscal_cubic2.dat` which can be used in the broutines.

C.2 Energy Calibrations

Subsection 3.3.3 contains the description of energy calibrations which include 2-hours long data collection runs with a radioactive sources (^{152}Eu, ^{228}Th, ^{88}Y and ^{22}Na) placed in the center of the array and development a calibrated-energy data file.

The calibrated-energy data file is generated as follows:

• Create Smaug files with cuts over non-calibrated position for each detector using `gates.for` file from the `nscl_nuclear:[96037.boris.energy]` subdirectory.

• Convert Smaug files into GeLi fit standard and fit them, using command file

`gf2.cmd (gf2.for)`. Rename `gf2.out` files into `22na.out, 228th.out, 152eu.out` and `88y.out`.

• Run `encal.for`, which will create `geliecal_XXX.list`, where `XXX` stands for the slice number.

• Run Physica by typing:`@richfit geliecal_XXX 'Energy'`. File `richfit.pcm` can be edited for linear or quadratic fit.

• Create `l98XXX.dat` file and update `phyres11.for` file. Run `physres11.for`, which will take the fit results from `geliecal_XXX.out` and place them into `l98XXX.dat`.

• Basically `l98XXX.dat` can be used for the energy calibration in the broutines. At the same time one can create `en_array.tab` files.

• Create `en_array.tab` by running `trans.for`, which will produce `en_array.tab-new`. Rename `en_array.tab-new` into `en_array.tab` and use it for energy calibration in the broutines. Currently, `trans.for` is set for 10 slices.

C.3 Efficiency Calibrations for Isotropic Source

Efficiency calibrations (measurements) for isotropic sources are described in subsection 3.4.1. The efficiency calibration procedure is conducted with the calibrated γ radioactive sources (^{22}Na, ^{88}Y, ^{152}Eu and ^{228}Th) located in the exact target position. Nuclear data is collected for each 2-8 hours long calibration runs and analyzed. The extracted efficiency of the array is presented in Figure 3.14. The experimentally measured detection efficiency is more preferable than calculated because of the complex design of the experimental apparatus. The calibration γ-sources are presented in Table C.1. To achieve consistency between different radioactive sources activity of ^{152}Eu was reduced by 21%.

The development of the calibrated efficiency data file consists of the following steps:

Table C.1: Description of the calibration γ-sources ($\star$ - denotes uncertainties at the 99% confidence level, † - denotes uncertainties with an unknown confidence level and ‡ - denotes a corrected source strength).

Parent nucleus	NSCL source number	Source strength/Date
^{22}Na	NSCL-132	$10.46 \pm 0.37 \mu$Ci* (11/1/1988)
^{88}Y	NSCL-507	$11.5 \pm 1.5 \mu$Ci† (12/15/1996)
^{152}Eu	NSCL-139	$14.64 \pm 0.542 \mu$Ci‡ (11/1/1988)
^{228}Th	F9074	$11.47 \pm 0.37 \mu$Ci* (10/1/1994)
^{228}Th	NSCL-503	$1.286 \pm 0.032 \mu$Ci* (6/1/1995)

• The preliminary requirements include good energy and position calibrations, and good knowledge of the radioactive sources activities, branching ratios, live time and total time of the measurements.

• Cut each detector into 10 slices over calibrated position, and plot calibrated energy with no multiplicity for each slices (^{152}Eu,^{228}Th,^{88}Y and ^{22}Na). It is good to use 10 keV/ch binnings. This can be done in Smaug using the modified `gatec.for` file from the `nscl_nuclear:[96037.boris.efficiency]` subdirectory.

• Convert Smaug output files into GeLi fit standard.

• Fit photopeaks for all sources by using the `gf2.cmd` command file. After that rename `gf2.out` files into `eff22na.out, eff88y.out, ...` .

• Run `effcal152eu1.for`, which create `eff152eu1.list`. Run `effcalth1.for , ...` .

• Run `eff97013-152eu1.for, eff97013-152eu2.for, ...` which will create files `*.table`. The typical order is ^{152}Eu, ^{228}Th, ^{88}Y and ^{22}Na.

• Look into `*.tables` files and identify the files which are empty or different from

the rest.

• Update `overallq_10pos_det.pcm, overallq_9pos_det.pcm and eff_fit_thr.pcm` for the detectors which are different from the rest.

• Start Physica and type `syst=0.05` (5% systematic error originates from an imperfect personal judgment of the fit boundaries). In physica type `@overall` and after that `det01, ...` this will create file `effdet01.out, ...` .

• Using file `effdet01...` one has to edit `9XXXX_eff.m` and `general9XXXX_eff.m`.

An example of an efficiency calculations for $E2$ transitions (^{31}Na) and 11 detectors (inner ring) is presented below.

```
troy.nscl.msu.edu> math
Mathematica 4.0 for Digital Unix
Copyright 1988-1999 Wolfram Research, Inc.
 -- Motif graphics initialized --

In[1]:= <<general9701311_eff.m
 -- File graphics initialized --
loaded constants.m
Use Sigma[] to calculate Coulomb Excitation cross sections
Use AngDis[] to calculate Angular Distributions
Use An[] to calculate Angular Distributions; only
 changing the variables in AngDisList
Use ShowParm[SigmaList] and ShowParm[AngDisList] to see
which variables to change
Use Effic[] to calculate efficiencies
Function Effw[beta,energy,i1,i2,HalfThick] defined
```

```
In[2]:= detlist={1,2,3,4,5,6,7,8,9,10,11}


Out[2]= {1, 2, 3, 4, 5, 6, 7, 8, 9, 10, 11}


In[3]:= Effic[]
File to load efficiency array from? 9701311_n101_eff.m
Please enter Half-Thickness for Au at this energy (mg/cm^2) : 2552
Please enter actual total thickness of Au target (mg/cm^2) : 702
Ji is not defined;
Jf is not defined;
Jff is not defined;
DeltaMixing is not defined;
ParityChange is not defined;
ThetaMax is not defined;
DeltaEnergy is not defined;
BetaBeam is not defined;
Atarget is not defined;
Ztarget is not defined;
Aprojectile is not defined;
Zprojectile is not defined;
LambdaExcitation is not defined;
BeELam is not defined;
BeMLam is not defined;
EorM is not defined;
Max. sc. angle in CM in Degrees : 3.24
Excitation energy  in MeV       : 0.35
```

```
Beam velocity in c              : 0.3195
A of target                     : 197
Z of target                     : 79
A of projectile                 : 31
Z of projectile                 : 11
Multipolarity of transition     : 2
 Is it electric - 1 or magnetic - 0 transition?  : 1
B(E2) in e^2 fm^4
    : 310
 Initial angular momentum            : 1.5
 Angular momentum of excited state   : 2.5
 Final   angular momentum            : 1.5
 mixing ratio for mixed multip. deexcitation : 0
 Paritychange between Jf and Jff? 1/0 (= y/n)  : 0

ClebschGordan::tri: ThreeJSymbol[{1., 1}, {2., -1}, {0, 0}]
is not triangular.

ClebschGordan::tri:
   SixJSymbol[{2.5, 2.5, 0}, {2., 1., 1.5}] is not triangular.

ClebschGordan::tri: ThreeJSymbol[{1., 1}, {2., -1}, {0, 0}]
is not triangular.

General::stop: Further output of ClebschGordan::tri
     will be suppressed during this calculation.
```

-32

a0 = 1. - 4.93038 10 I

a2 = 0.134231 + 0. I

a4 = 0. + 0. I

W = 1/(4 Pi) (a0 P0 + a2 P2 + ...)

W[theta] defined as Angular distribution in projectile frame

Wboosted[theta] defined as Angular distribution in labframe

The total raw efficiency of the array is 20.0934 %

For projectile peak, efficiency is 17.5029% +/- 0.0844131%

The total raw efficiency of the array is 20.0934 %

Including absorption: 10.8893% +/- 0.0552119%

a0 = 1.

a2 = -0.385396

a4 = -0.0240751

a6 = 0.

W = 1/(4 Pi) (a0 P0 + a2 P2 + ...)

W[theta] defined as Angular distribution in projectile frame

Wboosted[theta] defined as Angular distribution in labframe

The total raw efficiency of the array is 15.0157 %

For target (gold) peak, efficiency is 14.0039% +/- 0.0670267%

The total raw efficiency of the array is 15.0157 %

Without absorption, @ 547.5 keV: 16.8188%

```
In[4]:= Quit
```

Such calculations can be performed for all $E\lambda$ and $B\lambda$ transitions.

Appendix D

ECIS Calculations

A phenomenological Saxon-Woods nuclear potential (optical potential) is usually defined as follows [87]

$$V_n(r) = (V + iW)f(r)\,, \tag{D.1}$$

where $V(r)$ and $W(r)$ are real and imaginary parts, $f(r) = (1 + exp((r - R_0)/a)^{-1}$ with $R_0 = r_0(A_p^{1/3} + A_t^{1/3})$, r_0 and a are the potential reduced radius and diffuseness, respectively. The Coulomb potential $V_c(r)$ (potential between a point charge and a uniform charge distribution with a radius $R_c = r_c\left(A_p^{1/3} + A_t^{1/3}\right)$, where r_c is the reduced charge distribution radius) is defined as follows [87]

$$V_c(r) = \begin{cases} Z_p Z_t e^2/r & \text{for} \quad r \geq R_c \\ Z_p Z_t e^2/2R_c\,[3 - (r/R_c)^2] & \text{for} \quad r < R_c \end{cases}\,. \tag{D.2}$$

In the current calculation the following optical potential parameters were used [83]: V=50 MeV, W=57.9 MeV, r_V=r_W=1.067 fm, a_V=a_W=0.800 fm and r_c=1.2 fm.

The input data file for the coupled-channels code ECIS88 [82] with an optical model parameters set determined for the ^{17}O+^{208}Pb reaction at 84 MeV/nucleon [83] is presented below. This particular file was created by L.A. Riley and used for the calculation of nuclear contribution of the ^{31}Na+^{197}Au reaction at 51.5 MeV/nucleon [75].

```
197Au on 31Na   Elab = 51.5 MeV/A   5/2 State   Coulomb + Nuclear Rot.
tFFFTFFtFFTTFFFTFFFFTFFFFFFFTFFFFFFFFFFFFFFTFFFFFF
FFFFFFFFFFFFFFFFTTTFfFFFFFFFFFFFFFFFFFFFFFFFFFFF
    25000                                        500

1.5  00   10145.5000   0.00000  197.0000   31.0000  869.
2.5  00       0.350
    2    2    1.5
 0.5900
 0.5900     0.0      0.0       0.0       0.0       0.5900    0.0
50.0       1.067    0.800
57.9       1.067    0.800




1.200

   0.01000   0.01000    3.2400
FIN
//

*********************************************************************

197Au on 31Na   Elab = 51.5 MeV/A   5/2 State    Coulomb (only) Rot.
```

```
tFFFTFFtFFTTFFFTFFFFTFFFFFFFTFFFFFFFFFFFFFFTFFFFFF
FFFFFFFFFFFFFFFFTTTfFFFFFFFFFFFFFFFFFFFFFFFFFFFFF
    25000                                        500

1.5  00   10145.5000   0.00000  197.0000   31.0000  869.
2.5  00       0.350
    2    2    1.5
 0.000
 0.000     0.0      0.0       0.0       0.0       0.5900    0.0
50.0       1.067    0.800
57.9       1.067    0.800




1.200

   0.01000   0.01000    3.2400
FIN
//

*********************************************************************

197Au on 31Na   Elab = 51.5 MeV/A   5/2 State   Nuclear (only) Rot.
tFFFTFFtFFTTFFFTFFFFTFFFFFFFTFFFFFFFFFFFFFFfFFFFFF
```

```
FFFFFFFFFFFFFFFFTTTFfFFFFFFFFFFFFFFFFFFFFFFFFFFFF
    25000                                          500


1.5  00    10145.5000    0.00000  197.0000   31.0000  869.
2.5  00         0.350
    2    2     1.5
 0.5900
 0.5900      0.0       0.0        0.0        0.0        0.0000     0.0
50.0         1.067     0.800
57.9         1.067     0.800




1.200


   0.01000   0.01000    3.2400
FIN
//
```

LIST OF REFERENCES

[1] V.A. Matveev, F.T.Avignone, *Physics Today*, May 1994, 86.

[2] P. Möller, J.R. Nix and K.L. Kratz, *At. Data Nucl. Data Tables* **66**, 131 (1997).

[3] I. Tanihata, H. Hamagaki, O. Hashimoto, Y. Shida, N. Yoshikawa, K. Sugimoto, O. Yamakawa, T. Kobayashi and N. Takahashi, *Phys. Rev. Lett.* **55**, 2676 (1985).

[4] P.G. Hansen, A.S. Jensen, and B. Jonson, *Ann. Rev. Nucl. Part. Sci.* **45**, 591 (1995).

[5] E.K. Warburton, J.A. Becker, B.A. Brown, *Phys. Rev.* **C41**, 1147 (1990).

[6] F. Boehm, P. Vogel, *Physics of Massive Neutrinos*, (Cambridge Univ. Press, 1992).

[7] C.E. Rolf, W.S. Rodney, *Cauldrons in the Cosmos*, (Univ. of Chicago Press, 1988).

[8] W.H. Scharf, *Biomedical Particle Accelerators*, (AIP Press, 1994).

[9] T. Nakamura, N. Fukuda, T. Kobayashi, N. Aoi, H. Iwasaki, T. Kubo, A. Mengoni, M. Notani, H. Otsu, H. Sakurai, S. Shimoura, T. Teranishi, Y.X. Watanabe, K. Yoneda, and M. Ishihara *Phys. Rev. Lett.* **83**, 1112 (1999).

[10] C. Thibault, R. Klapisch, C. Rigaud, A.M. Poskanzer, R. Prieels, L. Lessard, and W. Reisdorf, *Phys. Rev.* **C12**, 644 (1975).

[11] X. Campi, H. Flocard, A.K. Kerman, and S. Koonin, *Nucl. Phys.* **A251**, 193 (1975).

[12] A. Poves, J. Retamosa, *Nucl. Phys.* **A571**, 221 (1994).

[13] C. Detraz, D. Guillemand, G. Huber, R. Klaisch, M. Langevin, F. Naulin, C. Thibault, L.C. Carraz, and F. Touchard, *Phys. Rev.* C **19**, 164 (1979).

[14] D. Guillemaund-Mueller, C. Detraz, M. Langevin, F. Naulin, M. De Saint-Simon, C. Thibault, F. Touchard and M. Epherre, *Nucl. Phys.* **A426**, 37 (1984).

[15] G. Klotz, P. Baumann, M. Bounajma, A. Huck, A. Knipper, G. Walter, G. Marguier, C. Richard-Serre, A. Poves and J. Retamosa, *Phys. Rev.* **C47**, 2502 (1993).

[16] T. Motobayashi, Y. Ikeda, Y. Ando, K. Ieki, M. Inoue, N. Iwasa, T. Kikuchi, M. Kurokawa, S. Moriya, S. Ogawa, H. Murakami, S. Shimoura, Y. Yanagisawa, T. Nakamura, Y. Watanabe, M. Ishihara, T. Teranishi, H. Okuno, R.F. Casten, *Phys. Lett.* B **346**, 9 (1995).

[17] B.V. Pritychenko, T. Glasmacher, P.D. Cottle, M. Fauerbach, R.W. Ibbotson, K.W. Kemper, V. Maddalena, A. Navin, R. Ronningen, A. Sakharuk, H. Scheit, V.G. Zelevinsky, *Phys. Lett.* B **461**, 322 (1999).

[18] E. Caurier, F. Nowacki, A. Poves, and J. Retamosa, *Phys. Rev.* **C58**, 2033 (1998).

[19] H. Sakurai, S.M. Lukyanov, M. Notani, N. Aoi, D. Beaumel, N. Fukuda, M. Hirai, E. Ideguchi, N. Imai, M. Ishihara, H. Iwasaki, T. Kubo, K. Kusaka, H.

Kumagai, T. Nakamura, H. Ogawa, Yu.E. Penionzhkevich, T. Teranishi, Y.X. Watanabe, K. Yoneda, A. Yoshida, *Phys. Lett.* **B 448**, 180 (1999).

[20] K. Alder, A. Bohr, T. Huus, B. Mottelson, A. Winther, *Rev. Mod. Phys.* **28**, 432 (1956).

[21] T. Glasmacher, *Ann. Rev. Nucl. Part. Sci.* **48**, 1 (1998).

[22] M. Goeppert Mayer, *Phys. Rev.* **75**, 1969 (1949).

[23] D.R. Hartree, *Proc. Cambridge Phil. Soc.* **24**, 89 (1928).

[24] V. Fock, *Z. Physik* **61**, 126 (1930).

[25] V. Fock, *Z. Physik* **62**, 795 (1930).

[26] J.M. Eisenberg, W. Greiner, *Nuclear Theory, Vol. 3*, (Elsevier Science Publishing Company, Inc., 1986).

[27] K.L.G. Heyde, *The Nuclear Shell Model* (Springer-Verlag, 1994).

[28] S.G. Nilsson, *Mat. Fys. Medd. Dan. Vid. Selsk.* **29**, II:212 (1955).

[29] S.G. Nilsson, I. Ragnarsson, *Shapes and shells in nuclear structure*, (Cambridge University Press, Cambridge, 1995).

[30] A. Bohr, B.R. Mottelson, *Nuclear Structure, Vol. 2*, (World Scientific, 1998).

[31] S.S.M. Wong, *Introductory Nuclear Physics* (Prentice Hall, 1990).

[32] P. Ring, P. Schuck, *The Nuclear Many-Body Problem*, (Springer-Verlag, 1980).

[33] *Table of Isotopes, edited by R.B. Firestone & V.S. Shirley* (John Wiley and Sons, Inc. Vol.I, 1996).

[34] K. Alder and A. Winther, *Electromagnetic Excitation*, (North Holland, Amsterdam, 1975); *Coulomb Excitation*, (Academic Press, New York, 1966).

[35] A. Winther and K. Alder, *Nucl. Phys.* **A319**, 518 (1979).

[36] A.N.F. Aleixo and C.A. Bertulani, *Nucl. Phys.* **A505**, 448 (1989).

[37] C.J. Benesh, B.C. Cook, and J.P. Vary, *Phys. Rev.* **C40**, 1198 (1989).

[38] S. Raman, C.W. Nestor Jr., S. Kahane, and K.H. Bhatt, *Phys. Rev.* **C43**, 556 (1991).

[39] H. Scheit, *Low-Lying Collective Excitations in Neutron-Rich Even-Even Sulfur and Argon Isotopes Studied via Intermediate-Energy Coulomb Excitation and Proton Scattering*, (Ph. D. Thesis, Michigan State University, 1998).

[40] L.D. Landau and E.M. Lifshitz, *Mechanics* (Pergamon Press, 1976).

[41] L.D. Landau and E.M. Lifshitz, *The Classical Theory of Fields* (Pergamon Press, 1979).

[42] C.A. Bertulani and G. Baur, *Phys. Rep.* **163**, 299 (1988).

[43] S. Wolfram, *The Mathematica Book*, (Cambridge University Press, 1996).

[44] C.K. Gelbke, *Nucl. Phys. News Inter.* **4**, 5 (1994).

[45] H. Scheit, T. Glasmacher, R.W. Ibbotson, P.G. Thirolf, *Nucl. Instrum. Methods* **A422**, 124 (1999).

[46] *NSCL Mechanical Design Department*, (unpublished, 1999).

[47] B. M. Sherrill, D.J. Morrissey, J.A. Nolen Jr., and J.A. Winger, *Nucl. Instrum. Methods* **B56**, 1106 (1991).

[48] H. Geissel, G. Münzenberg, and K. Riisager, Annu. Rev. Nucl. Part. Sci. **45**, 163 (1995).

[49] B. Jonson, H.L. Ravn, G. Walter, *Nucl. Phys. News Inter.* **3**, No.2 (1993).

[50] T. Nilsson,*CERN Courier* **39**, 20 (1999).

[51] R. Serber, *Phys. Rev.* **72**, 1008 (1947).

[52] M. Steiner, *Private communication.*

[53] W.R. Leo, *Techniques for Nuclear and Particle Physics Experiments* (Springer-Verlag, 1994).

[54] D. Swan, J. Yurkon, D.J. Morrissey, *Nucl. Instrum. Methods* **A 348**, 314 (1994).

[55] G.F. Knoll, *Radiation Detection and Measurement* (John Wiley & Sons, 1989).

[56] B. Pritychenko, T. Glasmacher, R.W. Ibbotson and H. Scheit, *NSCL Annual Report* 1997, Available http://www.nscl.msu.edu/research/1997_Annual_Report/home.html, December 15, 1999.

[57] *Smaug: On-line/Offline Data Analysis Program* (NSCL, unpublished, 1995).

[58] *GF2: Notes on the use of the program GF2* (Chalk River Nuclear Laboratories, unpublished, 1989).

[59] *Physica: Reference Manual* (TRIUMF, unpublished, 1994).

[60] P.R. Bevington, D.K. Robinson, *Data Reduction and Error Analysis for the Physical Sciences* (WCB/McGraw-Hill, 1992).

[61] A. H. Wapstra, G. J. Nijgh and R. van Lieshout, *Nuclear Spectroscopy Tables* (North-Holland Publ. Co., 1959).

[62] *Table of Isotopes, edited by R.B. Firestone & V.S. Shirley* (John Wiley and Sons, Inc. Vol.II, G-1, 1996).

[63] E. Storm and H.I. Israel, *Nucl. Data Tables* **A7**, 565 (1970).

[64] P.M. Endt, *Nucl. Phys.* **A521**, 1 (1990).

[65] J.M. Finn, Hall Crannell, P.L. Hallowell, J.T. O'Brien and S. Penner, *Nucl. Phys.* **A290**, 99 (1977).

[66] C. Zhou, *Nucl. Data Sheets* **76**, 399 (1995).

[67] M.J. Lopez-Jimenez, M. Belleguic, M. Stanoiu, M.- G. Saint-Laurent, L. Achouri, F. Azaiez, C. Bourgeois, C. Borcea, J.M. Daugas, G. De France, F. De Oliveira, Z. Dlouhy, C. Donzaud, J. Duprant, P. Gangnant, S. Grevy, S. Leenhardt, M. Lewitowicz, J.F. Libin, M. Marques, Y. Penionzhkevitch, L. Petizon, M.-G. Porquet, J.E. Sauvestre, H. Savajols, N. Skobelev, O. Sorlin, *contribution to XXXVII International Winter meeting on Nuclear Physics (Bormio, Italy, January 1999.*

[68] A.T. Reed, O. Tarasov, R.D. Page, D. Guillemaud-Mueller, Yu.E. Penionzhkevich, R.G. Allat, J.C. Angelique, R. Anne, C. Borcea, V. Burjan, W.N. Catford, Z. Dlouhy, C. Donzaud, S. Grevy, M. Lewitowicz, S.M. Lukyanov, F.M. Marques, G. Martinez, A.C. Mueller, P.J. Nollan, J. Novak, N.A. Orr, F. Pougheon, P.H. Regan, M.G. Saint-Laurent, T. Siiskonen, E. Sokol, O. Sorlin, J. Suhonen, W. Trinder, and S.M. Vincent, *Phys. Rev.* C **60**, 024311 (1999).

[69] C.A. Bertulani, *Computer Phys. Comm.* **116**, 1459 (1999).

[70] P.M. Endt, *At. Data Nucl. Data Tables* **23**, 3 (1979).

[71] M.J. Martin, *Nucl. Data Sheets* **74**, ix (1995).

[72] B.V. Pritychenko, T. Glasmacher, P.D. Cottle, R.W. Ibbotson, K.W. Kemper, A. Sakharuk, H. Scheit and V.G. Zelevinsky, *Proc. ENPE 99: Experimental Nuclear Physics in Europe (Seville, Spain), June 21-26, 1999*, AIP Conference Proceedings 495 (1999) 51.

[73] B.A. Brown, Available under *"Nuclear Structure Resources"* http://www.nscl.msu.edu/∼brown, December 15, 1999.

[74] G. Huber, F. Touchard, S. Büttgenbach, C. Thibault, R. Klapisch, H.T. Duong, S. Liberman, J. Pinard, J.L. Vialle, P. Juncar and P. Jacquinot, *Phys. Rev.* **18**, 2342 (1978).

[75] B.V. Pritychenko, T. Glasmacher, B.A. Brown, P.D. Cottle, R.W. Ibbotson, K.W. Kemper, L.A. Riley, H. Scheit, *submitted to Phys. Rev. Lett.*

[76] R. W. Ibbotson, T. Glasmacher, B.A. Brown, L. Chen, M.J. Chromik, P.D. Cottle, M. Fauerbach, K.W. Kemper, D.J. Morrissey, H. Scheit and, M. Thoennessen, *Phys. Rev. Lett.* **80**, 2081 (1998).

[77] T. Motobayashi, *Proc. Third IN2P3-RIKEN Symposium on Heavy Ion Collisions, Shinrin-Koen, Saitama, Japan, 24-28 October 1994.*

[78] J. Kantele, *Nucl. Instrum. Methods* **A275**, 149 (1989).

[79] B.A. Brown, A. Etchegoyen, and W.D.M. Rae, *OXBASH, The Oxford-Buenos Aires-MSU shell model code, NSCL Report No. 524, 1988.*

[80] H. Scheit, T. Glasmacher, B.A. Brown, J.A. Brown, P.D. Cottle, P.G. Hansen, R. Harkewicz, M. Hellström, R.W. Ibbotson, J.K. Jewell, K.W. Kemper, D.J. Morrissey, M. Steiner, P. Thirolf, and M. Thoennessen, *Phys. Rev. Lett.* **77**, 3967 (1996).

[81] T. Glasmacher, B.A. Brown, M.J. Chromik, P.D. Cottle, M. Fauerbach, R.W. Ibbotson, K.W. Kemper, D.J. Morrissey, H. Scheit, D.W. Sklenicka, M. Steiner, *Phys. Lett.* B **395**, 163 (1997).

[82] J. Raynal, *Coupled channel code ECIS88, unpublished.*

[83] J. Barrette, N. Alamanos, F. Auger, B. Fernandez, A. Gillibert, D.J. Horen, J.R. Beene, F.E. Bertrand, R.L. Auble, B.L. Burks, J. Gomez Del Campo, M.L. Halbert, R.O. Sayer, W. Mittig, Y. Schutz, B. Haas, J.P. Vivien, *Phys. Lett.* B **209**, 182 (1988).

[84] R.W. Ibbotson, *Octupole and Quadrupole Correlations in* ^{148}*Nd and* ^{150}*Sm Studied by Coulomb Excitation*, (Ph. D. Thesis, The University of Rochester, 1995).

[85] M. Keim, *Proc. ENAM 98: Exotic Nuclei and Atomic Masses (Bellaire, Michigan) June 23-27, 1998*, AIP Conference Proceedings 455 (1998) 50.

[86] R.W. Ibbotson, T. Glasmacher, P.F. Mantica, H. Scheit, *Phys. Rev.* C **59**, 642 (1999).

[87] R. Liguori Neto, P. Roussel-Chomaz, L. Rochais, N. Alamanos, F. Auger, B. Fernandez, J. Gastebois, A. Gillibert, R. Lacey, A. Miczaika, D. Pierroutsakou, J. Barrete, S.K. Mark, R. Turcotte, Y. Blumenfeld, N. Frascaria, J.P. Garron, J.C. Roynette, J.A. Scarpaci, T. Suomijärvi, A. Van der Woude, A.M. Van den Berg, *Nucl. Phys.* **A560**, 733 (1993).